SINGLE MOLECULE PIEZOELECTRICS AND FERROELECTRICS: FROM THEORY TO EXPERIMENT

By

Xinfeng Quan

B.S., Fudan University, 2008

Submitted to the Graduate Faculty of the

Kenneth P. Dietrich School of Arts and Sciences in partial fulfillment

of the requirements for the degree of

Doctor of Philosophy

University of Pittsburgh

2013

UNIVERSITY OF PITTSBURGH

KENNETH P. DIETRICH SCHOOL OF ARTS AND SCIENCES

This thesis was presented

by

Xinfeng Quan

It was defended on

September 13th, 2013

and approved by

Tara Y. Meyer, PhD, Associate Professor, Department of Chemistry

David H. Waldeck, PhD, Professor, Department of Chemistry

Qing-Ming Wang, PhD, Professor, Department of Mechanical Engineering

Dissertation Advisor: Geoffrey R. Hutchison, Assistant Professor, Department of Chemistry

Dissertation Advisor: Geoffrey R. Hutchison

SINGLE MOLECULE PIEZOELECTRICS AND FERROELECTRICS: FROM THEORY TO EXPERIMENT

Xinfeng Quan, PhD

University of Pittsburgh, 2013

This dissertation proposes and studies the idea of single molecule piezoelectrics and ferroelectrics via both computational and experimental means. The research is aimed to open a new area of piezoelectric/ferroelectric materials for next generation of nanoscale, flexible, efficient, and multifunctional electronic devices.

Density functional theory (DFT) calculations are employed to study the electric field induced conformational change (piezoelectric effect) of three molecular springs: asymmetrically substituted helicenes, asymmetrically substituted phenanthrenes, and oligoaminoacids and the electric field driven polarization inversion (ferroelectric effect) of molecular bowls (buckybowls). Molecular structure, functional groups, dipole moment, and regiochemistry are discussed as factors to generate good single molecule piezoelectrics and ferroelectrics. A significantly large piezoelectric coefficient (up to 272 pm/V for a hypothetical helicene derivative and 450 pm/V for a hypothetical buckybowl derivative) and a broad range of inversion field (0.26 V/nm - 9.05 V/nm for buckybowls) are predicted. Our proposed materials could potentially compete with conventional piezo/ferroelectric materials (e.g. zinc oxide (ZnO), polyvinylidene difluoride (PVDF), and lead zirconium titanate (PZT), etc.).

The piezoelectric effect of single molecules are experimentally demonstrated with a sample of patterned self-assembled monolayers (SAMs) of oligoaminoacids via techniques of piezoresponse force microscopy (PFM) and Fourier-transform infrared spectroscopy (FTIR). Combined with our computational predictions, we believe that a new class of piezoelectric/ferroelectric materials may be created from the "bottom up" based on molecular conformational changes, which are new material resources for fabricating flexible, large scale, ultrathin, and lightweight electronic devices.

TABLE OF CONTENTS

LIST OF TABLES

LIST OF FIGURES

LIST OF SCHEMES

Appendix

ACKNOWLEDGEMENTS

Reaching to the completion of my PhD degree, I would like to acknowledge many people who have helped me during this journey. I could not have achieved it without their love, coaching, inspiration, and friendship.

First I would like to acknowledge my advisor Professor Geoffrey Hutchison. Geoff has been a great mentor, gracious, knowledgeable, and illuminative. Besides our regular meetings, Geoff is always willing and patient to offer helpful discussions whenever I come to him. Without his guidance, I could not have completed both theory and experiment work of my thesis. From him I have gained a broad range of knowledge in general science as well. Being creative is very important to scientists. Geoff has always been encouraging to new ideas and been supportive to let me carry them out. I couldn't forget those mid-night text messages and emails between us when I got exciting results. I would also like to thank Geoff for helping me to improve my writing and presenting skills. I am considering him as a great model for my science career.

Deep appreciation is due to my thesis committee professors, Professor Tara Meyer, Professor David H. Waldeck, and Professor Qing-Ming Wang. Their questions, comments, and suggestions at every stage of my PhD study are very helpful in directing my research to what I have achieved today. I have also gained much confidence from their interest and appreciation to my research, as well as their encouragement for me to pursue a science career.

My gratefulness also goes to every past and present member in the Hutchison group. Marcus, Xialing, Tamika, Andrey, Adam, Paula, Steve, Chris, Ilana, Terry, Arthur, Leah, Shannon, Leandro, and Eric, you have been helpful in offering scientific discussions, and you are great friends in life as well. I have my special thanks to Paula. She has greatly helped to proofread this thesis. She is also a great teacher in my every day English, leading me into knowing the culture which science alone does not offer.

I would like to acknowledge my family. Neither of my parents ever had a chance to finish middle school education. They have devoted their lives to create a better future for me. They are so loving and so supportive. They wish I could get what they have lost, yet still be free to pursue whatever good for me. I would like to shine their names here, Jiefang and Xiaohui, even it is unconventional in our culture. My sister Zhe has also been a great sister, friend, and mentor ever since I was young. I am grateful to her love, understanding, and all kinds of support on every stage I go to. It is their love and support filling my heart for me to study abroad and to achieve success.

Last but not least, I would like to thank my girlfriend Lihua. She is also a best friend. She is understanding, sharing all my trivial or big thoughts. She is intelligent, offering critical thoughts in both scientific and daily topics. She is caring, making life sweet and full of happiness.

1.0 INTRODUCTION

The first chapter introduces fundamental knowledge of piezoelectrics and ferroelectrics, and outlines the structure of this thesis.

1.1 GENERAL BACKGROUND

1.1.1 Basics of conventional piezoelectrics

Piezoelectrics are polar materials which produce electrical charges in response to a mechanical distortion, or change shape in response to an applied electric field. As such they have achieved wide use for applications ranging from sensors,[1, 2] ultrasonic motors,[3] scanning-probe microscopy manipulation,[4, 5] to energy conversion devices.[1, 6] Conventional piezoelectric materials fall into three main categories: 1) inorganic crystals/ceramics with a crystal structure that lacks a center of symmetry. (e.g. quartz,[1, 7] lead zirconium titanate (PZT),[1, 2, 8] and zinc oxide (ZnO)[6, 9]), 2) polymers from both natural and synthetic resources with polar domains (e.g. poly(vinylidinedifluoride) (PVDF),[10] and polysaccharides[11, 12]), and 3) some organic solids of polar molecules.[13] Though they are three different kinds of materials, the origin of the piezoelectric property is, to a large degree, the same.

1.1.1.1 Origin of piezoelectricity

Inorganic crystal and ceramic piezoelectrics

The microscopic piezoelectric origin of inorganic crystal and ceramic piezoelectrics lies in the non-centrosymmetric unit cell.[14] Twenty-one out of the thirty-two point groups of crystals (or structures) are non-centrosymmetric, and of these, twenty are potentially piezoelectric.[15] For example, in PZT (**Figure 1.1, A**), the Zr^{4+} or Ti^{4+} cation sits in the upper middle of the unit cell, creating a small dipole moment. If mechanical stress is applied to the unit cell, the dipole moment will increase or decrease depending on the particular direction of the stress. Such stress induced polarization change is called the direct piezoelectric effect. If an external electric field is applied, the unit cell would stretch or contract. This shape deformation caused by applied electric field is called the reverse piezoelectric effect. In a single crystal or well aligned polycrystal, the effect mentioned above in each unit cell cumulatively gives rise to the macroscopic piezoelectric property of the bulk (**Figure 1.1, D**). Depending on the randomness of the direction of each polar domain, an electric poling process may be needed to line up the polarity of each domain to enhance the overall piezoelectric efficiency of the polycrystalline bulk.

The electric dipole direction is defined as from the negative charge pointing to the positive charge, while molecular dipole moment is conventionally pointing from the positively charged atoms to the negatively charged atoms. In order to avoid confusion between electric dipole and molecular dipole, the direction of all dipoles (P) in this thesis is defined as pointing from the positive charge to the negative.

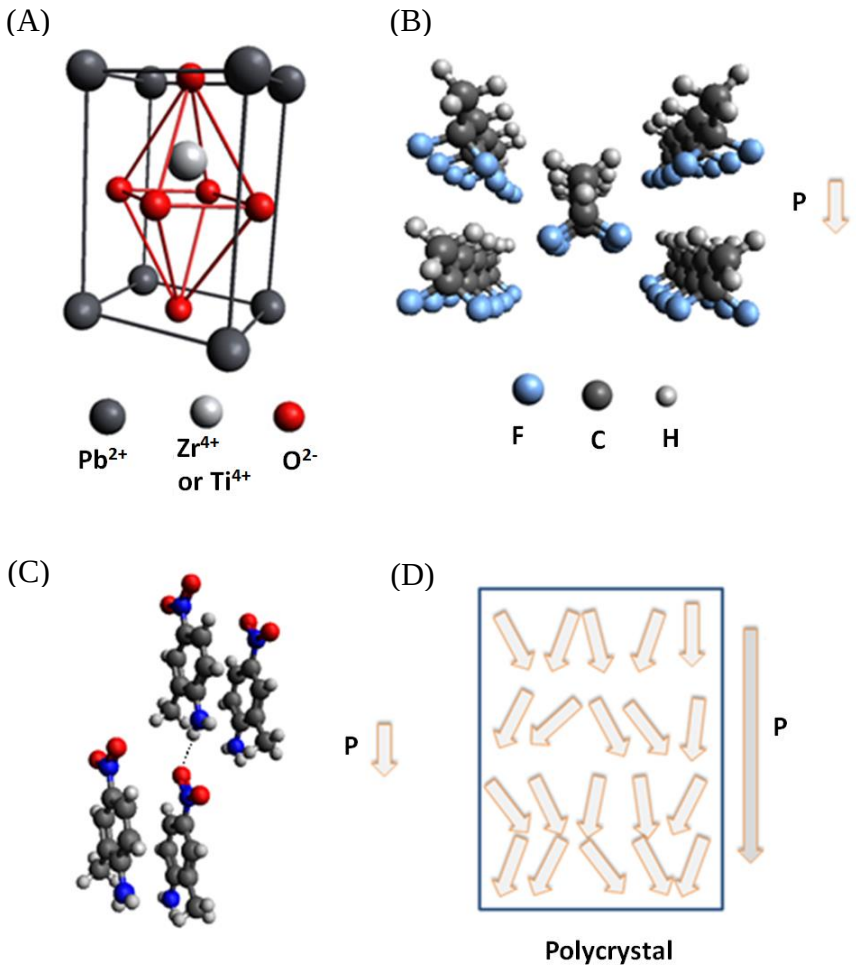

Figure 1.1 Unit cell of lead zirconium titanate (PZT) (A), basic structure of β-phase crystalline polyvinylidene fluoride (PVDF) (B), and crystal structure of 2-methyl-4-nitroaniline (MNA) with intermolecular hydrogen bond indicated (C). When each dipole of the unit cell or basic structure is well aligned, the bulk polycrystal is polar and piezoelectric (D). In order to avoid confusion between electric dipole and molecular dipole, the direction of all dipoles (P) in this thesis is defined pointing from the positive charge to the negative charge.

Piezoelectric polymers

The polymeric piezoelectric family consists mainly of polyvinylidene fluoride (PVDF),[10] polyurea,[16] poly-lactic acid,[17] other synthetic polymers,[18] and biopolymers including polysaccharides[19] and proteins.[20-22] For such polymeric piezoelectric materials the piezoelectric property originates from the aligned polar polymer chain.[23-25] For synthetic polymers (e.g. PVDF) the as synthesized polymer chains are usually randomly oriented, and an electric poling process is required to align the polymer chains.[10] The rotation of the polymer chain dipoles will be restrained within the poled semicrystalline bulk where thicker lamellae helps to produce larger overall polarity.[26] **Figure 1.1, B** illustrates the crystal structure of piezoelectric PVDF. Each aligned polymer chain resembles a polar unit cell of its inorganic piezoelectric counterpart and cumulatively leads to the overall piezoelectric property of bulk polymers.

Piezoelectric organic solids

Several organic crystals are found to be piezoelectric, including the well-known Rochelle salt, Diisopropylammonium Bromide,[27] 2-methyl-4-nitroaniline (MNA),[28, 29] and some other organic crystals.[13, 30] The piezoelectric origin may lie in the molecular polarity and the ordered intermolecular hydrogen bond, as suggested by a recent theoretical study on piezoelectric MNA.[28] **Figure 1.1, C** shows the MNA crystal structure[31] in which hydrogen bonds are formed between the $-NH_2$ groups and nearby $-NO_2$ groups. The change of the hydrogen bond length is responsible for the overall piezoelectric deformation under applied external electric field.

1.1.1.2 Piezoelectric coefficient

One key parameter of piezoelectric materials is the piezoelectric charge coefficient d_{33} (pC/N), which measures the charge density created in pC/m^2 at the materials surface when mechanical

stress in N/m^2 is applied (direct piezoelectricity). The alternative unit is pm/V, measuring the overall shape change in picometer over applied bias in volt (converse piezoelectricity). These two units will be used interchangeably in this thesis.

Another key parameter is the piezoelectric voltage coefficient g_{33} (V • m/N), the ratio of the electric field produced to the mechanical stress applied. It can be calculated from the piezoelectric charge coefficient d_{33},

$$g = d_{33}/\varepsilon \tag{1.1}$$

where ε is the relative permittivity of the material.

Materials with a larger d_{33} will exhibit a larger deformation in response to the same applied field strength over the same thickness. Similarly, higher charge density or higher voltage difference will be created from materials with a larger d_{33} or g_{33}, respectively, with the same applied stress. Materials with a large d_{33} can be used as efficient actuators and charge capacitors, while materials with high g_{33} can be used as highly effective touch sensors.

1.1.2 Basics of conventional ferroelectrics

While piezoelectrics are about the coupling of shape change and external electric field, ferroelectrics place particular emphasis on the coupling of materials polarization and electric field. Materials with intrinsic polarity are ferroelectric if the polarization can be reversed under applied electric field. Such polarization inversion character enables ferroelectrics broader applications such as non-volatile memory[32, 33] multiferroics,[34] capacitors, and charge storage devices.[1] Many materials are piezoelectric and ferroelectric simultaneously, as the electric field

induced deformation usually leads to a polarization inversion beyond a certain level of field strength. PZT, PVDF, and some organic crystal piezoelectrics fall in this category.

Figure 1.2 illustrates the polarization inversion of a PZT unit cell. When a small electric field is applied along the unit cell from top to bottom, the Zr^{4+} (or Ti^{4+}) ion will be forced to move towards the center and the unit cell shrinks in size. Once the strength of the electric field surpasses beyond a certain level (the so-called coercive field), the Zr^{4+} ion will be pushed into the lower half of the unit cell. When the applied field is abolished, the Zr^{4+} ion remains in the lower half of the unit cell and the polarization is reversed compared to the polarization before the field was applied. Such a relative displacement mechanism of ferroelectrics is called the displacive mechanism.

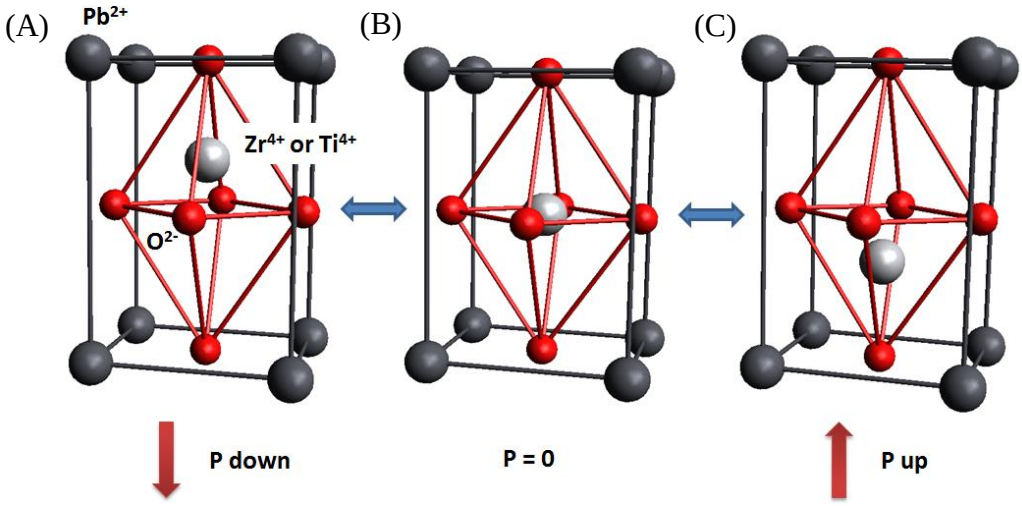

Figure 1.2 Illustration of the polarization inversion of a PZT unit cell. The transition state (B) is not stable. The unit cell is usually polar with the polarity points either downwards (A) or upwards (C). The direction of the polarity in this thesis is defined from the positive charge to the negative to avoid the difference between "electric dipole" and "molecular dipole moment".

Similar to the ion displacement in PZT ferroelectrics, a charged mass migration takes place during the inversion process of ferroelectric PVDF and some ferroelectric organic solids. The polarization reversal is believed to result from the polar chain rotation in PVDF where the dipoles accumulated from C-H and C-F bonds are perpendicular to the polymer chain.[35] The polarization inversion mechanism of organic solid ferroelectrics is mainly typed as 'proton-transfer' where a dynamic proton leads to the hydrogen bond migration (O-H···O to O···H-O).[13]

For all the above mentioned ferroelectrics, structures with the reversed polarization are usually the mirror image of the structures before the inversion. The higher energy of the middle transition state gives a double-well potential diagram (**Figure 1.3**). The inversion energy is defined as the energy difference between the non-centrosymmetric ground state and the centrosymmetric transition state. Note that such an energy barrier could also be overcome by a temperature elevation. For ferroelectric materials, this phase change temperature is called the Curie temperature (T_c), above which materials become nonpolar and paraelectric.

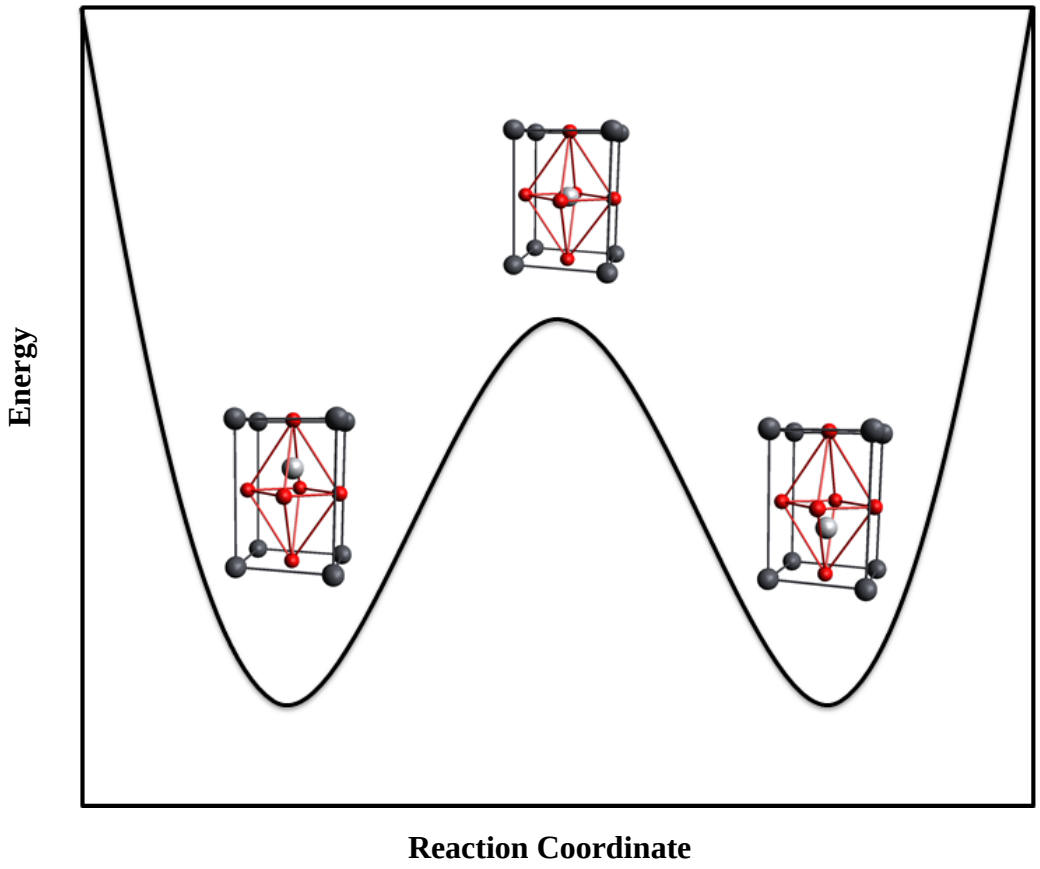

Figure 1.3 Energy diagram of the polarization inversion process of PZT.

1.1.3 Advantages and disadvantages of conventional piezoelectric/ferroelectrics materials

Among all the conventional piezoelectrics, PZT has the highest d_{33} in the range of 300 - 500 pm/V. However, the d_{33} (both measured and theoretical) of PZT can decrease dramatically to far below 100 pm/V as the thickness of the thin film decreases to below hundreds of nanometers, presenting a so-called size effect.[36-38] For example in a work of de la Cruz *et al*. the measured d_{33} of a 140 nm thick film is only 21.2 pm/V,[38] and for ultrathin epitaxial $SrRuO_3/PbZr_{0.2}Ti_{0.8}O_3/SrRuO_3/SrTiO_3$ heterostructures the d_{33} is found to be 60 pm/V and 7 pm/V for a 15 nm and a 5 nm thick film, respectively.[39] This significant drop of d_{33} is believed to result from the internal crystal defects in ultrathin PZT films[40] and a possible transition between the ferroelectric and the paraelectric phase.[41] Such a size effect generally occurs in ceramic piezoelectric materials. Hence, it makes PZT less appealing for making next generation electronic devices at the nanometer scale.

With the concern of lead toxicity, lead-free piezoelectric ceramics have drawn increasing attention in the past two decades.[42-44] The d_{33} of lead-free piezoelectric ceramics is generally smaller than that of PZT. The highest piezoelectric coefficient among the lead-free family currently reported is to 416 pm/V for a solid solution of (K, Na)NbO_3-$LiTaO_3$-$LiSbO_3$.[43] For such lead-free piezoelectrics, usually a high sintering temperature (900-1350 °C) is involved in the synthesis process in order to change the mixed solid salts into relatively uniform crystals.[45] With such a high temperature, *in-situ* growth of such materials on a variety of substrates, especially flexible organic/polymer substrates, becomes impossible. Making flexible devices from lead-free piezoelectric ceramics is thus a large challenge.

Progress has been made on ZnO nanowire piezotronics since the first report of piezoelectric nanogenerators made of zinc oxide nanowire arrays in 2006.[6] The environmental benign nature

of ZnO and the ease of ZnO nanowire fabrication have spread its applications into broad areas covering flexible nanogenerators,[46, 47] self-powered sensors,[48, 49] piezotronic transistors,[50, 51] and some more. The size of a unit ZnO nanowire sample employed in these studies is usually micrometers long with a diameter > 50 nm, which sets the lower dimension limit of ZnO nanowire based devices. So far no group has reported patterned piezoelectric devices made from ZnO nanowires at the nanoscale. Yang *et al*. reported that the dielectric constant of ZnO nanowires decrease from 6.3 to 2.7 when the diameter decreases from 285 nm to 85 nm.[52] The smaller dielectric constant of ZnO (8.66 of bulk ZnO[53]) also limits the potential load over a given thickness. The d_{33} for ZnO is generally small within a range of 9.9 to 26.7 pm/V.[9, 54]

The d_{33} of electrically poled PVDF thin films can reach up to 33 pm/V.[55] Although this coefficient is one factor smaller than that of PZT ceramic piezoelectrics, PVDF is preferable in some applications based on its intrinsic flexibility and light weight. There are a number of ways to make polar PVDF thin films including electric poling and Langmuir-Blodgett (LB) deposition.[56] However, patterned and ultrathin PVDF films have not yet been reported, and thinner films will become less stable in maintaining the overall polarity.[57]

For biological polymers, piezoelectricity has been found in wood, bones, some soft tissues, and even virus components.[22] The piezoelectric coefficient of biomaterials is usually small (<10 pm/V). Few applications have been reported so far partially due to the complexity of biological materials.

1.2 SINGLE MOLECULE PIEZOELECTRIC AND FERROELECTRICS

1.2.1 Single molecule piezoelectrics

Piezoelectrics can be simplified as polar (or charged) springs where mechanical energy is coupled with electric energy (**Figure 1.4**). If a molecule in a spring-like shape is polar along the spring breathing mode, it is then expected to be piezoelectric. All molecules should change shape to some extent in an applied external electric field because of the field-induced polarization. However the level of deformation can be significantly different. We show in this thesis that organic molecules (**Figure 1.5**) with careful design can perform dramatic conformational change in response to an applied field. A large piezoelectric coefficient (d_{33}) of 272 pm/V is predicted for a helicene derivative, significantly higher than that of ZnO and PVDF piezoelectrics and comparable to PZT materials.

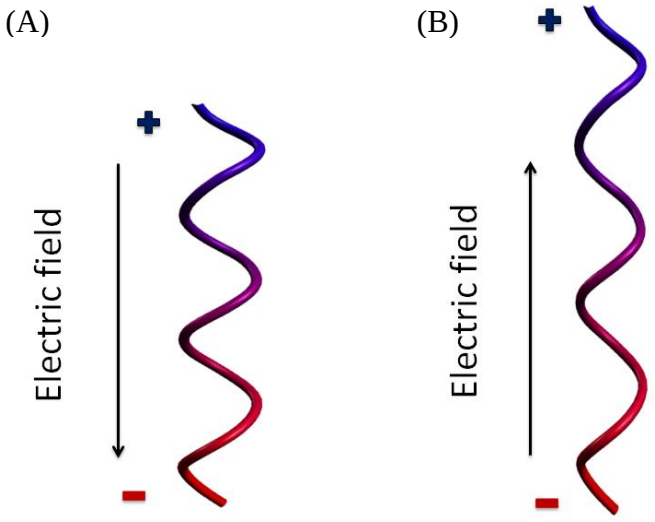

Figure 1.4 Charged springs in an electric field. The spring will contract if the electric field is applied along the dipole (A) and will extend if the field direction is opposite (B).

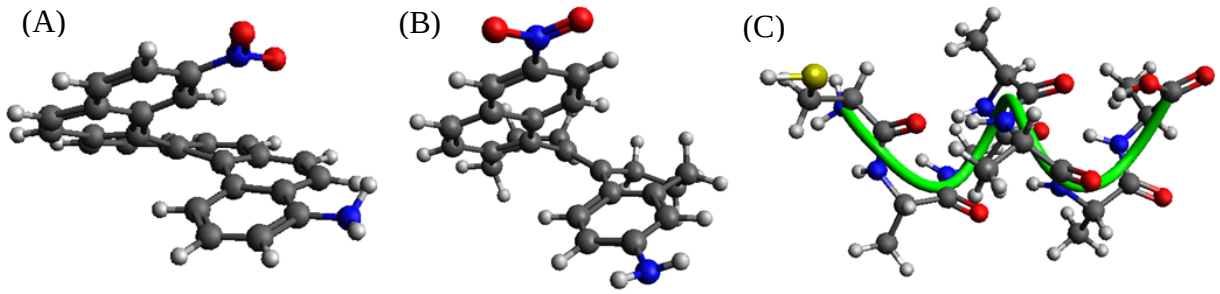

Figure 1.5 Molecular structure of 4-amino-2-nitro[6]helicene (A), 3-amino-8-nitrophenanthrene (B), and oligoaminoacids Cys-$(Ala)_6$. These molecules can be considered as polar molecular springs.

1.2.2 Single molecule ferroelectrics

Some disadvantages of conventional piezoelectric materials, such as rigidity, toxicity, and difficulty in synthesis, are inherent to ferroelectric applications as well. The advantage of building ferroelectric devices from single molecules is that a much smaller scale (<10 nm) can be approached both in film thickness and film size. Similar bottom-up strategy can be used to order single molecule into smaller usable units, which could dramatically enhance the ferroelectric performance in real applications (e.g. ferroelectric random-access memory (FeRAM)[32] with higher storage density).

The molecular dipole moment of piezoelectric oligoaminoacids is not likely to reverse under mild electric field. The reversed polarization in z-axis of piezoelectric helicenes and phenanthrenes under large electric field will not remain after the field is abolished. So these three kinds of molecules are thus not likely to be ferroelectric. Possible ferroelectric single molecules require a structure that is polar and can convert between two stable conformations with opposite dipoles. While single molecule piezoelectrics are abstracted as polar/charge springs, we relate single molecule ferroelectrics to polar invertible bowls (**Figure 1.6**).

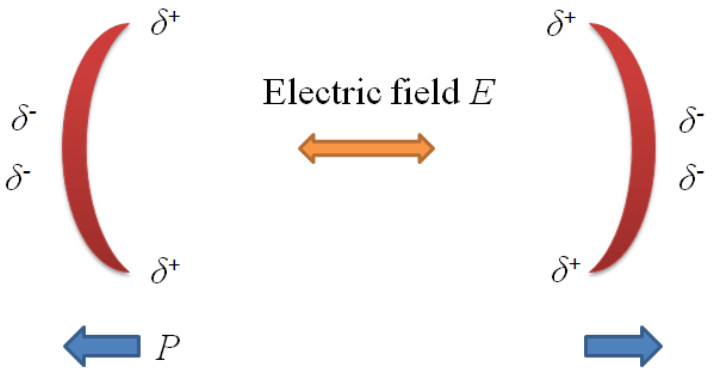

Figure 1.6 Polar flexible bowls and bowl-to-bowl inversion in an electric field.

Sumanenes and corannulenes are two typical nonplanar bowl-shaped molecules which can be considered as fullerene (C_{60}) fragments (**Figure 1.7**). Such bowl-shaped molecules are also called "buckybowls". Both sumanene and corannulenes can perform a bowl-to-bowl inversion above a certain temperature and in a relative free state (e.g. room temperature in solution). Such inversions have been studied by both computational and experimental means.[58-60] An energy barrier between the curved bowl and the planar transition state must be overcome for a possible inversion. If the inversion of the polar buckybowls can be achieved by an applied electric field, they could be potential single molecule ferroelectrics.

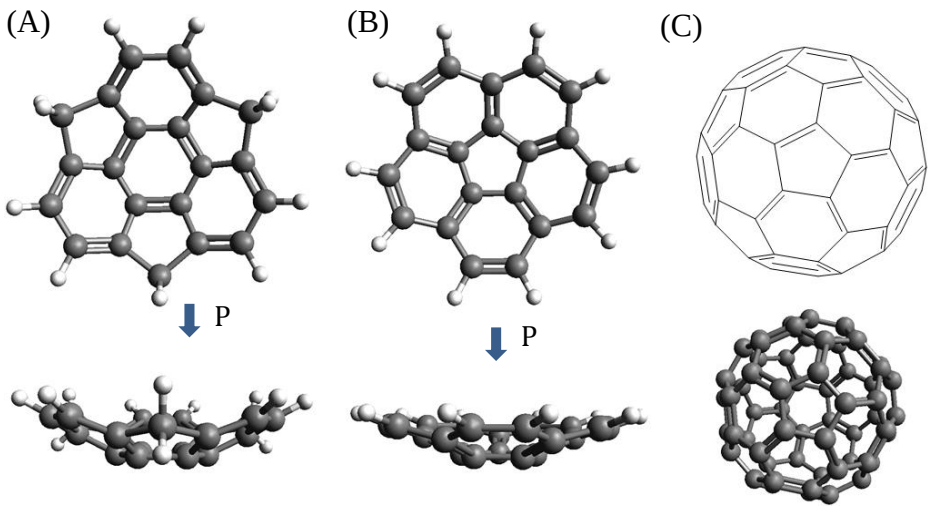

Figure 1.7 Molecular structures of sumanene (A), corannulene (B) and fullerene (C). The molecular dipole moment of sumanene and corannulene points from the center of the rim to the center of the bottom.

1.3 OBJECTIVES AND OUTLINES

The objectives of this dissertation are to: 1) demonstrate the concept of single molecule piezoelectrics and single molecule ferroelectrics using density functional theory (DFT) calculations; 2) describe design rules for good single molecule piezoelectrics and ferroelectrics; 3) demonstrate single molecule piezoelectricity via piezoresponse force microscopy (PFM) and Fourier-transform infrared spectroscopy (FTIR) methods via samples of self-assembled monolayers of one of our proposed single molecule piezoelectrics; and 4) describe primary synthesis of helicene single molecule piezoelectrics.

The thesis is organized as follows:

Chapter 2 presents a theoretical examination on three types of piezoelectric single molecules (asymmetrically substituted [6]helicenes, asymmetrically substituted phenanthrenes, and several oligoaminoacids) using mainly density functional theory (DFT) calculations. Regiochemistry, effects of dipole moments, polarizability, and steric interactions are examined to conclude design rules for good single molecule piezoelectrics.

Chapter 3 presents an experimental demonstration of the piezoelectric property of a self-assembled monolayer of our targeting oligoaminoacids using piezoresponse force microscopy (PFM) and surface Fourier-transform infrared spectroscopy (FTIR). Experiment methods and sample fabrication will be discussed in detail. Synthesis of an asymmetrically substituted [6]helicene is included after the summary of the PFM results.

Chapter 4 studies the single molecule ferroelectrics, a conceptual extension to single molecule piezoelectrics. Several buckybowls (both reported and hypothetical) are examined via DFT calculations. Similar to single molecule piezoelectrics, we study the effect of molecular structure, functional groups, and dipole moment of the buckybowls to their inversion field.

Chapter 5 concludes this thesis and provides future outlook for further improvement and potential applications of single molecule piezoelectrics and single molecule ferroelectrics.

Appendix A includes the synthesis of an asymmetrically substituted [6]helicene 3-bromo-14-methoxo[6]helicene (**3b14m**).

Appendix B includes the attempt of flexible piezoelectric devices based on single molecules.

2.0 CALCULATIONS OF SINGLE MOLECULE PIEZOELECTRICS

This work, written in collaboration with Christopher W. Marvin, Leah Seebald, and Geoffrey R. Hutchison*, was, in part, published as *J. Phys. Chem. C*, **2013**, 117 (33), 16783–16790.

Xinfeng Quan, Christopher W. Marvin, and Leah Seebald, performed the calculation and analysis of substituents and polarization effects of helicenes and phenanthrenes.

2.1 INTRODUCTION

Computational chemistry has become a great tool for structure-property evaluation of molecules and solids. Although exact analytical solutions are absent for many-body quantum problems, predictions for relative small molecules can be close enough to experiments to reliably predict low-energy geometries, dipoles, charge distributions, vibrational frequencies, and some other properties. Calculations can save time in the real experiments as poor candidates could have been screened out.[61] A much larger number of possible molecule structures can be examined no matter if the molecule is synthetically available or not. Some molecule properties may be easier to obtain from calculation. We will use computational tools to study single piezoelectric molecules and to guide current and future experimental work.

All molecules should change shape in an applied external electric field due to field induced polarization. However the level of deformation can be significantly different. Only those with tremendous shape change in a linear fashion are potential piezoelectric candidates. Three prototypical single molecule piezoelectrics proposed in this dissertation are asymmetrically substituted [6]helicenes, asymmetrically substituted phenanthrenes, and oligoaminoacids. Being intrinsically polar and spring-like or in shape, those molecules perform a large deformation under an applied external electric field, as we show in this chapter.

Molecular details such as regiochemistry, dipole moment, functional groups, and polarizability will be discussed in detail as key factors of good single molecule piezoelectrics, especially in the case of helicenes and phenanthrenes (**Scheme 2.1**).

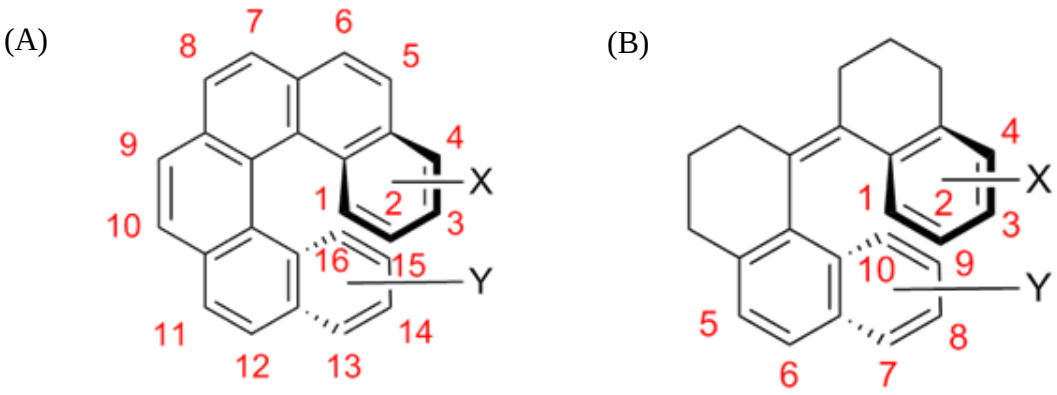

Scheme 2.1 Asymmetrically substituted [6]helicene (A) and tetrahydrophenanthrene (B), including atom numbering, where –X and –Y are representative of electron donating and electron withdrawing substituents, respectively.

2.2 COMPUTATIONAL METHODS

We used Gaussian 09[62] and density functional theory (DFT), with the B3LYP functional[63, 64] and the 6-31G(d) basis set to optimize all computed structures. DFT methods are known to be asymptotically incorrect and ignore dispersion,[65-71] several other functionals, including B97D,[72] CAM-B3LYP,[73] PBE1PBE,[74] and ω-B97XD,[75] were employed to check consistency. Each functional predicts a different piezoresponse of helicenes and phenanthrenes.[76] Since no experimental data yet exists for comparison, and the trends from each functional appear consistent across different molecules, we used the B3LYP method and focus mainly on the structure/property relationships and the computed geometric deformations. Our group has compared computed to experimental piezoelectric coefficients of crystalline 2-methyl-4-nitroaniline, and high agreement was found between computational and experimental piezoelectric responses (in hydrogen bonding interactions) when using the B3LYP functional.[77]

To consider the geometric deformation under an applied external electric field, the molecule was oriented to a specific frame of reference using Avogadro,[78] and the specified direction and magnitude of the field was added to the Gaussian input (**Table A1** and **Figure A6**). Since small local minima geometries exist (e.g., with inverting the pyramidal $–NH_2$ group), all resulting optimized geometries were checked for consistency with the lowest energy geometry. Optimized structures were also compared with identical calculations performed using Q-Chem 3.2[79] to ensure results were not dependent on the geometry optimization algorithm or implementation. In both cases, the implementation is built-in and the effect of the applied electric field directly modulates forces, gradients, etc. Unless otherwise specified (i.e., for examination of the direct piezoelectric effect), no constraints were applied to the optimization. Since optimization occurs in the 3N-6 internal degrees of freedom, translations and rotations of the frame of reference can

be removed by select choice of coordinates. We find that even with automatic selection of internal coordinates from Cartesian coordinates, only small (less than 1-3°) rotations occur.

The piezoelectric coefficient is a tensor derived from the direction of the applied field and the resulting molecular geometric distortion. We restrict our discussion to the largest such contribution, and the piezoelectric coefficient, d_{33}, was calculated from the molecular length at maximum extension (l_{max}) and at zero applied field (l_{zero}) using **Equation 2.1:**

$$d_{33}\left[\frac{pm}{V}\right] = \frac{(l_{max} - l_{zero})}{(l_{zero})} \times \frac{1}{field}\left[\frac{nm}{V}\right] \times 1000\left[\frac{pm}{nm}\right] \quad (2.1)$$

Note that while this formula suggests a linear response of the piezoelectric distortion to the applied electric field, there is no guarantee that all molecules will exhibit linear electromechanical response in all electric field range examined. One can imagine, for example, conformationally restricted species that cannot extend or contract due to steric crowding or other large energetic barriers. While the choice of a frame of reference is potentially arbitrary in single molecules, unless specified, we have defined the z-axis of the molecules to approximate the lowest energy vibrational breathing mode, as discussed below.

Calculation of the molecular volume was performed by simple Monte Carlo estimation of the van der Waals volume, determining the ratio of points inside and outside the van der Waals surface of the molecules.[76]

2.3 RESULTS AND DISCUSSIONS

2.3.1 Asymmetrically substituted [6]helicenes

We first discuss the substituted fully conjugated [6]helicenes and build a set of structure/property correlations. We will describe different regiochemical isomers using amino and nitro substituents, functional group substitutions in the 4- and 15- position, along with dipole moment and polarizability contributions to potential energy. The electric field was applied along the direction of C2 to C15, **Scheme 2.1**, and is defined as the z-axis of the system. The field was varied between ±1.29 V/nm, large on macroscopic terms, but small on an atomistic scale, corresponding to the field due to an extra positive or negative charge at 1.06 nm from the molecule. Over the field range, the distance between the two nitrogen atoms was predicted to vary from 4.869 Å to 5.480 Å (corresponding to -1.29 V/nm and +1.29 V/nm applied field, respectively) as illustrated in **Figure 2.1**. This deformation of 0.61Å corresponds to ~12.5 % length change and a computed piezoelectric constant d_{33} of 48.8 pm/V, comparable to 9.9~26.7 pm/V for ZnO piezoelectric materials.[9, 54] Such a large d_{33} implies that much smaller fields, comparable to conventional piezoelectrics, can be used in experiments or practical applications. Between atoms C2 and C15, a deformation of 0.22Å also occurs, as illustrated in **Figure 2.2**, indicating that the molecule performs a complete structural change beyond a simple bending of the C-N amine and nitro groups. Molecules will be referenced so that position and functional group are clear, such as 4-amino-15-nitro[6]helicene is **4a15n**.

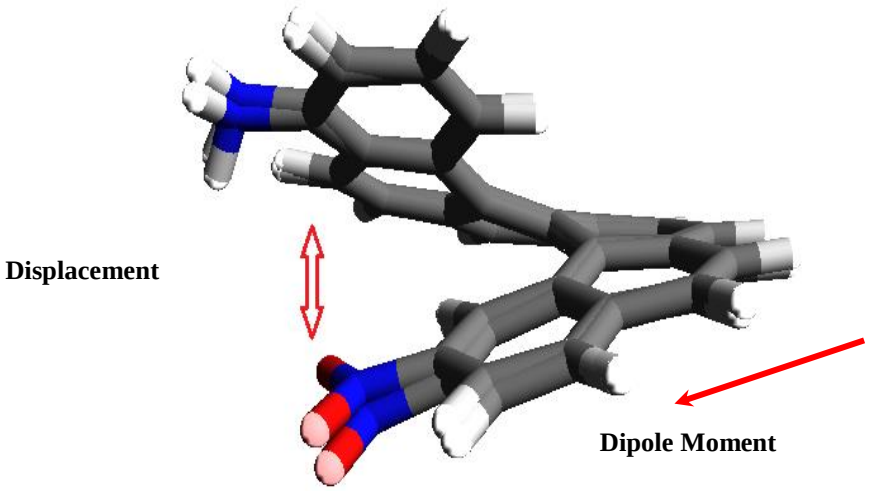

Figure 2.1 Superposition of [6]helicene 4a15n under two levels of applied field strength (±1.29 V/nm).

(A)

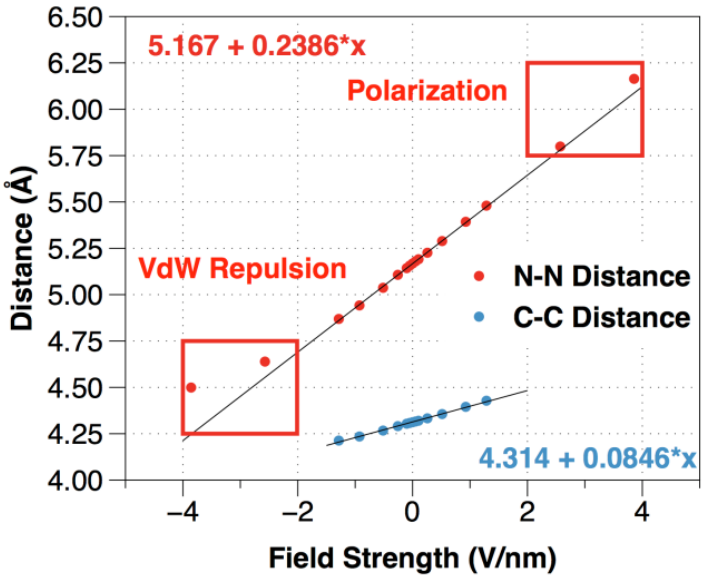

(B)

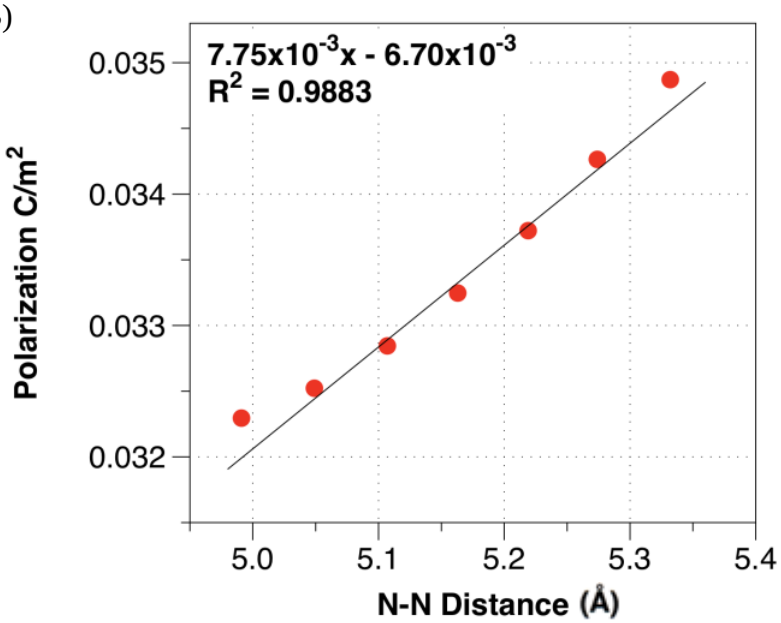

Figure 2.2 (A) Calculated N to N and C2 to C15 distances in 4a15n under different applied external electric fields demonstrating the converse piezoelectric effect. Note that while the deformations are largely linear across the field strengths studied; some curvature does occur at high positive and negative applied fields. (B) Calculated polarization (dipole moment per volume) in 4a15n at different constrained geometries, demonstrating the direct piezoelectric effect. Similar nonlinearities are found at large deformations.

As observed in **Figure 2.2 (A)**, molecules exhibit a converse piezoelectric effect (strain induced by electric field), and while the variation in displacement is largely linear with applied external field, at large positive and negative fields some nonlinearity is found. During the contraction with a negative field, the molecular length begins to saturate beyond -1.29 V/nm because of van der Waals repulsion between atoms in the helicene. As the molecule extends with a large positive field, the π-electron polarization increases and slightly increases the deformation above linear response for fields beyond +1.29 V/nm.

Similarly, **Figure 2.2 (B)** demonstrates a direct piezoelectric effect (polarization induced by strain), found by calculating both the molecular dipole moment and van der Waals volume to give a polarization, at specific geometric distortions. For each N-N (or C2-C15) distance, the two carbon atoms were set to a specific displacement and "frozen" for a constrained geometry optimization while all other atoms relaxed. While the dipole moment derives from separated charges, partial charges clearly redistribute as the conformation changes, yielding some nonlinearity, particularly at large geometric distortions. Thus single molecules clearly exhibit both direct and converse piezoelectric effects. In this thesis, we discuss mainly the converse effect, since its calculation does not require arbitrary geometric constraints.

The piezoelectric response of the molecule is due to coupling between the molecular dipole moment and the applied field, which changes the potential energy surface of the molecule and creates geometry with a new global minimum energy. **Equation 2.2** describes the energy change upon interaction with an external electric field of these systems: μ is the dipole moment, ($C\ m^{-1}$); $\vec{F}$ is the applied electric field, ($V\ nm^{-1}$); α is the polarizability of the molecule ($C^2\ m^2\ J^{-1}$); and β is the hyperpolarizability, ($C^3\ m^3\ J^{-2}$):

$$E(F_z) - E(F_z = 0) = -\mu_z F_z - \alpha_{zz} {F_z}^2 - \beta_{zzz} {F_z}^3 \quad (2.2)$$

For the 4-amino-15-nitro[6]helicene (**4a15n**), the calculated energy change is 4.6 kJ/mol with 59 % and 41 % contributed from the dipole moment and polarizability, respectively and only 0.07 % from the hyperpolarizability.[76]

If we assume this energy excites only the lowest-energy breathing mode of the helicene (computed frequency of 31.4 cm^{-1} and computed force constant of 0.0045 mdyne $Å^{-1}$), the overall harmonic deformation would be over 1.84 Å! Clearly, multiple vibrations are excited, and immense electromechanical response is possible even with a relatively small potential energy change (4.6 kJ/mol). **Figure 2.3** illustrates the non-monotonic change of the overall molecular dipole moment. At about -0.5 V/nm, the dipole moment reaches a minimum and increases as electric field increases or decreases. This effect derives from the near-orthogonality of the applied electric field and the dipole moment, illustrated in **Figure 2.1**. If each component of the dipole moment is considered (as in **Figure 2.3**), the z-axis component is affected most by the applied field, and at large field strength, dominates the overall dipole moment.

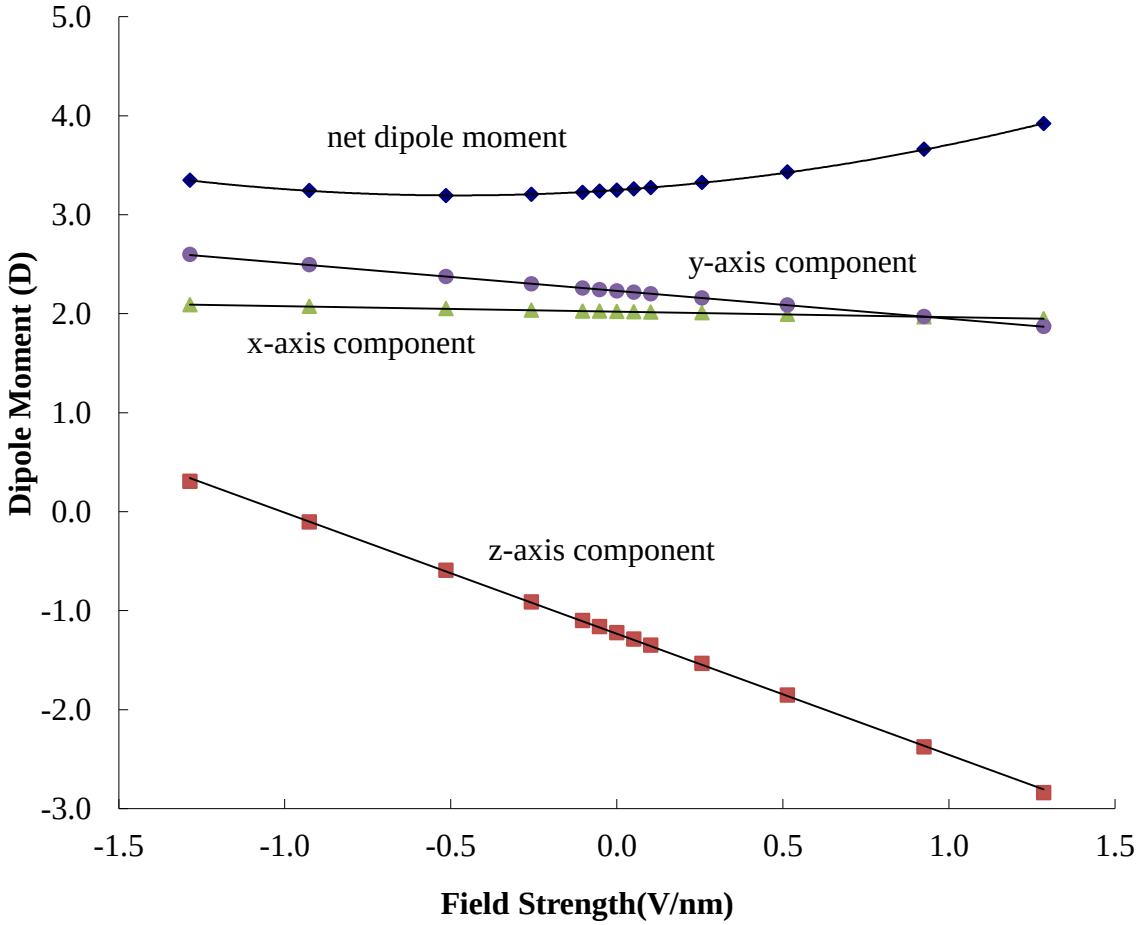

Figure 2.3 The computed net dipole moment along with the x-, y-, and z-axis components for **4a15n** under different applied electric fields. Note that while the x-axis component is the largest in magnitude, it is not significantly affected by the applied field along the z-axis.

2.3.1.1 Regiochemical isomers

Beyond **4a15n,** all 16 amino-/nitro- regioisomers of [6]helicene, reflecting substitution at each of the 4 free positions of both the "top" and "bottom" rings in **Scheme 2.1**, have been studied for their predicted piezoelectric response. For each isomer, the geometry was optimized by varying the applied external electric field as described above. The electric field was applied along the direction of C2 to C15 for each regioisomer, since it gives the largest deformation under the same electric field strength (**Figure A7**). The length changes described are defined as the average change in length between the substituents from the molecule at 0 V/nm applied field to the lengths at ±1.29 V/nm. In all cases, a length deformation was found proportional to the magnitude of the field and the predicted piezoelectric coefficients are compiled in **Table 2.1**.

Table 2.1 Computed piezoelectric coefficient d_{33} of 16 isomers of amino- and nitro- substituted [6]helicenes. Field is applied along C2 to C15 and within the range of ±1.29 V/nm.

Isomer	**1a13n**	**1a14n**	**1a15n**	**1a16n**	**2a13n**	**2a14n**	**2a15n**	**2a16n**
d_{33} (pm/V)	12.7	10.5	7.4	1.8	39.9	37.0	23.1	6.7
Isomer	**3a13n**	**3a14n**	**3a15n**	**3a16n**	**4a13n**	**4a14n**	**4a15n**	**4a16n**
d_{33} (pm/V)	23.5	44.7	36.7	6.1	13.5	23.7	48.8	8.3

The molecular geometry plays a large role in determining the overall deformation potentials. For example, in isomer **1a16n**, substituents on C1 and C16 are extremely close and likely form an intramolecular hydrogen bond between the $-NH_2$ and $-NO_2$ groups, restraining the molecule from significant contraction (due to steric repulsion) or extension, giving the smallest response in the series, 1.8 pm/V. Retaining only one substituent on C1 or C16, as in the isomers **1a15n**, **1a14n**, **1a13n**, **2a16n**, **3a16n** and **4a16n**, allows larger space for the molecule to extend and contract, so larger deformation is observed. The five isomers that exhibit a maximum deformation above 30 pm/V are **2a14n** (37.0 pm/V), **3a15n** (36.7 pm/V), **2a13n** (39.9 pm/V), **3a14n** (44.7 pm/V) and **4a15n** (48.8 pm/V). In these molecules, the two substituents are along the lowest energy breathing mode, yielding a large z- component of the dipole moment and little steric repulsion.

For anisotropic properties such as piezoelectric response, the deformation of a material depends not only on the strength of the applied field, but also on the direction. We considered applied fields along multiple directions, since each molecule is inherently asymmetric, using field strengths between ±1.29 V/nm. Larger deformations take place when field is applied along or close to the z-axis, along the molecular breathing mode, see **Figures A1** and **A2**. So for most of the 16 isomers, the largest deformation occurs when the field is applied along the C2 to C15 axis.

2.3.1.2 Dipole moment

To optimize single-molecule piezoelectric response, one might imagine a larger dipole moment would give a larger geometric distortion. As discussed above, only the z-component of the dipole

moment is directly coupled to the applied field, and in the 16 regiochemical isomers considered here, it is only a small component of the overall dipole moment. Consequently, there is little correlation between the molecular dipole moment and the deformation, or even in the magnitude of the z-component. As illustrated in **Figure 2.4**, there is some small correlation between the *fraction* of the overall dipole moment in the z-direction at zero applied field and the piezoelectric deformation.

(A)

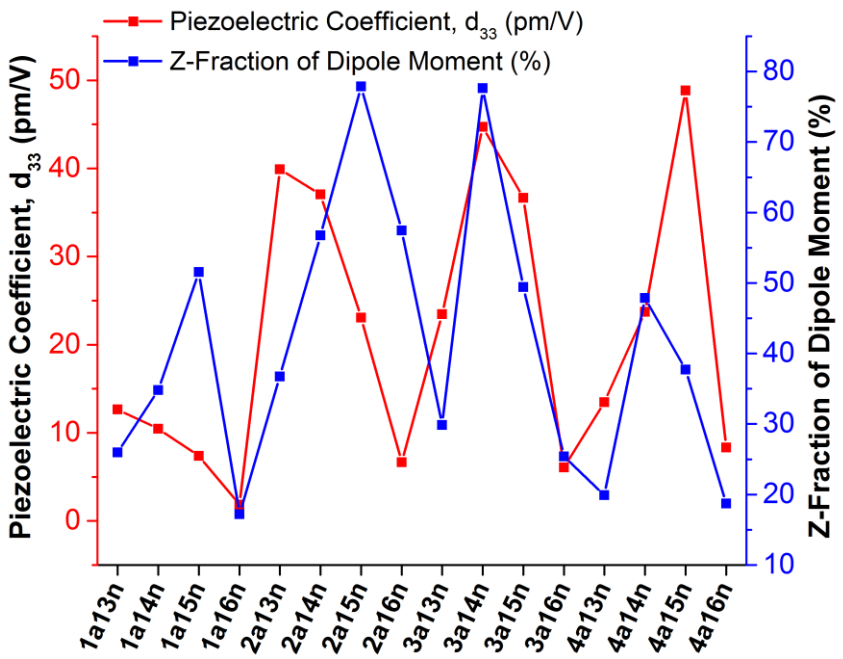

(B)

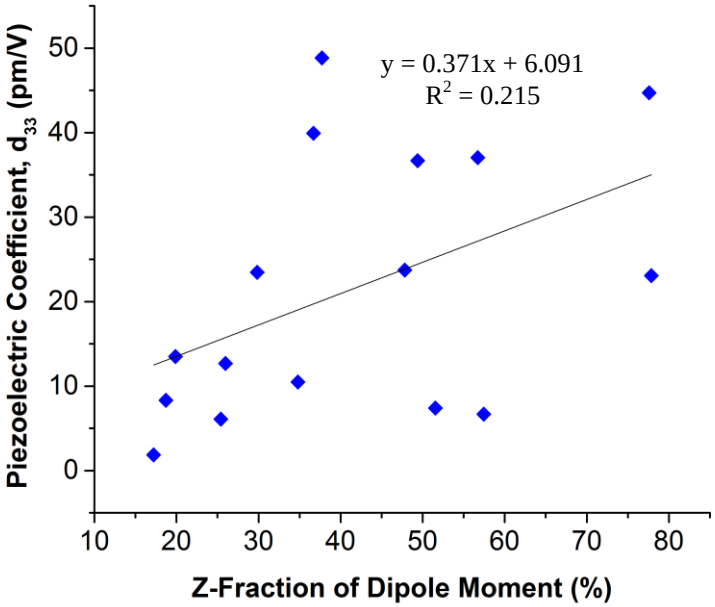

Figure 2.4 (A) Calculated dipole moment (i.e. fraction of the total magnitude aligned with the z-axis) and maximum response of the 16 [6]helicene isomers considered. (B) There is a small correlation between z-fraction of dipole moment and calculated deformation for [6]helicene regioisomers. Field is applied along C2 to C15.

2.3.1.3 Functional groups

Several activating and deactivating functional groups with varying strength were studied, resulting in 36 different 4- and 15- substituted [6]helicenes using a combination of 6 electron withdrawing and 6 electron donating groups, with computed piezoresponse compiled in **Figure 2.5**. Although IUPAC numbering would change depending on what functional group is attached to the helicene, the numbering will be kept consistent with **Scheme 2.1** to limit possible confusion. Hammett-Taft parameters were used for the σ_{meta} constants to determine the difference in electronic directing character.[80, 81] Functional groups with a larger Hammet-Taft constants ($\Delta\sigma_{meta}$) tend to yield larger piezoelectric response.[76] However, the combination of a strong electron withdrawing group and a strong electron donating group doesn't insure a large z-fraction of dipole moment. The relationship of deformation and z-fraction dipole moment is vague in these isomers, but with a stronger electron withdrawing group and stronger electron donating group, the z-fraction of dipole moment changes less, which means those molecules favor a shape deformation rather than charge redistribution under the applied field.

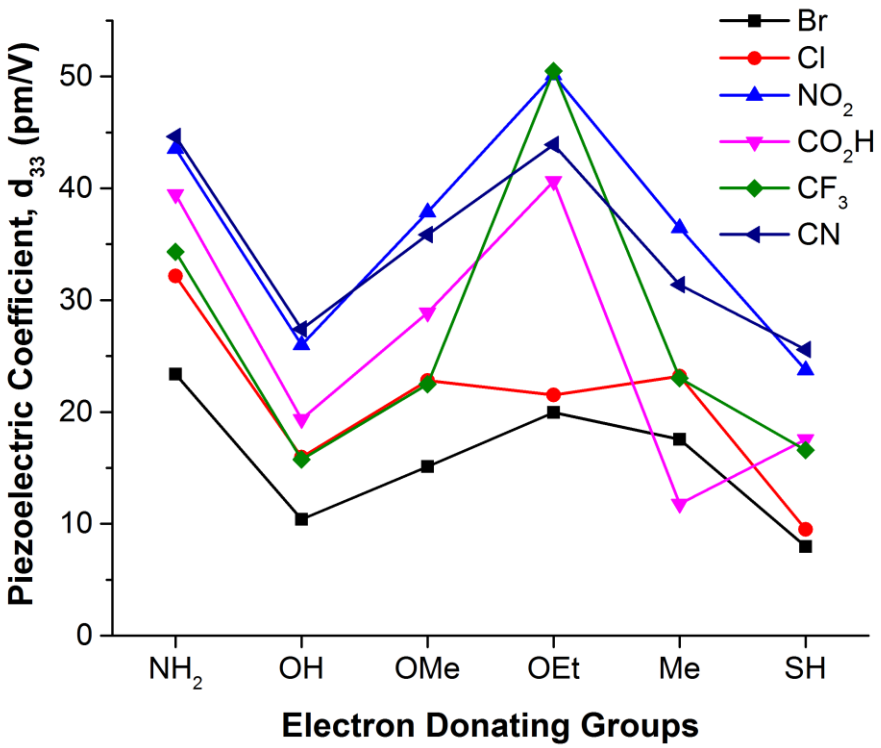

Figure 2.5 Calculated piezoresponse (d_{33}) of 4- and 15- substituted [6]helicene. Nitro- and cyano- substituted [6]helicenes have higher overall responses for the electron withdrawing groups, while the amino substituted [6]helicene has the highest average deformation for the electron donating groups. Figure is adapted from Ref.[76]

2.3.1.4 Polarizability

The regiochemistry clearly complicates the correlation of molecular dipole moment and computed piezoresponse. The high degree of correlation, however, between the difference in Hammett parameters and predicted piezo coefficient suggests that higher dipole moments generally yield greater geometric deformation. **Figure 2.6** shows the relationship between computed polarizability and deformation of the 16 amino- and nitro- substituted helicenes. While the correlation is slightly higher than with the dipole moment, the regiochemistry also complicates the response. Instead, one can consider a series of elongated helicenes, adding more fused benzene rings to linearly (i.e., rather than helically) extend the helicene. Such "clamphenes" show dramatically increased geometric deformation (**Figure 2.7**), deriving largely from their increased polarizability.

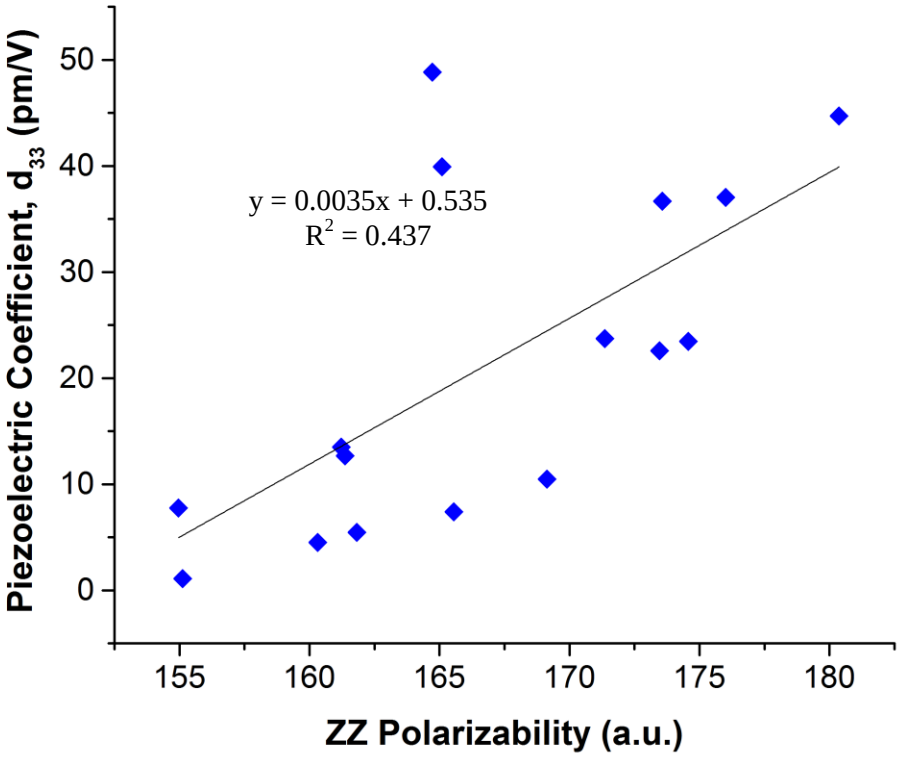

Figure 2.6 Using the ZZ polarizability data from the regiochemical computations, it can be seen that as the polarizability of the [6]helicene system correlates with the piezoelectric response.

As an example, hypothetical helicene derivatives are proposed for single molecule piezoelectrics with high response, illustrated in **Figure 2.7 (A)**. This molecule could be considered as adding a naphthalene group to both ends of a [6]helicene, increasing the "arm length" and thus the linear distortion along the z-axis. For the clamp-like shape of the molecule, we name it 5-amino-20-nitro "clamphene" (**CP10-5a20n)**, shown in **Figure 2.7 (B)**. As with the [6]helicenes, under an applied electric field range of ±1.29 V/nm, the computed distance between the two nitrogen atoms extends from 9.31 Å to 10.94 Å, yielding an 18 % length deformation, and a computed d_{33} of 136 pm/V, comparable to many inorganic piezoelectric materials.[1, 2] As the arm length is further extended, the calculated d_{33} increases to an even larger number (**Figure 2.8**). For example, d_{33} of 272 pm/V can be achieved if four phenyl rings are added.

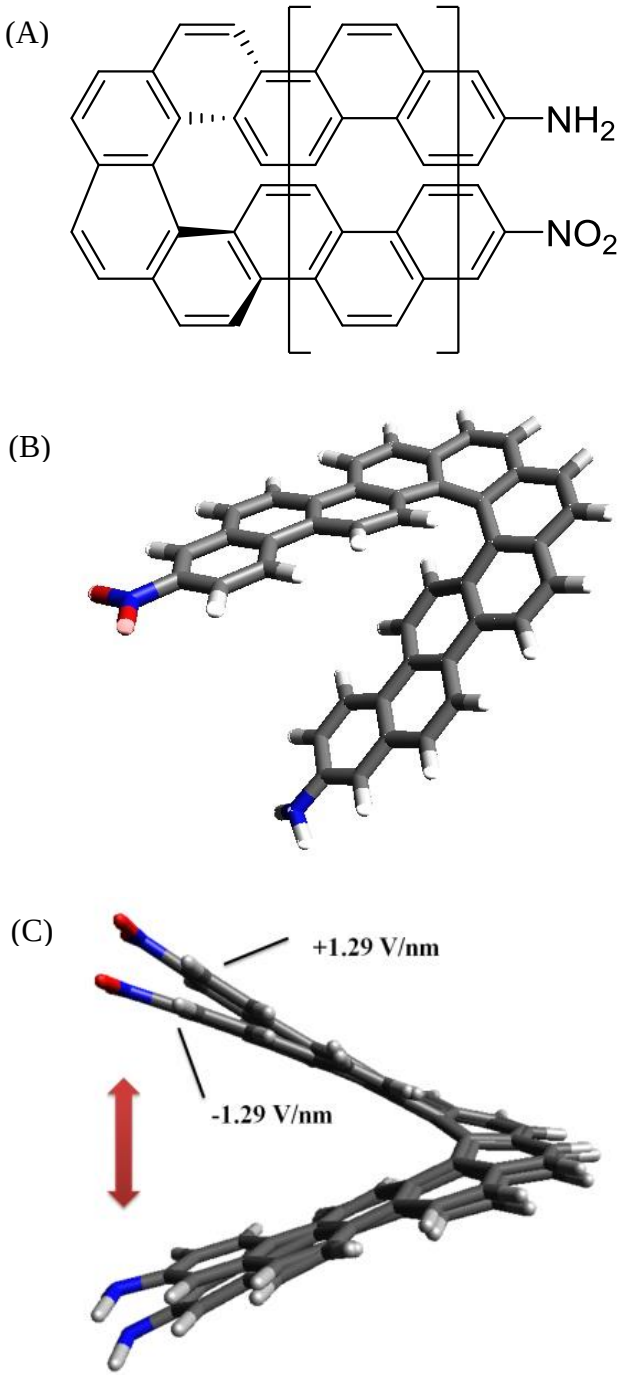

Figure 2.7 (A) Extended –arene used for polarizability and upper-limit calculations. (B) Example "clamphene" 5-amino-20-nitro "clamphene" (CP10-5a20n), and (C) computed deformation of CP10-5a20n.

(A)

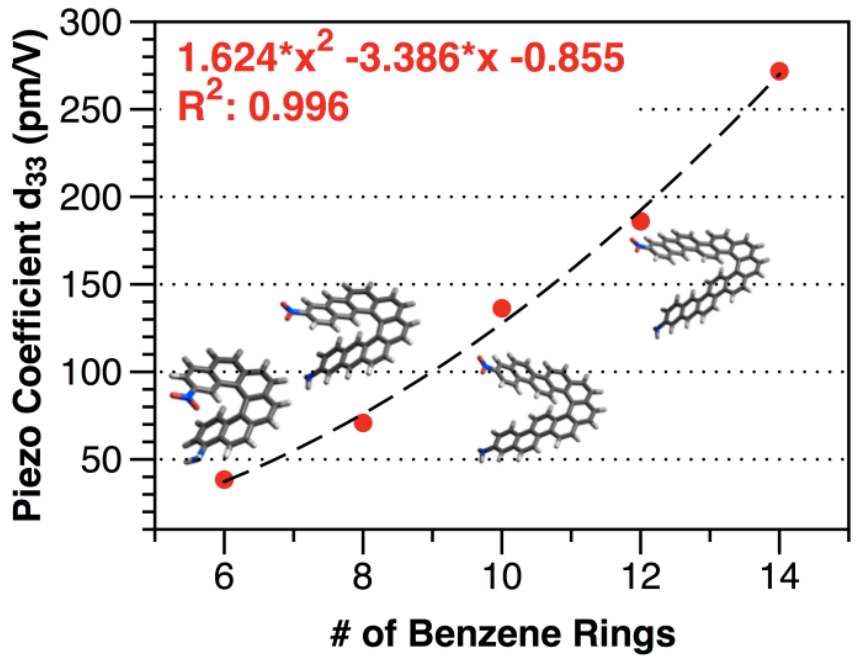

(B)

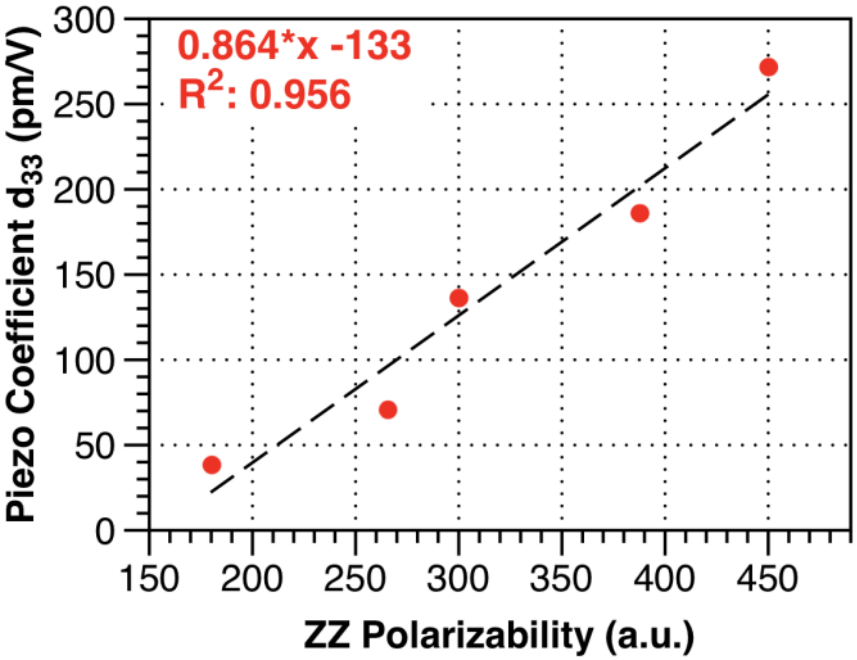

Figure 2.8 Increased computed geometric deformation (A) as a function of the number of benzene rings in the clamphenes and (B) as a function of the computed zz-component of the polarizability.

2.3.2 Asymmetrically substituted phenanthrenes

The tetrahydrophenanthrene system is obviously a more flexible hinge due to the lack of conjugation in part of the system and the incomplete ring system allowing for larger piezoelectric deformations through a rotation around the double bond, but with the downside of potential *cis/trans* isomerization. For the phenanthrenes, a field is applied along C2 to C9 on which lies the breathing mode of the molecules. The same field range as [6]helicene, ±1.29 V/nm, is applied for all molecules studied. The distance between the first atoms on each functional group is used in the determination of the piezoelectric response. In terms of regiochemistry, polarizability, dipole moment, and functional group, the behavior of the substituted phenanthrenes under applied electric field is similar to that of substituted helicenes.

Similar to the [6]helicene above, the piezoelectric response of these phenanthrene molecules is due to the coupling of the molecular dipole moment to the applied electrical field, which modifies the potential energy surface of the molecule and creates a new global potential energy minimum. Using **Equation 2.2**, the potential energy of the 3-amino-8-nitro-phenanthrene, **3a8n,** is 4.4 kJ/mol, with a contribution of 55% from the dipole moment and 45 % from the polarizability, slightly higher than the calculated contributions for [6]helicene.

As with the [6]helicene above, if we take into account only the lowest energy breathing mode (computed frequency of 27.7 cm^{-1}, and computed force constant of 0.0030 mdyne $Å^{-1}$), the overall harmonic deformation would be over 2.21 Å. Even though the potential energy change is relatively small (4.4 kJ/mol), a large electromechanical change is possible, but again, multiple vibrational modes are excited at once.

2.3.2.1 Regiochemical isomers

All 16 possible combinations of regiochemical isomers comparable to [6]helicene were tested for the phenanthrene. The geometry was optimized as described for the [6]helicene above. A larger piezoelectric response is noted for regiochemical isomers where the functional groups are along the breathing mode of the molecule and smaller responses are noted for molecules with the functional groups close to the center of the system as shown in **Table 2.2**.

Table 2.2 Computed piezoresponse (d_{33}) of 16 isomers of amino- and nitro- substituted phenanthrenes using an applied field of ±1.29 V/nm along C1 to C10.

Isomer	**1a7n**	**1a8n**	**1a9n**	**1a10n**	**2a7n**	**2a8n**	**2a9n**	**2a10n**
d_{33} (pm/V)	17.9	14.5	8.6	1.1	40.9	34.2	21.9	2.7
Isomer	**3a7n**	**3a8n**	**3a9n**	**3a10n**	**4a7n**	**4a8n**	**4a9n**	**4a10n**
d_{33} (pm/V)	32.7	47.4	42.4	8.2	18.2	32.1	59.7	10.2

The molecular geometry plays a similar role in the phenanthrene system as it does in [6]helicene. A response greater than 40 pm/V is predicted for four of the isomers: **2a7n** (40.9 pm/V), **3a9n** (42.4 pm/V), **3a8n** (47.4 pm/V), and **4a9n** (59.7 pm/V). The substituents for these high deformation isomers are aligned mostly parallel with the applied field likely leading to a large affect from the field. The small responses, less than 10 pm/V, seem to be due to the increased distance between the substituents and the misalignment between the field and the functional groups.

2.3.2.2 Dipole moment

Just as [6]helicene, the z-component of the phenanthrene is directly coupled to the applied field. As seen in **Figure 2.9**, there is a much larger correlation between the z-fraction of the dipole moment for the phenanthrene and its piezoelectric response than [6]helicene. Of the 16 regiochemical isomers studied here, 13 have a contribution of over 50 % from the z-component of the dipole moment.

(A)

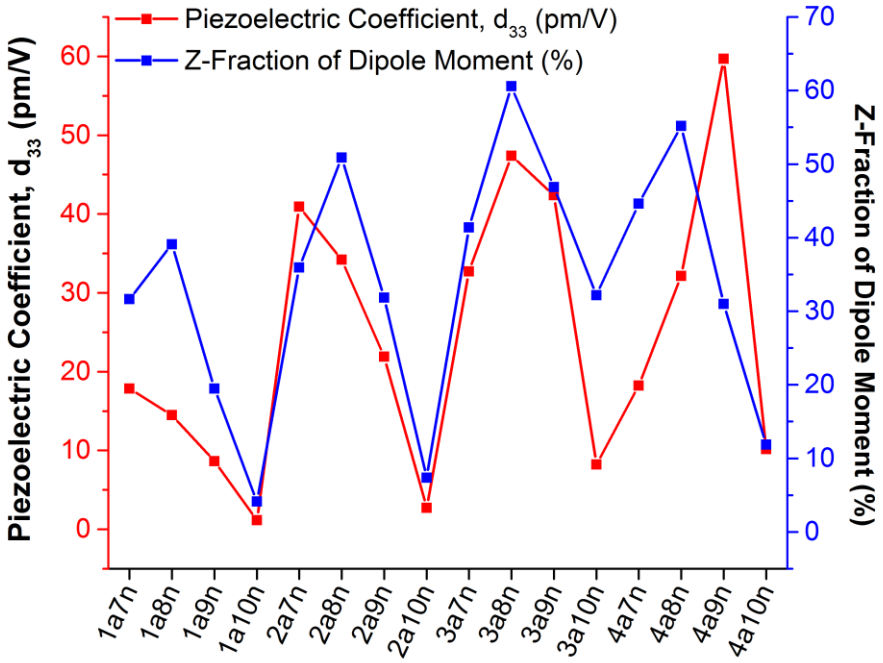

(B)

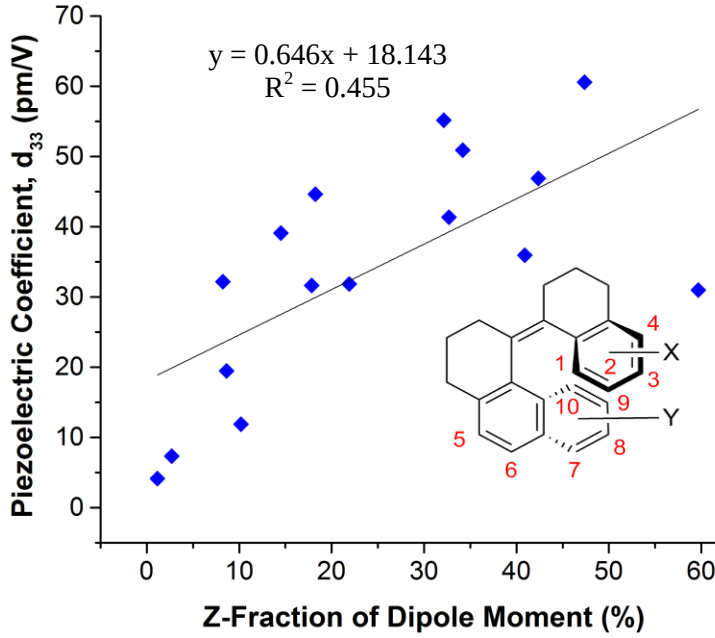

Figure 2.9 (A) Calculated piezoresponse (d_{33}) for 16 regiochemical isomers for amino- and nitro-substituted phenanthrene and z-fraction of the dipole moment of the 16 regiochemical isomers

under an applied field of ±1.285 V/nm. (B) The correlation graph shows a much higher correlation between the z-fraction of the dipole moment and the computed piezoresponse than the helicenes (**Figure 2.5**).

2.3.2.3 Functional groups

A variety of 3- and 8- substituted phenanthrenes were tested for their calculated piezoelectric coefficient, and although this regiochemical isomer does not show the highest calculated response above, the response of **4a9n** had a large variation over the ±1.29 V/nm range that it was tested, so for consistency purposes we decided 3- and 8- substituted phenanthrenes would be better experiments. Just as the [6]helicene above, in order to reduce confusion, the numbering will not match the IUPAC system, but instead will use the numbering in **Scheme 2.1.** Longer alkyl and alkoxy groups exhibit a larger percent deformation that we suspect is due to the free rotation capabilities of these chains. **Figure 2.10** shows the piezoelectric deformation of 42 combinations of functional groups tested. Stronger electron withdrawing groups (e.g., $-NO_2$ and -CN) and stronger electron donating groups ($-NH_2$ and -OR) will generally have larger deformation.[76]

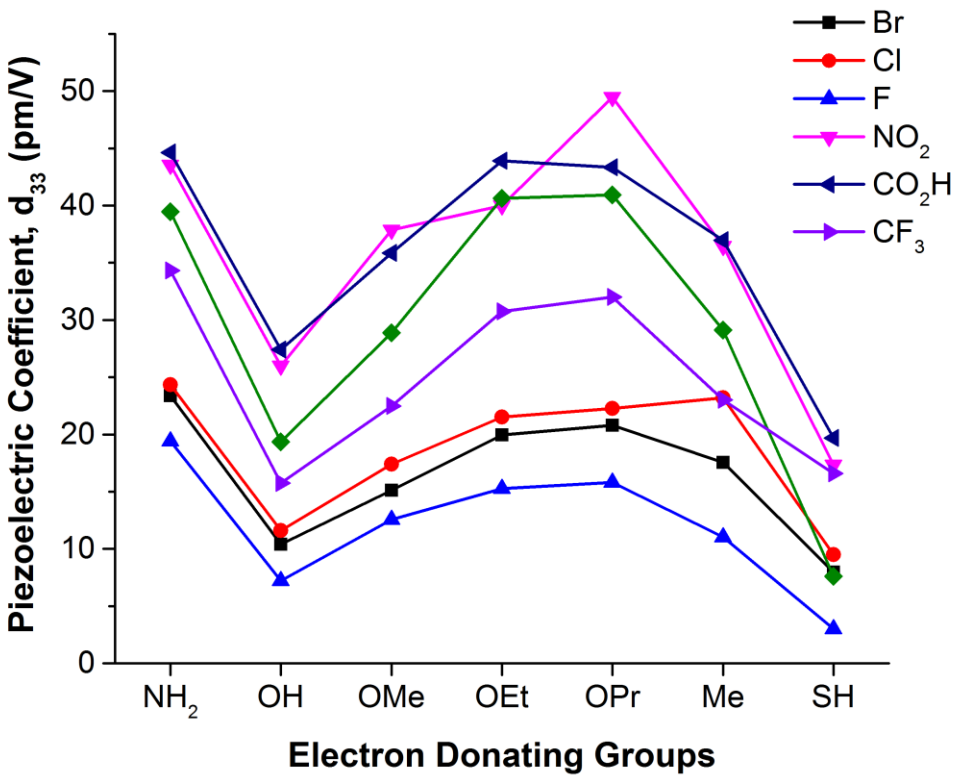

Figure 2.10 Variations of substituents on 3- and 8- positions and the resulting predicted piezoelectric deformation. Amine- and nitro- substituted phenanthrenes exhibit greater responses than the other functional groups. Figure is adapted from ref.[76]

2.3.2.4 Polarizability

Since the polarizability of these molecules contributes a large percentage to the potential energy of the "spring-like" system, then by increasing the polarizability a larger piezoelectric response should be predicted. Extending the conjugated system of the phenanthrenes by increasing the number of fused aromatic rings, as seen in **Scheme 2.2**, increases the polarizability of the molecule and in turn, the piezoelectric response. There is a very high correlation between the polarizability and the calculated piezoelectric coefficient, d_{33}, for the extended –arenes. With this relationship, we find that molecules that are highly polarizable are better targets than molecules with just a large z-component of the dipole moment based on the low correlation between z-component and the piezoelectric response as seen in **Figure 2.11**. There is a large correlation between both the extension of the system by increasing the number of fused aromatic rings and the ZZ polarizability with the piezo coefficient, d_{33}.

The reported responses might not be the highest for the systems of this size due to the regiochemistry of the functional groups. The position was chosen so the results were comparable between the extended –arenes.

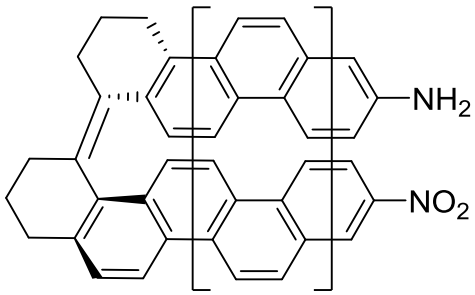

Scheme 2.2 Extended –arene with phenanthrene skeleton. This system is used to show the effect of the length of the system and polarizability on the piezoelectric response.

(A)

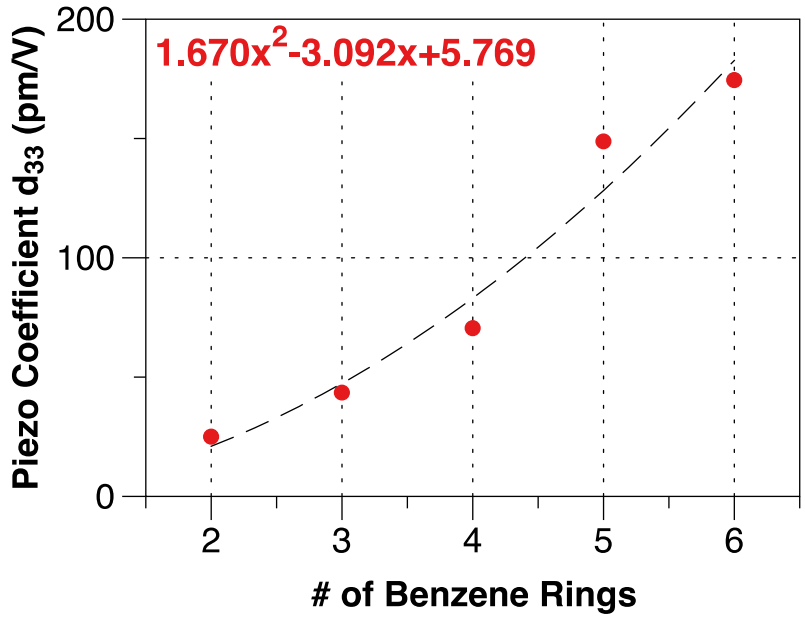
1.670x2-3.092x+5.769
Piezo Coefficient d33 (pm/V)
200
100
0
2
3
4
5
6
# of Benzene Rings

(B)

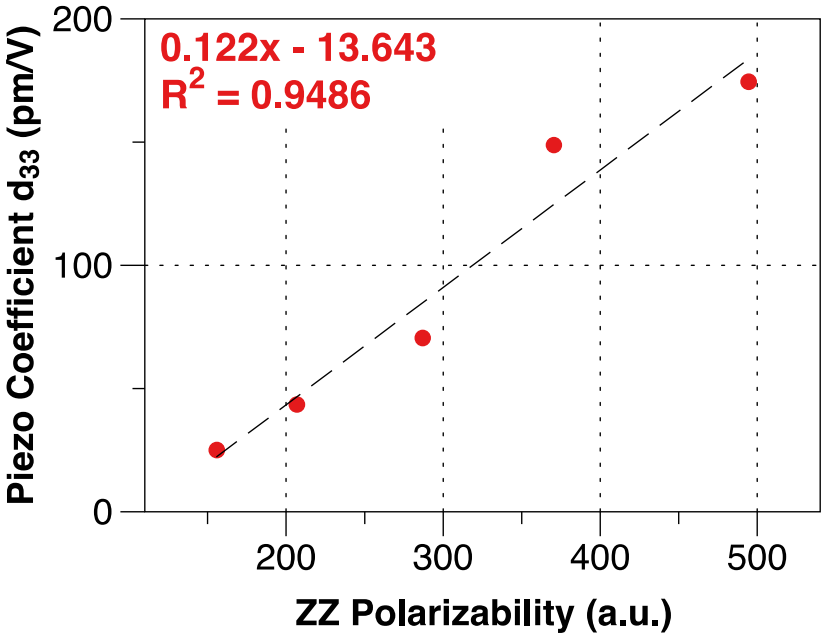
0.122x - 13.643
R2 = 0.9486
Piezo Coefficient d33 (pm/V)
200
100
0
200
300
400
500
ZZ Polarizability (a.u.)

Cont'd

(C)

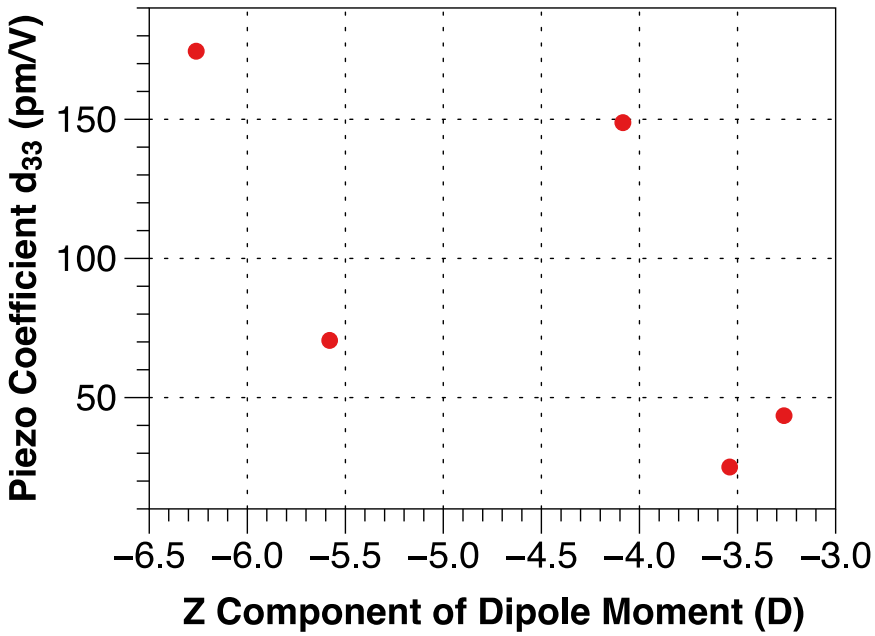

Figure 2.11 (A) The computed piezo coefficient of the molecule increases as the number of additional fused aromatic rings increases. This increase is correlated (B) to the increased polarizability (and thus induced dipole moment) and not the z-component of the permanent dipole moment (C).

2.3.3 Oligoaminoacids

We then discuss the piezoelectric effect of oligoaminoacids. Oligoaminoacids can adopt two main stable secondary structures, namely α-helix and β-sheet (**Figure 2.12**). The α-helical structure is maintained by an intramolecular hydrogen bond between the -NH- group of one amino acid and the C=O group of another amino acid four residues earlier. The dipole of each amino acid is lined up and accumulates to a very large dipole moment along the molecular helix. While in β-sheet the molecular backbone is stretched out with local dipoles cancelling each other out.

Hence α-helical oligoaminoacids are more likely to be piezoelectric than their β-sheet counterpart. For the simplicity of discussion oligoaminoacids with an α-helical secondary structure are studied in this thesis. Our calculations results on oligoaminoacids are largely verified by our experimental work presented in **Chapter 3**, where self-assembled monolayers of oligoaminoacids are tested.

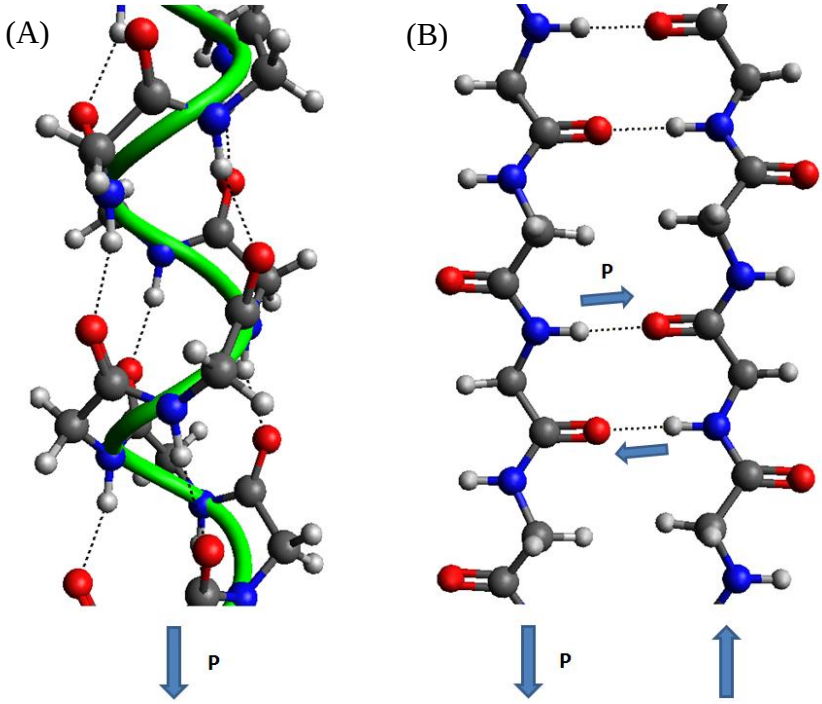

Figure 2.12 Structures of α-helix (A) and anti-parallel β-sheet (B). α-helical oligoaminoacids satisfy the model of a polar molecular spring.

2.3.3.1 Oligoaminoacids CA_6 and A_6C

We choose oligoaminoacids Cys-Ala-Ala-Ala-Ala-Ala-Ala (CA_6) and Ala-Ala-Ala-Ala-Ala-Ala-Cys (A_6C) as prototypes for several reasons. First is that alanine is more likely to form helices in a solvent-free environment.[82] This helps simplify both our calculation and experiment. Secondly, good comparisons can be drawn from CA_6 and A_6C as they are similar in structure but with opposite dipole moment from cysteine (Cys) end to alanine (Ala) end (**Figure 2.13**). They are supposed to stretch along the molecular helix but to opposite direction if the same electric field. Lastly, the sulfur atom on Cys will enable the formation of self-assembled monolayers (SAMs) of the oligoaminoacids on to gold surfaces due to the strong sulfur-gold interactions.

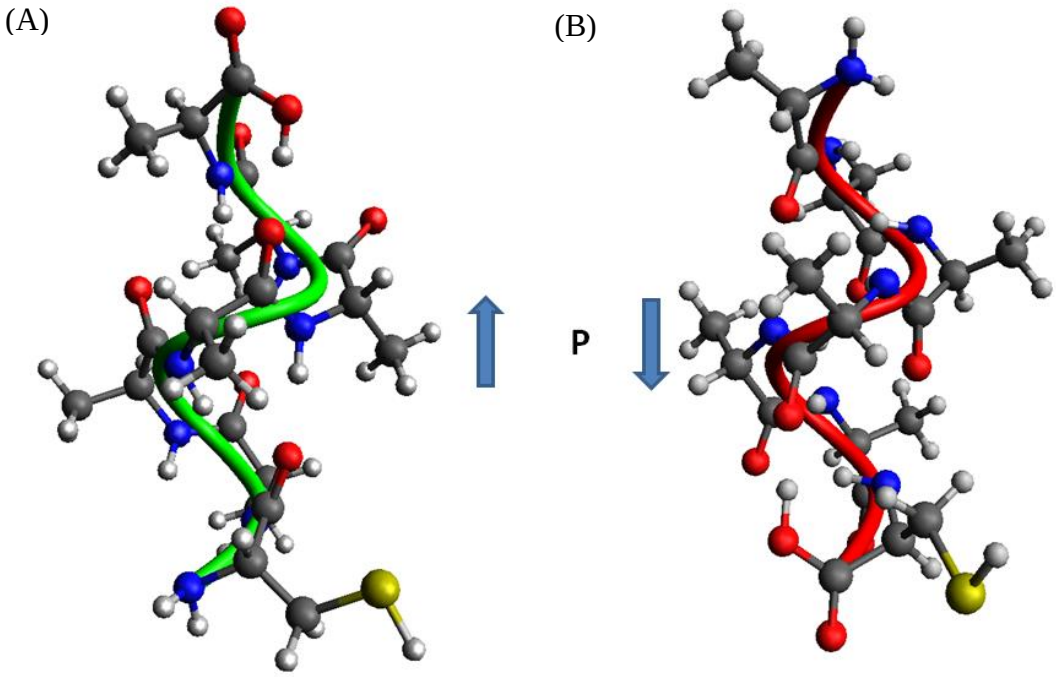

Figure 2.13 Molecular structure of α-helical CA_6 (A) and A_6C (B). Dipole moment is along the molecular helix from Cys end to Ala end in CA_6, and from Ala end to Cys end in A_6C, respectively.

The same field range (±1.29 V/nm) as with helicenes is applied to CA_6 and A_6C along the molecular α-helix. As shown in **Figure 2.14**, both molecules deform linearly when a smaller range of electric field is applied. The molecular length is defined as the distance between the two atoms/groups at the molecule ends further apart. For both molecules, the z-direction of the field is defined along the Cys end to the Ala end. It agrees to our predictions that the CA_6 helix contracts with increasing electric field while A_6C helix extends. Applying **Equation 2.1** on the linear region of both curves, a piezoelectric coefficient d_{33} of ~21 pm/V was calculated for CA_6 and of ~31 pm/V for A_6C over the field range of 0 - 1.29 V/nm, making oligoaminoacids comparable to ZnO nanowires (9.9~26.7 pm/V) and PVDF (-26 pm/V)[83] piezoelectric materials. If the more linear region is considered (± 0.26 pm/V), the calculated d_{33} will slightly decrease to ~14.7 pm/V for CA_6 and ~25.5 pm/V for A_6C.

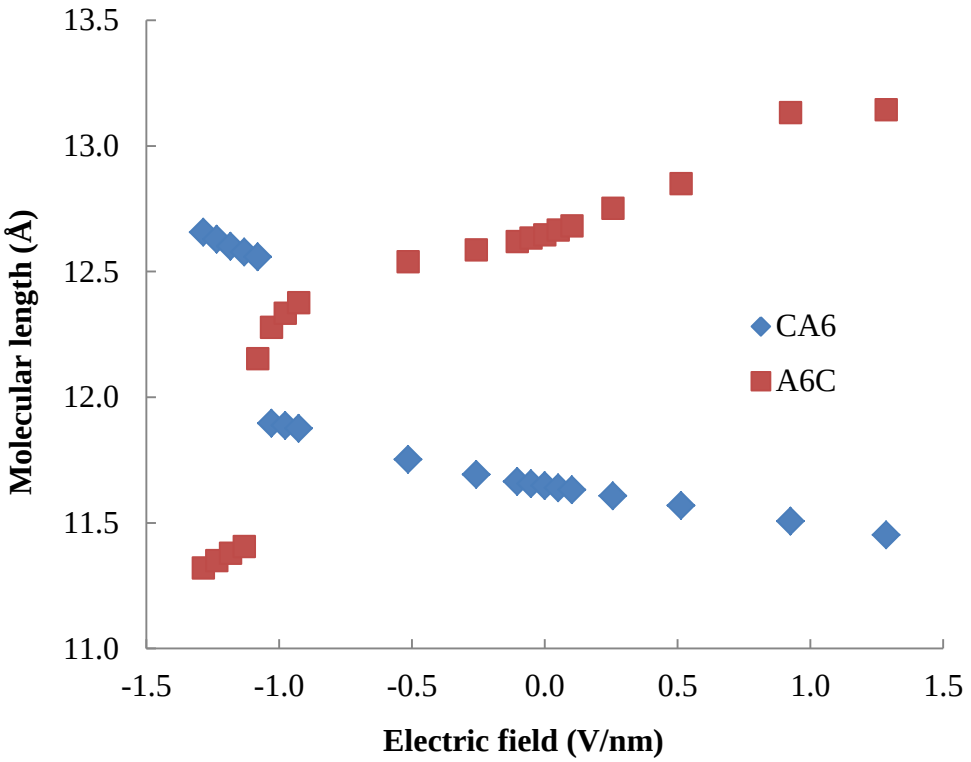

Figure 2.14 Calculated molecular length of CA_6 (from C/CH_3 to C/CH_2SH) and A_6C molecule length(N/NH_2 to C/COOH) under different applied external electric fields. For both molecules electric field is applied from Cys end to Ala end, resulting a reverse trend of distance change.

We assume that the stretch of the intramolecular hydrogen bond is responsible for the helix deformation (especially the linear region), similar to the piezoelectric origin of 2-methyl-4-nitroaniline (MNA) crystals as previously reported by our group.[28] Dramatic molecular length change was observed for both molecules when the field strength passes beyond a certain point. Such discontinuity of the molecular length change indicates a different path along which the molecule change shapes. As discussed below, the path of change for CA_6 is different from that for A_6C.

As shown in **Figure 2.15 A**, at 0 field strength the two hydrogen bonds indicated are four amino acid residues apart. When the field strength decreases beyond (about) -1.08 V/nm, the two hydrogen bonds are forced to dissociate and reform between three amino acid residues (**Figure 2.15 B**). CA_6 favors a 3_{10}-helical conformation in between field strength -1.29 V/nm and -1.08 V/nm. In a 3_{10}-helix each amino acid corresponds to a ~120˚ turn in the helix and the N-H group of an amino acid forms a hydrogen bond with the C=O group of another amino acid *three* residues earlier. The observation of electric field induced conformational change between α-helix and 3_{10}-helix has been reported observed via a scanning tunneling microscopy (STM) study on peptides SAMs.[84] While in between -1.03 V/nm and 1.29 V/nm an α-helix conformation is favored, where each amino acid corresponds to a ~90˚ turn in the helix and the N-H group of an amino acid forms a hydrogen bond with the C=O group of another amino acid *four* residues earlier.

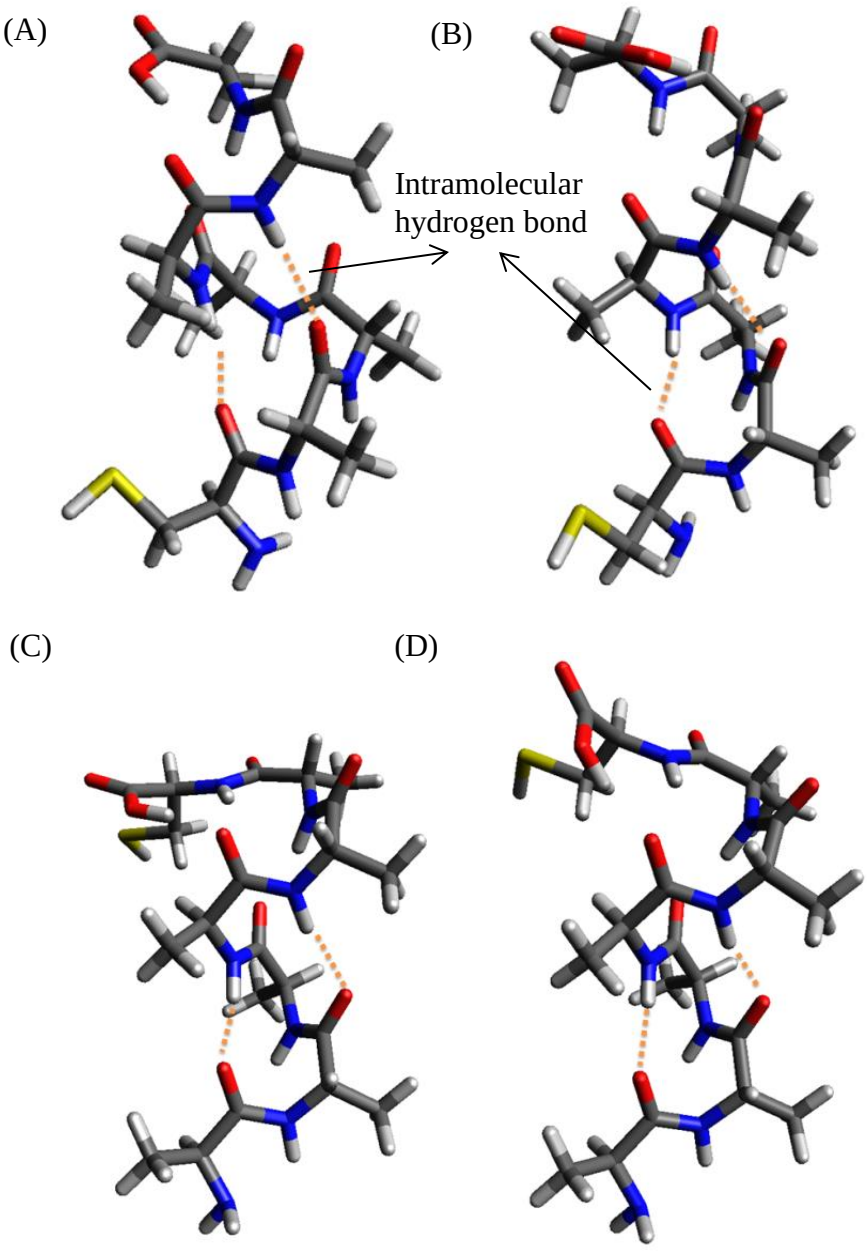

Figure 2.15 Structures of optimized CA_6 and A_6C under applied electric field. CA_6 adopts an α-helical conformation at 0 V/nm (A) and 3_{10}-helix below -1.08 V/nm (B). A_6C remains a 3_{10}-helical conformation within ± 1.29 V/nm with an end bending taking place at around -1.13 pmV (C and D).

In the case of A_6C, however, the jump in the molecular length change is caused by other reasons. Within the whole range of the field applied (± 1.29 pm/V), A_6C favors a 3_{10}-helix conformation (**Figure 2.15 D**) and is hence longer than CA_6 with the same number of amino acids. Instead of a transformation between α-helix and 3_{10}-helix, the cysteine end of A_6C bends towards the rest of the molecule beyond -1.13 V/nm (**Figure 2.15 C**). There might be two relatively stable conformations below and above -1.13 V/nm and switching between the two stable conformations leads to the discontinuity of the length change.

In real experiments, such discontinuity in molecular length change may not occur as 1) the effective field strength across the molecule helix may not exceed 1 V/nm and 2) the Cys-gold attachment and molecular packing (as in SAMs) may hinder the free bending of A_6C. We will show in **Chapter 3** that the deformation of CA_6 SAMs is linear in response to the applied electric field.

2.3.3.2 Control molecules

Since all molecules will change shape to some extend under applied electric field, we could distinguish our proposed piezoelectric oligoaminoacids from other rigid organic molecules with similar molecular lengths. The same DFT calculations are performed on several control molecules of dodecanethiol (DT), 11-mercaptoundecanethiol (MUA), three CA_6 random coils and linear CA_6 (**Figure 2.16**).

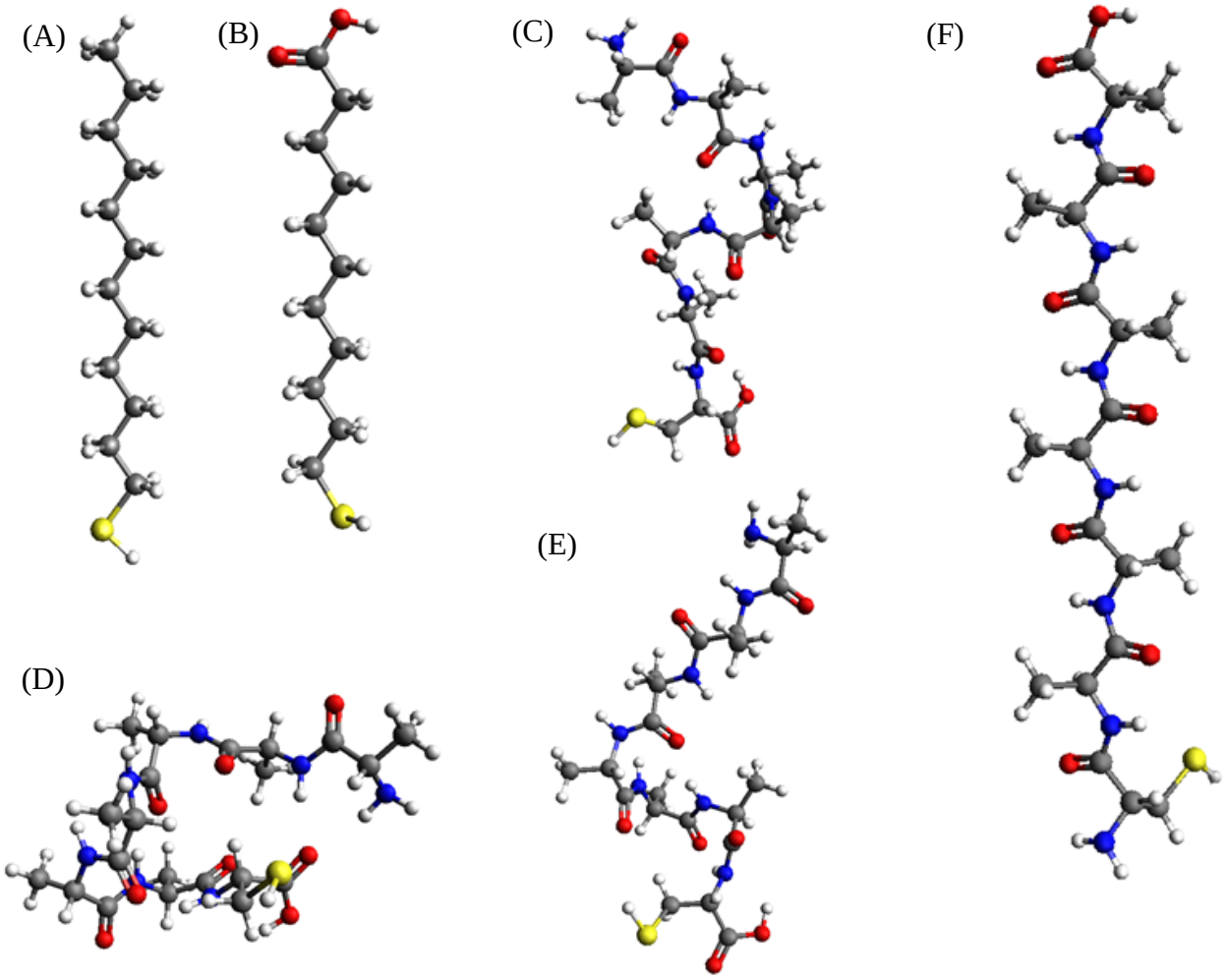

Figure 2.16 Molecular structure of (A) dodecanethiol (DT), (B) 11-mercaptoundecanethiol (MUA), (C-E) three CA_6 random coils, and (F) linear CA_6. These control molecules are either rigid with a very small piezoelectric coefficient d_{33} (~1 pm/V) (DT, MUA, and linear CA_6) or flexible to change length in a non-linear/random fashion.

The calculated deformation of molecules listed in **Figure 2.16** is shown in **Figure 2.17. Figure 2.17 A** is a redraw of the field induced length deformation curve of CA_6 (**Figure 2.14)** with the z-direction realigned to compare with other molecules in convenience. DT and MUA also change lengths in response to an applied electric field (**Figure 2.17 B**) but just to a minor extend with a very small d_{33} of 0.54 pm/V for DT and 1.55 pm/V for MUA. Such molecules will serve as good control molecules in the experimental study.

Three random coils of CA_6 from molecular dynamics (MD) (included in **Chapter 4**) trajectories are optimized under the same applied field range (**Figure 2.17 C**). The z-direction is arbitrarily assigned since a breathing mode is unclear to identify in random coils. The molecule length is defined as the distance between the two atoms furthest away from each other. Instead of a smooth linear trend, the molecule conformation distorts randomly. It seems obvious that random coils will change shape differently in response to a field applied in different directions. However, this might not be the case for α-helical CA_6. When the same field range is applied perpendicular to the molecular helix of CA_6, the molecule remains the α-helix conformation and stretches in response to the electric field (**Figure A8**). The shape change is minor with a calculated d_{31} of 3.0 pm/V over a small field range (-0.26 to 0 pm/V). A similar α-helix to 3_{10}-helix transformation is observed when large field (>1.18 pm/V) is applied. Such linear deformation under perpendicular field of CA_6 resembles those conventional piezoelectrics.

The electric field induced deformation of linear CA_6 is also negligible (1.01 pm/V, **Figure 2.17 D**) compared to helical CA_6. The helical structure with intramolecular hydrogen bonds may be key to the overall piezoelectric effect.

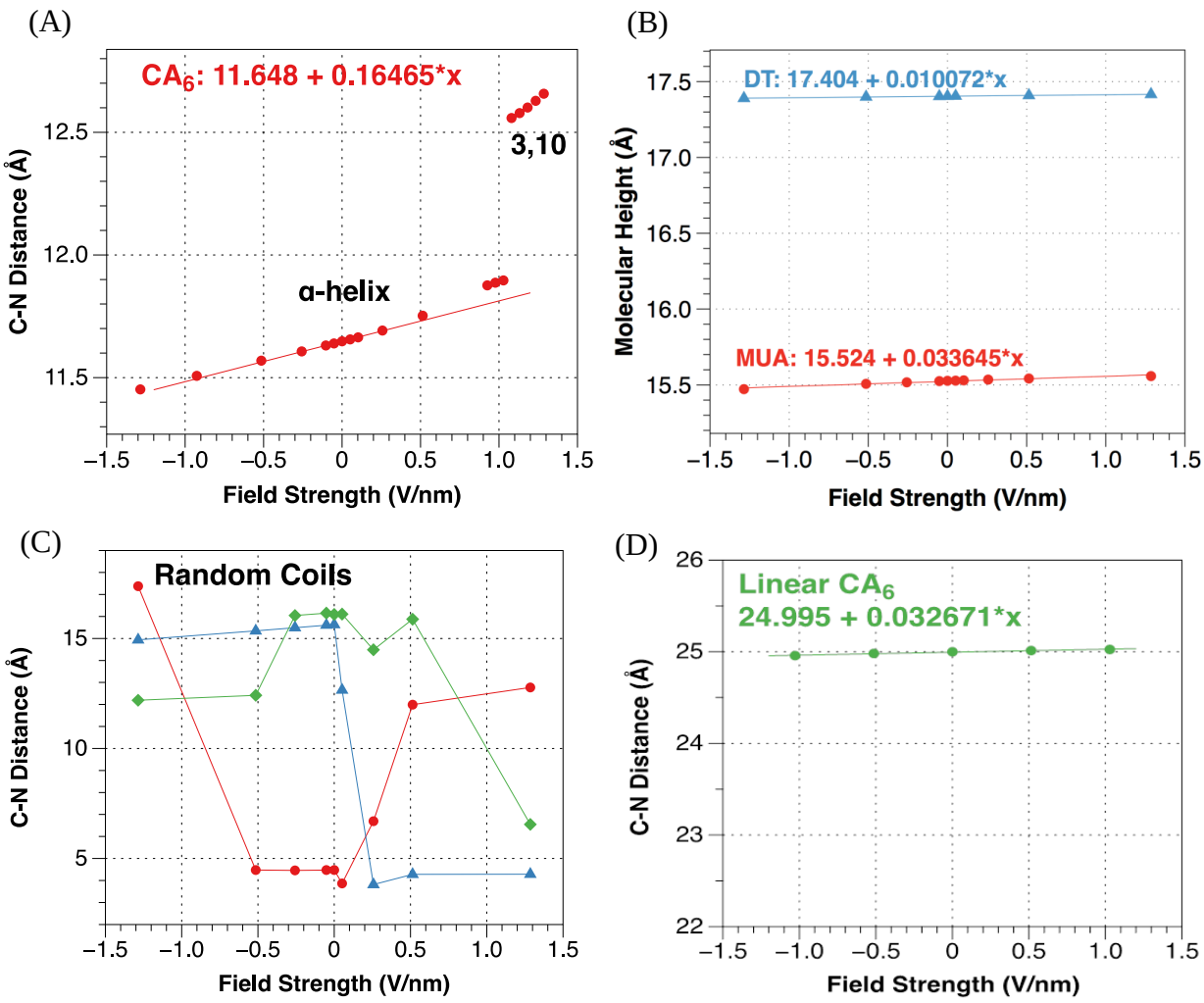

Figure 2.17 DFT geometry optimizations of molecules under study as a function of applied electric field. (A) α-helical CA_6 using the terminal C and N atoms, and showing linear response near zero field, and transition to a 3_{10}-helix at ~1.1 V/nm, (B) dodecanethiol (DT) and 11-mercaptoundecanoic acid (MUA), using the molecular height along the z-axis, (C) three CA_6 random coil conformations from the MD trajectories, illustrating nonlinear response as the oligomer kinks and unkinks, and (D) linear CA_6 using the terminal C and N atoms, showing little piezoresponse. For the convenience of comparison between different molecules, the direction of the applied field is realigned to each molecule to ensure a stretch over the positive field range.

2.3.3.3 The effect of helix length on calculated d_{33}

We have assumed that the overall piezoelectric effect of helical oligoaminoacids comes from the stretch of the intramolecular hydrogen bond along the molecular helix under applied electric field. Ratio of the number of intramolecular bonds to the number of amino acid residues (H-A ratio) would then affect the overall piezoelectric deformation under the same applied electric field, namely that longer chains would have a larger calculated d_{33}. As the molecular chain becomes longer, this d_{33} increase would eventually saturate since the H-A ratio comes closer to 100%. Furthermore, helical conformation is more likely to dominate in longer peptides.[85]

A series of oligoaminoacids CA_n with an increasing number n of alanine residues were constructed to test this hypothesis. Each molecule, from CA_7 to CA_{12}, was first optimized without an applied field for the lowest energy geometry. The d_{33} was calculated by averaging over a relatively small field range of ±0.26 V/pm. The geometry optimization both with and without an applied field favors 3_{10}-helix over α-helix for CA_n with $n > 7$. As shown in **Figure 2.18**, with the addition of each alanine, both calculated molecular length and dipole moment increase in a linear fashion. Each alanine adds ~2.0 Å and ~4.4 Debye to the helix. Some minor variations are observed for the length increase. As the 3_{10}-helix rotates 120˚ with each alanine added, the molecule length seems to change in a period of three alanine residues.

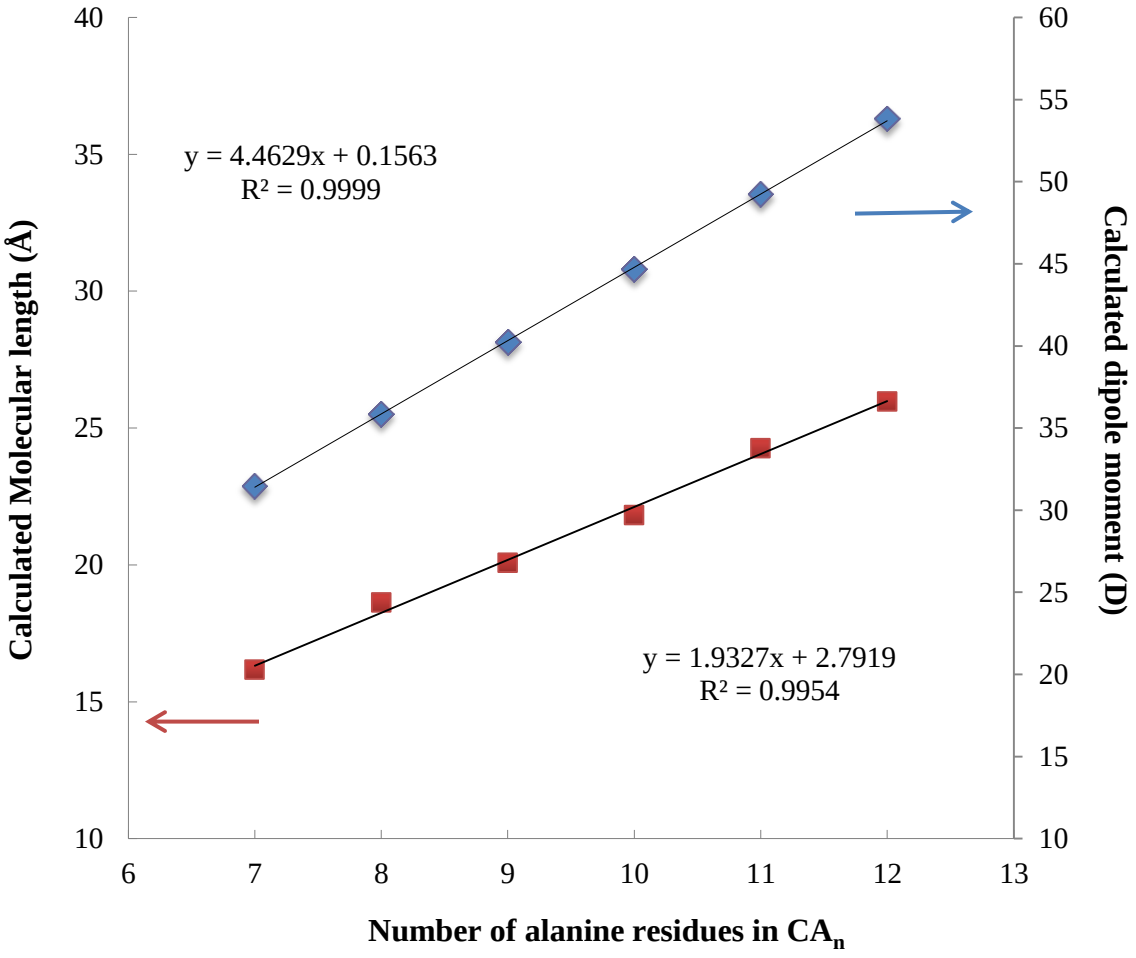

Figure 2.18 Correlation of the calculated molecular length (left) and dipole moment (right) to the number of alanine residues in CA_n.

Longer computational time is required for the optimization of longer chains. Some nonlinearity starts to show up starting from CA_7 (**Figure A9**). Instead of using two points as in **Equation 2.1**, the d_{33} for longer oligoaminoacids is an average over the whole range of the applied electric field (±0.26 V/nm). As shown in **Figure 2.19**, dramatically large d_{33} are calculated for longer oligoaminoacids, with up to 96.8 pm/V of CA_7 and 88.2 pm/V of CA_{10}. Similar to the molecular length change, the 3-alanine period is more distinctive in the trend of the d_{33} change.

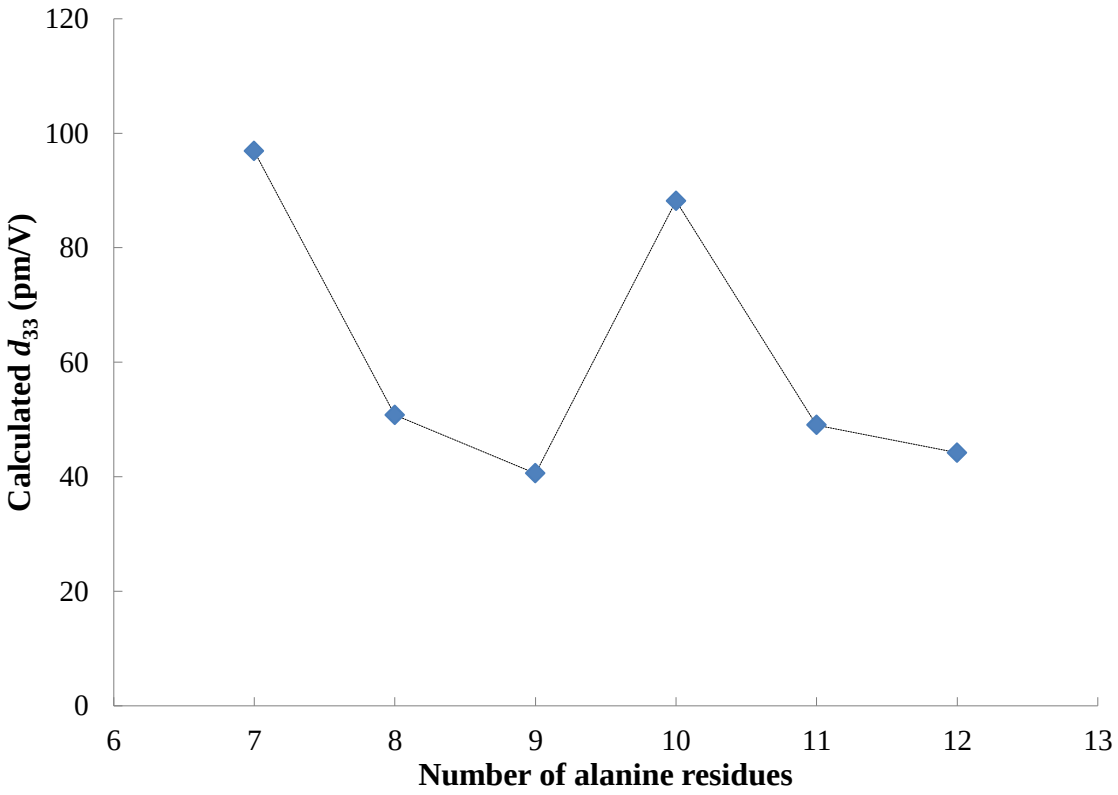

Figure 2.19 Calculated d_{33} versus the number of alanine residues from CA_7 to CA_{12}.

Although the dipole moment of each oligoaminoacids from CA_7 to CA_{12} points along the molecular helix, the linear increase of dipole moment through CA_7 to CA_{12} doesn't bring a linear increase of the calculated d_{33}. Instead, the relation between the calculated d_{33} and the calculated dipole moments is similar in shape to that between the calculated d_{33} and the number of alanine residues (**Figure 2.20**). The total dipole moment of a given oligoaminoacids is the sum of the dipole of each amino acid residue. Since each added dipole is in nature a tensor, the alignment of each dipole may be accounted for the periodic change of the calculated d_{33}. However, more studies in detail are needed to better explain this feature.

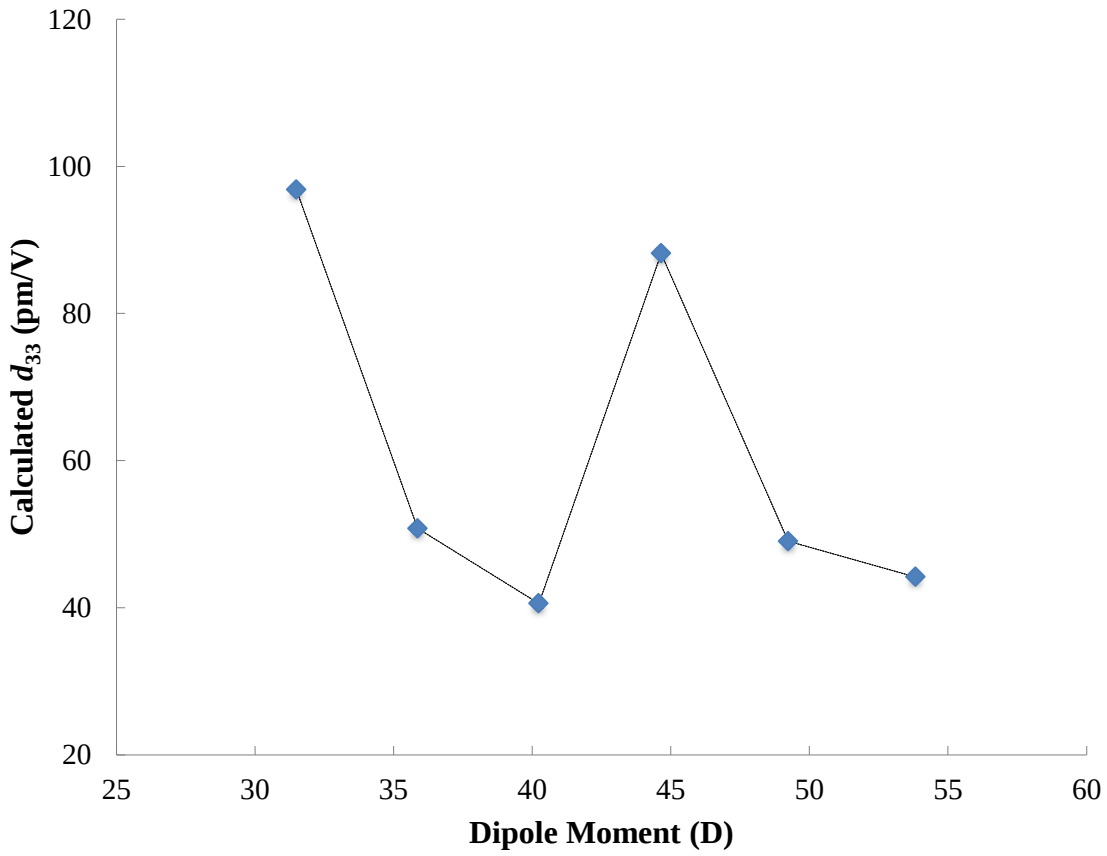

Figure 2.20 Calculated d_{33} versus Calculated dipole moment of CA_n.

2.4 SUMMARY

We have demonstrated that single molecules can respond via piezoelectric distortion to an applied electric field. Such changes are conformational in nature, as the coupling between the applied field and the molecular dipole moment drive an expansion or contraction of the molecular helix, along the breathing modes. The applied field changes the global minimum geometry, on top of any vibrational displacements about the equilibrium.

For helicenes and phenanthrenes, regioisomeric effects are found to be important, based on our study of 16 regioisomers of amino-nitro[6]helicene and phenanthrene. The regiochemical effect on the piezoelectric response is complicated, although we find a large predicted piezoelectric coefficient, d_{33}, for several regiochemical isomers and a variety of substituted [6]helicenes and phenanthrenes, most notably 4-amino-15-nitro[6]helicene with a piezoelectric coefficient of 48.8 pm/V and 49.5 pm/V for 3-nitro-8-propoxy phenanthrene, both comparable with inorganic materials, and far above piezoelectric response in other organics, such as PVDF. Piezoelectric responses, upwards of 100-272 pm/V, have been predicted for the extended helicenes and phenanthrenes, or "clamphenes." It should be mentioned that these responses are measured on single molecules and not crystals nor multi-layers like conventional piezoelectric materials. We suspect that due to enhancement of the local electric field, deriving from aligned molecular dipole moments, multilayer polar films may yield even greater response.[77]

Correlating dipole moment, polarizability, and steric interactions with the piezoelectric response will provide future design direction. Modification of the piezoelectric response is possible by changing the regiochemistry of these skeletons. In our study of substituted [6]helicene, a range of 47 pm/V (1.8 to 48.8 pm/V) is shown solely by modifying the positions of the substituents. The regiochemical effects are not completely clear, but some initial reasoning

behind the noticeable differences includes steric inhibitions, intramolecular hydrogen bonding for certain substituents, and alignment with the applied electrical field. Preliminary studies have shown that as the difference in Hammett-Taft constants increases, the piezoelectric response also increases. Other design rules for good targets that have shown promise include high polarizability, since the polarizability contributes ~41 % of the potential energy, and a low force constant to allow for larger deformations for lower input force.

For oligoaminoacids, the helical conformations (both α-helix and 3_{10}-helix) with intramolecular hydrogen bonds are key to the overall piezoelectric coefficient. Electric field induced conformation changes are either minor for linear oligoaminoacids CA_6 or without a clear pattern for random coils. The small deformations observed of more rigid molecules like DT and MUA distinguished the piezoelectric helical CA_6 and A_6C. Instead of the chain length, the number of the alanine residues in CA_n seems to play a larger role in determining the overall d_{33}. The number *n* In 3_{10}-helical CA_n series, the d_{33} is found to increase and decrease in a cycle of 3 additional alanine residues. A large d_{33} up to 96.8 pm/V is found for helical CA_7.

From what we have shown, it is possible that there is little "upper limit" to the piezoelectric response of molecules designed for conformational response. For example, in order to generate a piezoelectric response of 500 pm/V, on par with lead zirconium titanate (PZT), a molecule would need only a 50 % change in length upon an applied electric field of 1 V/nm (e.g. 4 Å to 6 Å). While such a target molecule has not yet been discovered, it is easy to imagine that such molecules can exist based on our computations of the extended systems, "clamphenes" and well-known redox-mediated conformational changes such as biological ion channels. Experimental verification of these results can be achieved by piezo-force atomic force microscopy, self-assembled thin-films, and other techniques.

3.0 EXPERIMENTAL DEMONSTRATION OF PIEZOELECTRIC EFFECT ON OLIGOAMINOACID SELF-ASSEMBLED MONOLAYERS

This work, written in collaboration with Jeffry D. Madura and Geoffrey R. Hutchison*, was ready for submission.

Dr. Jeffrey D. Madura performed the molecular dynamics (MD) simulation.

3.1 INTRODUCTION

This chapter details the experimental demonstration of single molecule piezoelectricity where piezoresponse force microscopy (PFM) and Fourier-transform infrared (FTIR) spectroscopy with grazing angle mode were employed. While the observation of conformational change at single molecule level may require high sensitive instruments with ultralow vacuum and low temperature settings; we approach this issue via self-assembled monolayers (SAMs) at ambient conditions. The piezoelectric single molecule oligoaminoacids (i.e. CA_6 and A_6C) proposed by our computational studies can form SAMs on smooth gold surface. The breathing mode of the molecular helix is then normal to the gold surface. Using the techniques of PFM and FTIR we are able to measure the collective electromechanical response out of thousands of molecules yet still directly indicating the behavior of a single molecule. The SAMs packing will also inhibit molecule from bending perpendicularly to the surface,[86] leaving molecule stretching more

preferable to be detected under applied electric field. We also used control molecules to minimize noise, tip-surface electrostatic effect, and other inherent instrument artifacts.

This chapter will begin with an introduction of the experiment methods employed and continue with sample preparation, experiment results and discussions.

3.2 EXPERIMENT METHODS

3.2.1 Piezoresponse force microscopy (PFM)

In the last two decades, Piezoresponse Force Microscopy (PFM) has been developed from a principle[87] based on Scanning Tunneling Microscopy (STM)[88] and Atomic Force Microscopy (AFM)[89] to a primary technique for imaging and nondestructive characterization of piezoelectric materials on the nanometer scale.[90-93] In recent years, this technique has included characterization of molecular and biological systems, which usually have lower piezoelectric response and complicated ambient environment.[93, 94]

PFM is a contact mode AFM technique with an alternative voltage U_{tip} applied to the tip while scanning.[89] Thickness change Δt of the piezoelectric samples caused by the changing voltage will lead to a vibration of the tip, which is detected and recorded by a laser diode signal system. The induced sample displacement under applied field is a demonstration of the samples' piezoelectric character. Relation between displacement and the applied voltage is then studied to further determine the piezoelectric response of the sample.

Figure 3.1 illustrates the working principle of PFM.

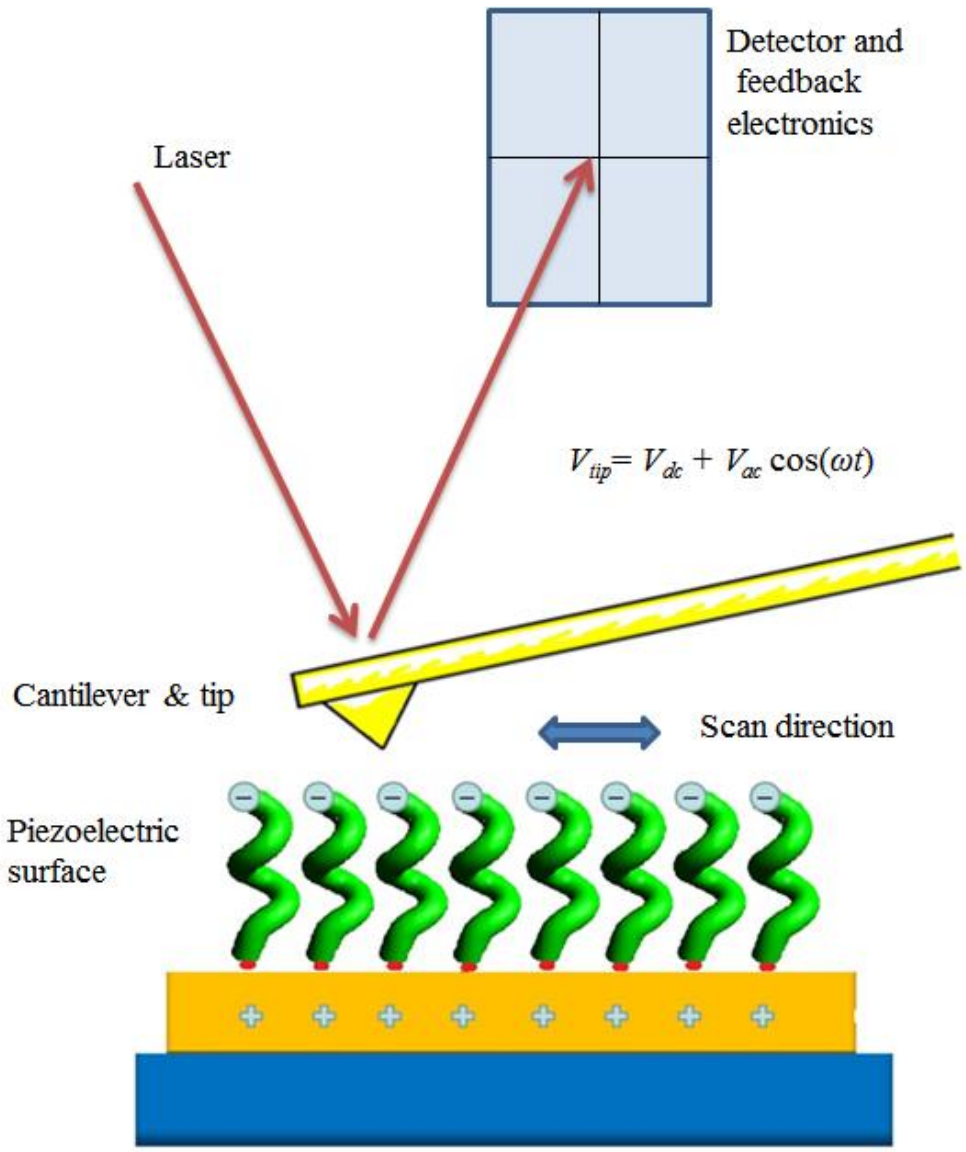

Figure 3.1 Illustration of the working principle of PFM. The tip voltage induced piezoelectric amplitude will be recorded by the laser detector and feedback electronics.

The overall deflection signal of the laser diode in PFM has three components, the displacement of the tip, the tip-sample interaction, and the displacement of the sample. The sample displacement is the true component of the piezo amplitude, while tip displacement and tip-sample interaction bring measurement artifacts. Limitations to obtaining quantitative PFM results include nonlocal effects from the tip,[95] complex background signal,[96] tip-surface electrostatic effects,[97] and potential drop from tip to surface due to weak indentation and high surface resistance.[97, 98] Some of the artifacts can be minimized by applying a larger force between the tip and sample surface, however, for soft materials in this study this method is not practical since large contact force could physically damage the soft SAMs. Although PFM has become a powerful tool in the study of piezoelectric materials and multiple calibration methods have been reported to increase performance in quantitative measurement,[99, 100] PFM has never been utilized as a method to determine the piezoelectric coefficient with high precision.[101]

According to our calculation in **Chapter 2**, the displacement of CA_6 single molecule can reach 1.2Å within the field range of ±1.29 V/nm, just above the best reported AFM normal resolution, which is slightly less than 1Å.[102, 103] Such a small displacement challenges good signal-to-noise ratio (SNR). Recently improved sensitivity and lower SNR are available by the introduction of a new test method called dual AC resonance tracking (DART).[104, 105]

In the DART mode, the tip is in contact with the surface and a sinusoidal bias is applied to the tip to excite the tip-surface resonance. During the scan, the excitation frequency will constantly change to trace the contact resonance peak via two lock-in feedback loops tracking and to level the amplitude over two frequencies above and below the initial contact resonance (**Figure 3.2**). SNR can be considerably improved since larger amplitude displacement will occur due to contact resonance. Quantitative correction is available by using the instrument default

software from the recorded amplitude, frequency, and phase data.[105] Crosstalk between the topography and the piezoresponse signal could also be minimized under contact resonance to avoid inconclusive or conflicting results.[104, 106]

Because of the intrinsic thin and soft nature of our samples (SAMs of oligoaminoacids), only small tip-sample force was applied to compromise between good tip-sample contact and large tip induced sample damage. This will lower the effective potential applied across the SAMs.

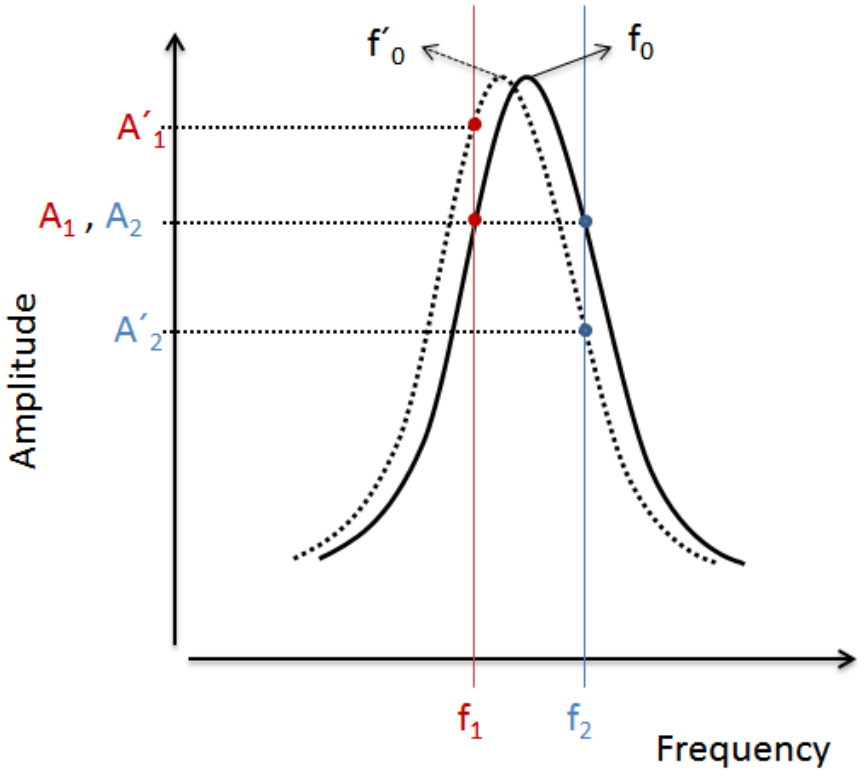

Figure 3.2 Illustration of the working principle of DART (redrew from Ref. [105]). The difference of the two amplitude $A_1' - A_2'$ indicates the direction of the resonance frequency shift from f_0 to f_0'. With the amplitude change as an error signal in a feedback loop, the resonance frequency can be tracked by changing the excitation frequencies f_1 and f_2 where $A_1' - A_2'$ is maintained close to zero.

3.2.2 Grazing angle Fourier-transform infrared spectroscopy (FTIR)

Fourier-transform infrared (FTIR) spectroscopy has been used to characterize protein secondary structure for over two decades.[107, 108] Distinctive IR absorption bands are observed to be indicative for protein secondary structures. The so-called amide I peak sits near 1650 cm^{-1}, consisted mainly of the C=O stretching vibration with minor contributions from the out-of-phase C-N stretching, the C-C-N deformation and the N-H in plane bend. Amide II band is mainly the out-of-phase combination of the N-H in plane bend and the C-N stretching vibration. The peak is centered on 1550 cm^{-1}. These Amide bands (especially Amide I) are almost signature to protein secondary structures. **Table 3.1** lists the assignment of amide I band and range to secondary structures.

Table 3.1 Band assignment and range of amide I of protein secondary structures.[109]

	Band position in $^1H_2O/cm^{-1}$	
Secondary structure	Average	Extremes
***α*-helix**	1654	1648–1657
***β*-sheet**	1633	1623–1641
***β*-sheet**	1684	1674–1695
Turns	1672	1662–1686
Disordered	1654	1642–1657

Hydrogen bonding is considered as a major role in determining the position of the amide I.[110] The amide I peak increases in wave number as the strength of the hydrogen bond decreases in the following order of secondary structures: intermolecular extended chains (1610-1628 cm^{-1}), intramolecular antiparallel β-sheets (1630–1640 cm^{-1}), α-helices (1648-1658 cm^{-1}), 3_{10}-helices (1660–1666 cm^{-1}) and non-hydrogen-bonded amide groups in DMSO (1660–1665 cm^{-1}).

Transition dipole coupling is another determining factor for the amide I position.[111] The coupling of the oscillating dipoles of neighboring amide groups relatively depends on the orientation of and the distance between the dipoles. The coupling intensity will change as the peptide chain extends or stretches.

Although the vibration spectrum can provide lots of structural information such as chemical structure, redox state, bond length and bond strength, bond angle and conformation, hydrogen bonding, etc.,[112] its indication of the α-helical stretch can only be qualitative.[113] The employment of FTIR in this thesis is expected to provide only qualitative evidence of the conformational change of our oligoaminoacids under applied electric field.

Our sample is an oligoaminoacids SAM on nontransparent flat gold substrates, so we use FTIR spectroscopy with the grazing angle incidence reflection mode. The model used in this thesis (Bruker GAO) has very high sensitivity due to their novel use of a folding mirror and a dual pass design.[114] The working principle and the experiment setup are illustrated in **Figure 3.3**.

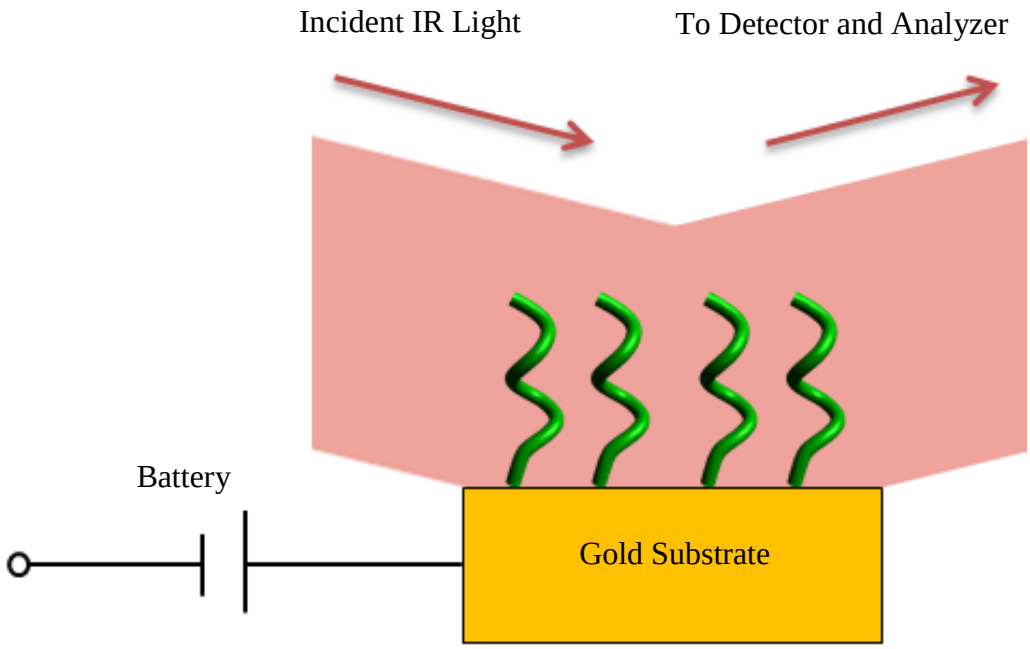

Figure 3.3 Illustration of the working principle of grazing angle FTIR and the experiment setup.

3.3 SAMPLE PREPARATION AND CHARACTERIZATION

Materials Used

CA_6, A_6C, dodecanethiol (DT), and 11-mercaptoundecanethiol (MUA) were purchased from Sigma-Aldrich, Inc. Amidated CA_6 was purchased from AnaSpec, Inc. All molecules were used as received without further purification. The epoxy resin (Epo-Tek 377) was obtained from Epoxy Technology. Silicone elastomer kit (Sylgard 184) for making polydimethylsiloxane (PDMS) was purchased from Dow Corning Corp. High grade mica substrate for template-stripped gold (TS-gold) was purchased from Ted Pella, Inc. Optical diffraction grating with 1μm grooves was obtained from Rainbow Symphony, Inc. The 2 μm "dot" patterned master (patterned photoresist on silica wafer) for CA_6/MUA and MUA/CA_6-am mixed SAMs was obtained from the Center for Nanotechnology (CNT) Nanotechnology User Facility (NTUF) of the University of Washington.

Fabrication of Template-Stripped Gold (TS-Gold)

TS-gold[115] was prepared by depositing 200 nm of gold onto a freshly-cleaved mica via E-beam evaporation (Multi-source Electron Beam Evaporation System , Thermionics Laboratory VE180) with a base pressure of 2×10^{-6} torr. The first 50 nm thick layer was deposited at a rate of 0.1 Å/s, while the remaining 150 nm was deposited at 0.5 Å/s. The epoxy adhesive starting materials were mixed according to the manufacturer's instruction. The gold side of the mica slice was then glued to a glass slide using the epoxy mixture and was put into oven at 150°C for 1 hour to anneal. The mica-gold-epoxy-glass sandwich was then immersed in tetrahydrofuran (THF) for several minutes to loosen the contact between mica and gold. The mica chips were

then peeled off using a pair of tweezers and dried with a stream of nitrogen. Every time a fresh gold substrate was made right before the next step fabrication of patterned SAMs.

Fabrication of Polydimethylsiloxane (PDMS) Stamp

The two components of the silicone elastomer were mixed and vigorously stirred for 10 minutes and vacuumed for 30 min to drive the micro air bubbles away. Once it became clear, the mixture was poured onto the mold (diffraction grating and "dot" masters) and was placed in an oven at 60°C for 1.5 hours. The cured polymer stamp was peeled off and cut into small pieces of approximately 2 mm by 4 mm before use. Stamps were soaked and rinsed with hexanes multiple times to remove possible low molecular weight oligomers. The cleaned PDMS stamps were then kept in vacuum overnight for drying and were stored in the lab glove box.

Patterning SAMs

The patterning was achieved by using the method of microcontact printing (μ-CP).[116] A solution of 10 μM of dodecanethiol (DT) in ethanol, 10 μM of 11-mercaptoundecanoic acid (MUA), < 1 mM of CA_6, <1 mM of amidated-CA_6 (CA_6-am), and < 1 mM of A_6C in 1:1 (v:v) water / acetonitrile were prepared as the "ink" source. Due to the small amount of the oligoaminoacids used, an accurate concentration was not determined. The stamp was dipped into 1 mL of the ink source for 5 minutes, dried in air and then stamped on the already prepared gold surface for 5 minutes before peeling off. Patterned DT, CA_6, and A_6C SAMs were made following the same procedure, respectively. The ink loading process for making patterned MUA SAMs is different. MUA was loaded to the stamp using drop cast methods. A newly prepared stamp was used for every stamping.

CA_6 and MUA mixed films were obtained by immersing the as-made patterned CA_6 films into 1 mM of MUA in ethanol for 10 minutes, followed by washing with ethanol and drying in

air. MUA and CA_6-am mixed films were obtained by immersing the as-made patterned MUA films into CA_6-am solution for 10 minutes, followed by washing with water/acetonitrile and ethanol and drying in air.

FTIR Sample Preparation

Gold-coated quartz crystal electrodes (CH Instruments, Inc.) were used for the preparation of CA_6 SAMs. The electrode was soaked in piranha solution (mixture of concentrated sulfuric acid to hydrogen peroxide with 3:1 ratio) for 2 hours. The gold electrode was then immersed in CA_6 solution for 48 hours to insure complete formation of compact SAMs. The SAM sample was washed with a solution of 1:1 water/acetonitrile and ethanol, respectively, for multiple times to remove physically attached CA_6 residues and was then dried in air. A gold electrode treated with piranha solution was used as background.

Piezoresponse Force Microscopy (PFM) Characterization

PFM measurement was performed with Asylum Research MFD-3D SPM. Both dual-AC resonance tracking (DART) mode and single frequency mode were used for quality results. Ti/Pt coated silicon tip (AC240TM, Asylum Research) with a first mode resonance frequency of 70 kHz and a normal stiffness of 2 N/m were used. For each sample characterized under DART mode, the contact resonance was around 280 kHz. 1-3 V tip bias was applied with respect to certain cases. Topography, piezoresponse amplitude, and phase images were all recorded. All recorded amplitude data was corrected q-correction from the tip-sample resonance amplification using the instrument default analyzing software. Multiple samples were fabricated and measured for consistency.

Note that the amplification correction (q-correction) was not available by default for single frequency mode. Piezo amplitude measured with this mode is only qualitative. The instrument inverse optical lever sensitivity (InvOLS)[117] was calibrated against a clean glass slide for every tip used.

FTIR Characterization

Fourier-Transform Infrared Microscope (FTIR) (Bruker VERTEX-70LS FTIR and Hyperion 2000) was used with the grazing angle mode. For a typical measurement, 0.41 to 1 cm^{-1} resolution was chosen for a scan of 5000 times within the range from 1000 cm^{-1} to 4000 cm^{-1}. The experiment was carried out in ambient conditions. The raw data was corrected from the effect of CO_2 and air humidity using the instrument default OPUS software.

A voltage bias was applied to the CA_6 SAMs by connecting the gold substrate to one electrode of an alkaline battery (± 9.6 V) or two batteries in series connection (+19.2 V) during the entire time of all 5000 scans.

3.4 RESULTS AND DISCUSSIONS

As mention earlier in this Chapter, instrument artifacts (e.g. electrostatic effect) will inherently contribute to the piezo amplitude. Only inclusive results of the piezo amplitude would be obtained from a sample with complete coverage of SAMs. SAMs with incomplete coverage (i.e. patterned SAMs) will provide a comparison between the piezo active SAMs and the piezo inert gold substrate.

Patterned SAMs can be fabricated via microcontact printing (μCP) method, which was first demonstrated in 1993 by Whitesides group in fabricating patterned SAMs of alkylthiols.[118] In a typical working process, alkylthiols was loaded from a solution "ink-source" to a patterned polydimethylsiloxane (PDMS) stamp. The inked PDMS piece was then stamped onto a smooth gold substrate where alkylthiols self-assembles into a compact molecular monolayer through the strong interaction between gold and sulfur atoms (**Figure 3.4**). Patterned SAMs with two components can be achieved by immersing one as-made patterned SAMs into a solution containing a different alkylthiol.[119] Microcontact printing has become a convenient and low-cost for making a variety of patterned thin films including also patterned SAMs of peptides and proteins.[120, 121]

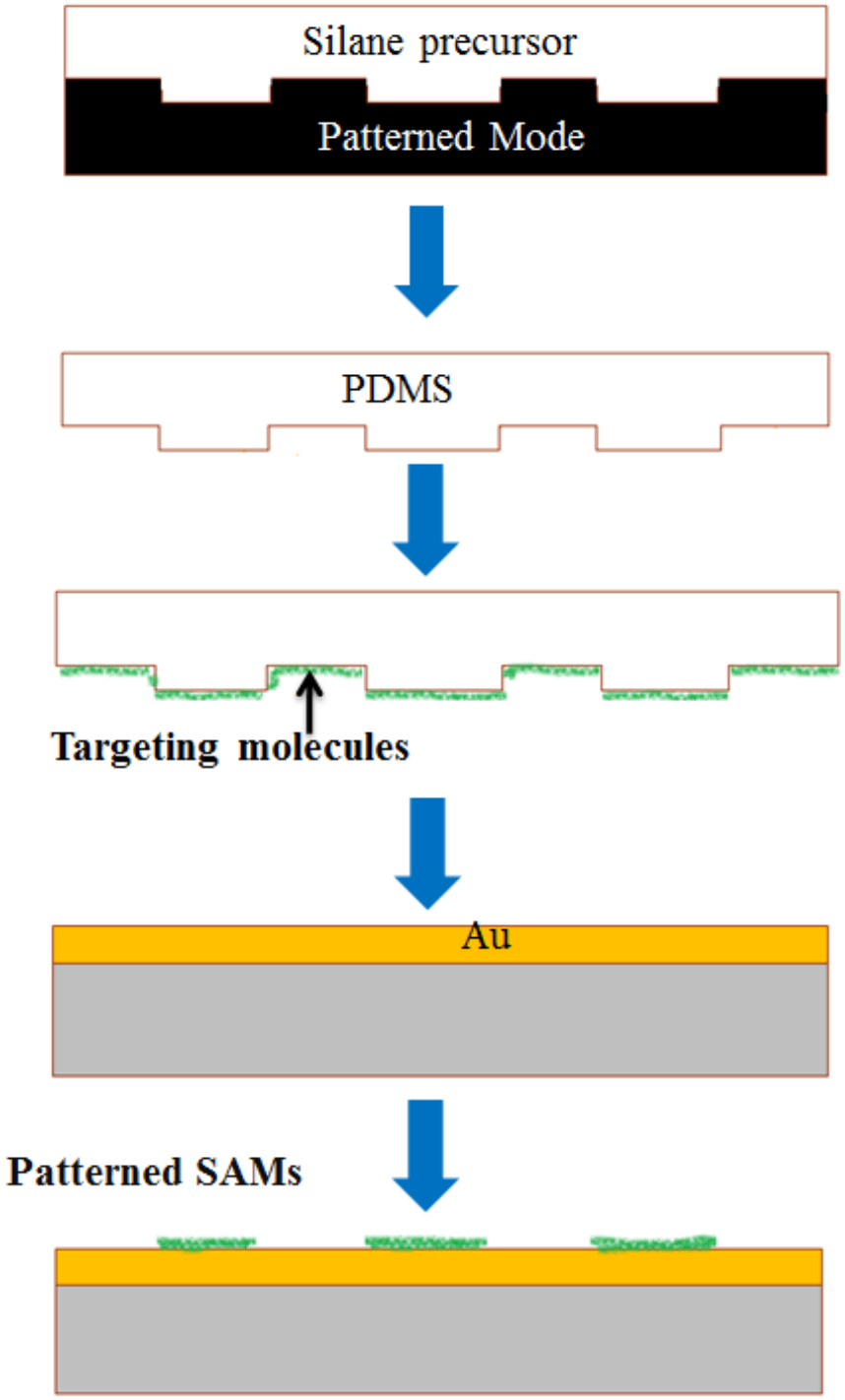

Figure 3.4 Procedure of typical microcontact printing (μCP) method.

3.4.1 PFM measurements

3.4.1.1 Topography and piezo amplitude of CA_6

Figure 3.5 A shows the topography of CA_6 SAMs in a stripe pattern. Formation of a monolayer is indicated by the match of the measured film thickness (~1.5 nm) to the DFT calculated molecular length (1.50 nm) of α-helical CA_6. The fact is notable that measurements of an exact film thickness require further information, such as modulus and Poisson's ratio of the film, and other tip parameters, since the topography data is essentially an interpretation of the tip-surface interaction.

When a bias of 3 volts was applied to the tip, the piezo amplitude contrast was clearly seen between region of the patterned SAMs and the bare gold (**Figure 3.5 B**). Piezo amplitude up to 6 pm was observed from the section data (**Figure 3.5 C**), giving a piezoelectric coefficient d_{33} of ~2 pm/V compared to 14.7 pm/V in theory. This difference can be explained at least in three aspects.

Firstly, since the DFT calculation involves a field applied parallel to the molecular helix in vacuum and assumes perfect electromechanical coupling, the computed piezoresponse of helical CA_6 should represent an ideal upper bound of the experimentally observed deformation for a single molecule. In the experiment, however, the PFM amplitude is averaged across an ensemble of $\sim 10^4$ molecules based on the effective tip radius and convoluted with nonlocal and electrostatic response, not just the piezoelectric deformation of the monolayers.

Secondly, the population of helical CA_6 is not likely to reach 100%. Both 3_{10}-helical and linear conformation is highly possible for shorter peptides,[85] as indicated by the molecular dynamics (MD) simulation as well (discussed later in this chapter). Linear conformation has a much weaker piezoelectric response with a calculated d_{33} of 1.01 pm/V.

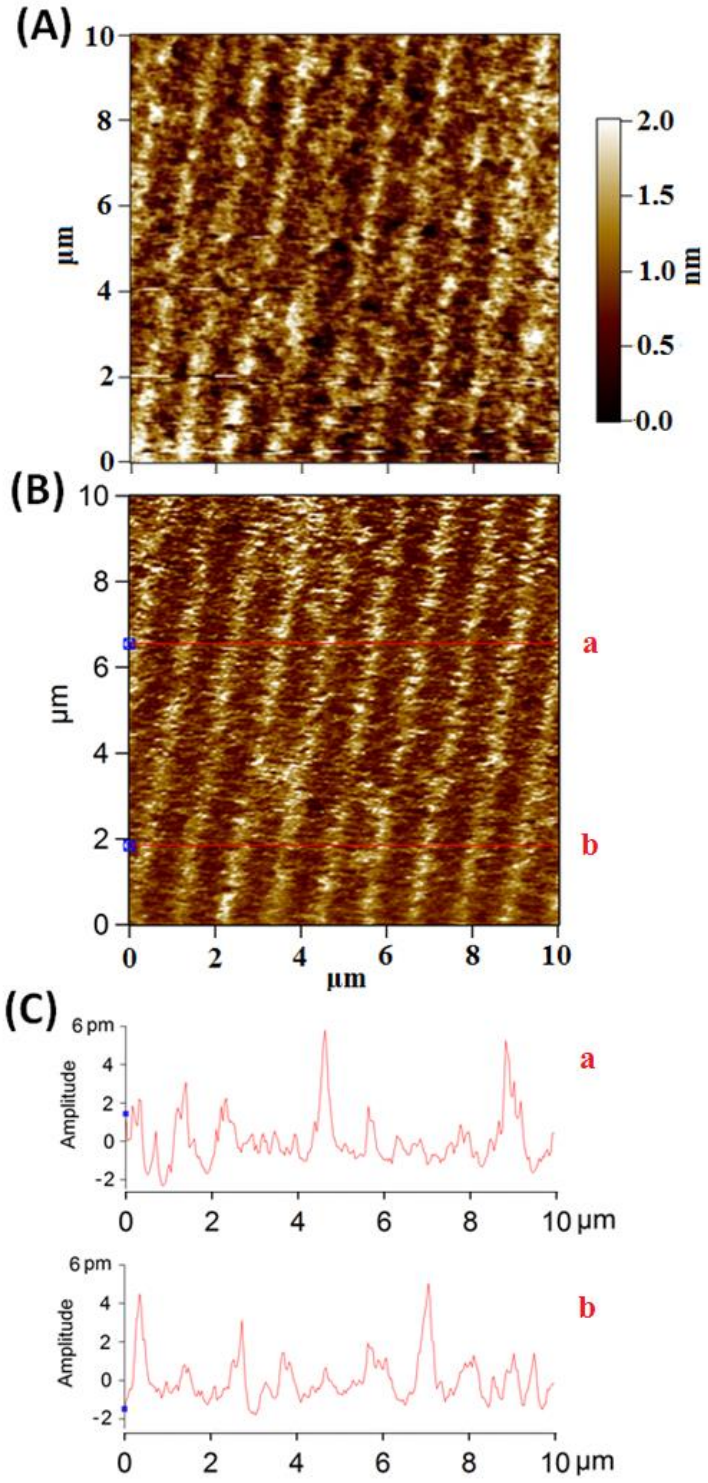

Figure 3.5 Topography (A), DART mode piezo amplitude (B) of patterned CA_6 SAMs. Section data of piezo amplitude on two randomly chosen lines are listed in image (C). The peak piezo amplitude is around 6 pm, giving a d_{33} of ~2 pm/V under 3V tip bias.

Thirdly, in ambient condition a water layer will inevitably form between the tip and the SAMs surface and lead to a potential drop from the tip to the SAMs surface.[97] The effective potential difference across the SAMs thickness may be much smaller than 3V, and the measured d_{33} is hence smaller than the actual value. Possible free CA_6 residues unattached to the gold surface would contaminate the Ti/Pt coated tip and further decrease the effective potential applied across the SAMs thickness.

Taking above factors into account, the experimental results are still in good agreement with our computational findings.

In order to be piezoelectric, the induced deformation has to be linear in response to the applied external electric field. Amplitude seen from applied bias with a single value may indicate a bistable switch behavior as well.[84] To address this issue, we compiled histograms of the PFM amplitudes as a function of electric field in DART mode (**Figure 3.6**). The low-response (left) edge (**Figure 3.6 B**) of the histogram serves as a baseline for the gold surface, and the high-response (right) edge of the histogram indicates the molecular extension. Both line scans and histograms indicate a large number of molecules exhibit large responses. For quantitative analysis, we used the full width at half-maximum (FWHM) as a measure of the PFM amplitude (**Figure 3.6 C**). The results averaged across multiple regions on multiple films measured with multiple tips indicate a linear FWHM change in response to applied electric field (**Figure A10**).

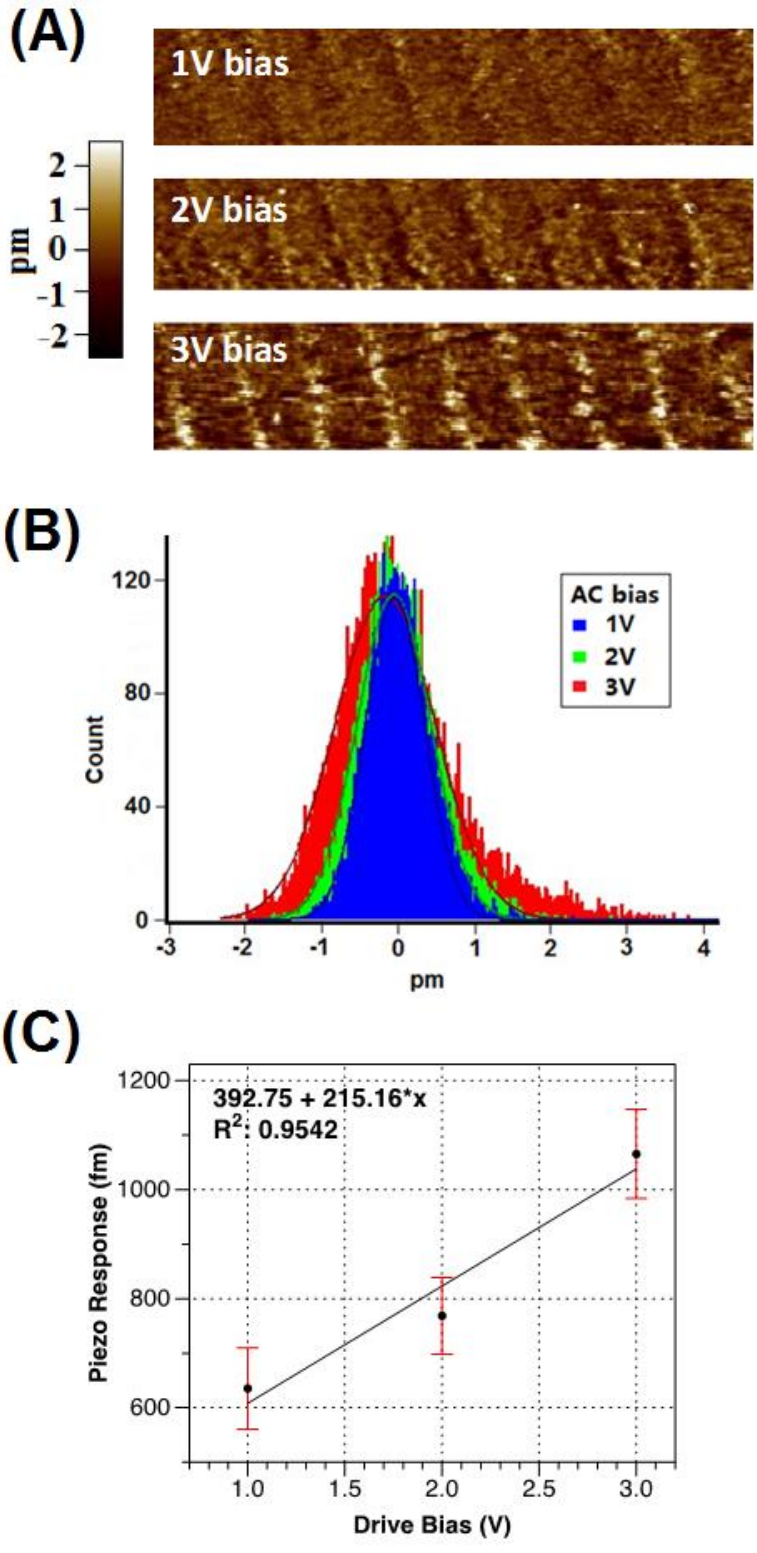

Figure 3.6 Piezo amplitude of CA_6 SAMs as a function of increasing applied bias voltage. (A)

DART PFM amplitude of CA_6 SAMs on bare gold, showing clearly increasing amplitude with increasing bias, (B) example histograms of DART PFM amplitudes as a function of increasing bias voltage, and (C) linear correlation between FWHM of histograms (as a measure of "average" response) and applied tip bias voltage.

3.4.1.2 Control experiments of A_6C, DT, MUA, and amidated CA_6

As mentioned earlier in this chapter, DART PFM is believed to be an improved technique for low response and non-uniform piezoelectric materials, and a method with lower signal-to-noise ratio and fewer resonance artifacts. However the inherent limitations (e.g. nonlocal effects, complex background signal, and electrostatic effects) still make it problematic to determine piezoelectric response of soft materials with a small piezoelectric coefficient both quantitatively and qualitatively.

To overcome these artificial amplitude contributions, we introduced built-in controls to examine the absolute piezoresponse. Patterned single monolayers of another oligopeptide (AAAAAAC, A_6C) and dodecanethiol (DT) were deposited by the same method onto individual gold substrates (**Figure 3.7 C** and **E**) to form single monolayers and was again judged by the agreement between AFM topography and computed molecular size.[122] Significant piezo response is found via DART PFM for both CA_6 and A_6C stripes, and substantially less amplitude is observed from the DT monolayers (**Figure 3.7 B**, **D**, **F**, and **Figure A11**). Thus, we hypothesize that the relatively large PFM amplitude from the CA_6 and A_6C monolayers derives primarily from intrinsic molecular conformational changes caused by the applied electric field. Some of the observed difference in PFM amplitude between CA_6 and A_6C monolayers may derive from the terminal (top) end group effect, -COOH for CA_6 and -NH_2 for A_6C, respectively.

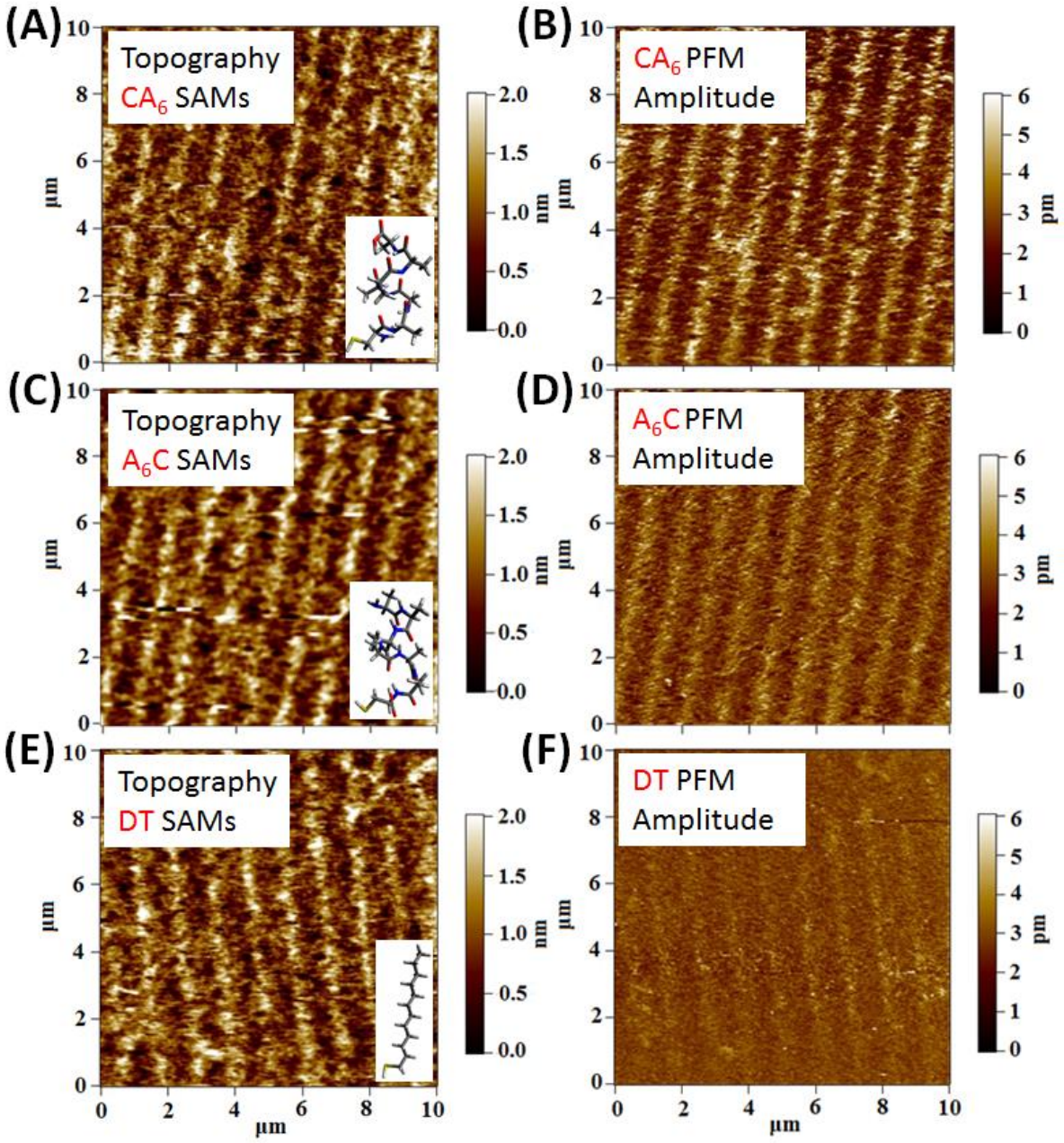

Figure 3.7 AFM topography and DART PFM amplitude of patterned molecular monolayers. AFM topography of (A) oligopeptide CA_6, (C) oligopeptide A_6C, and (E) dodecanethiol (DT), DART-PFM amplitude of (B) CA_6, (D) A_6C , and (F) DT with an applied bias of 3V.

Since the PFM characterization has been performed in ambient conditions, a water meniscus will form at the surface-tip interface. At neutral pH, the C-terminus of CA_6 will partially yield an anionic carboxylate-terminated surface atop the oligopeptide monolayer (*vide infra*), while the alkyl-terminated DT remains neutral. Similarly, CA_6 shows greater PFM response than the amine-terminated A_6C. Such electrostatic response would not only be different between the bare gold surface and the carboxylate-terminated CA_6 monolayers, but may explain the larger response of CA_6 when compared to the nonpolar, alkyl-terminated DT monolayers. To control for this effect, we prepared films using CA_6 peptide monolayer "dot" patterns (**Figure 3.8 A**), followed by backfilling the remaining exposed gold surface with 11-mercaptoundecanoic acid (MUA), since both molecules have a carboxylic acid group at the surface end (**Figure 3.8 B**). The isoelectric point (pI) of CA_6 is estimated to be 5.5, close to the pKa ~4.8 of MUA in solution.[123] The similarity between these two ends is also demonstrated by surface potential measurement via Kelvin probe force microscopy (KPFM), which gives a much smaller surface potential difference <20 mV between MUA and CA_6 compared to >70 mV between CA_6 and gold (**Figure A12**).

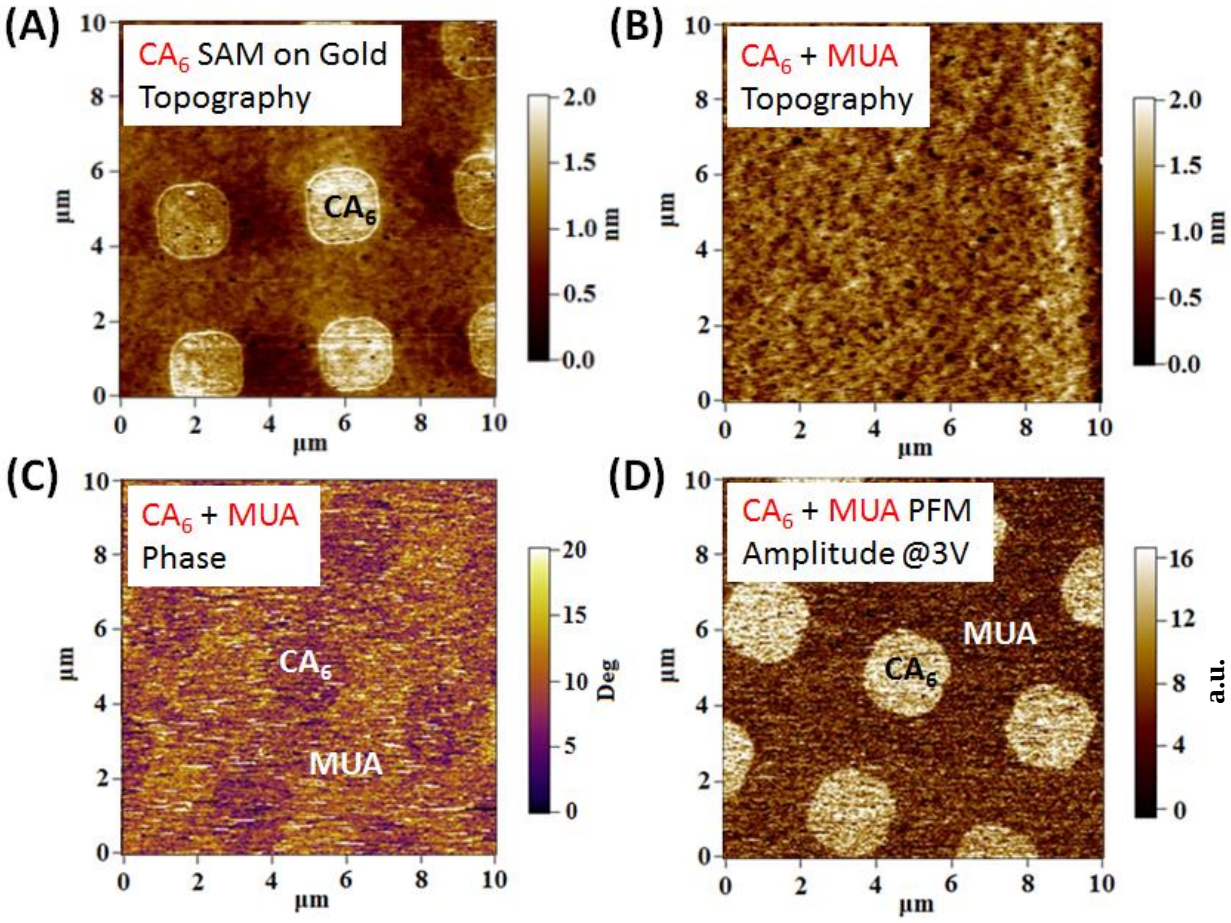

Figure 3.8 AFM topography, single-frequency PFM phase and amplitude of patterned and mixed monolayers. (A) AFM topography of oligopeptide CA_6 SAM on bare gold, (B) AFM topography of the same film after depositing a solution of 11-mercaptoundecanoic acid (MUA) to fill all exposed gold regions, (C) single-frequency PFM phase data of mixed CA_6/MUA film, indicating slight differences in phase between CA_6 "dots" and MUA background, and (D) single-frequency PFM amplitude of a mixed CA_6/MUA film with an applied bias of 3V.

Both CA_6 and MUA have similar computed heights 1.50 nm and 1.88 nm, respectively, so the AFM topology of the mixed film (**Figure 3.8 B**) appears essentially featureless; although the phase channel (**Figure 3.8 C**) shows slight variation between regions of the two molecular monolayers. While both CA_6 and MUA have comparable heights and terminal carboxylic acid groups, the computed piezo-driven conformational change in MUA (*vide infra*) is dramatically smaller than CA_6. As seen experimentally in **Figure 3.8 D**, the CA_6 islands exhibit markedly greater PFM amplitude at 3V bias than MUA. These mixed CA_6/MUA films are highly stable, and we have observed pattern retention and strong PFM response over 42 days in ambient conditions (**Figure A13**). While the single-frequency PFM mode used to image the mixed CA_6/MUA films cannot yield reliable *quantitative* measurements of the piezoresponse of the two materials, this technique clearly indicates that the PFM deformation observed in CA_6 patterns derives largely from molecular conformational changes and not solely due to end-group effects.

To further eliminate the electrostatic effect artifacts from the piezoelectric response, we compared MUA with amidated CA_6 (CA_6-am). The -COOH group at the C-terminus of CA_6 is converted to the $-CONH_2$ of CA_6-am (**Scheme 3.1**). The surface end of CA_6-am SAMs should remain neutral in the same conditions.

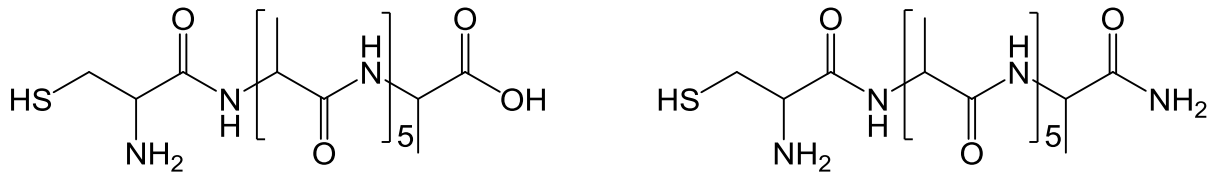

Scheme 3.1 Structure of CA_6 (left) and amidated CA_6 (right) with chiral center neglected. While CA_6 may provide a negatively charged end group $-COO^{\ominus}$ in ambient water layer, the C-terminus of amidated CA_6 will remain neutral.

A MUA/CA_6-am mixed film was fabricated similarly to the CA_6/MUA mixed film by first making a patterned MUA SAMs (**Figure 3.9 A**) followed by a backfilling with CA_6-am molecules. Again, the AFM topography of MUA/CA_6-am mixed film (**Figure 3.9 B**) is featureless while the phase image (**Figure 3.9 C**) shows a distinctive variation. The C-terminus amidation will not change much to the molecular structure or height. But the surface end will become charge neutral compared to a possible negatively charged end of CA_6.

If the electro static effect is the main contribution to the measured piezo amplitude, it is then well expected that the measured piezo amplitude of the CA_6-am region would not be significantly larger, if not smaller, than the piezo amplitude of the MUA region. On the contrary as shown in **Figure 3.9 D**, the CA_6-am region exhibits significantly larger PFM amplitude than MUA. Such result is even stronger evidence than the comparison between MUA and CA_6 that the electrostatic effect between the end group and the tip is should have played only a minor role in determining the PFM amplitude. We then reach the conclusion that the PFM amplitude observed for CA_6, A_6C, and CA_6-am SAMs is primarily resulted from the tip bias induced molecular deformation and those oligoaminoacids are piezoelectric in nature.

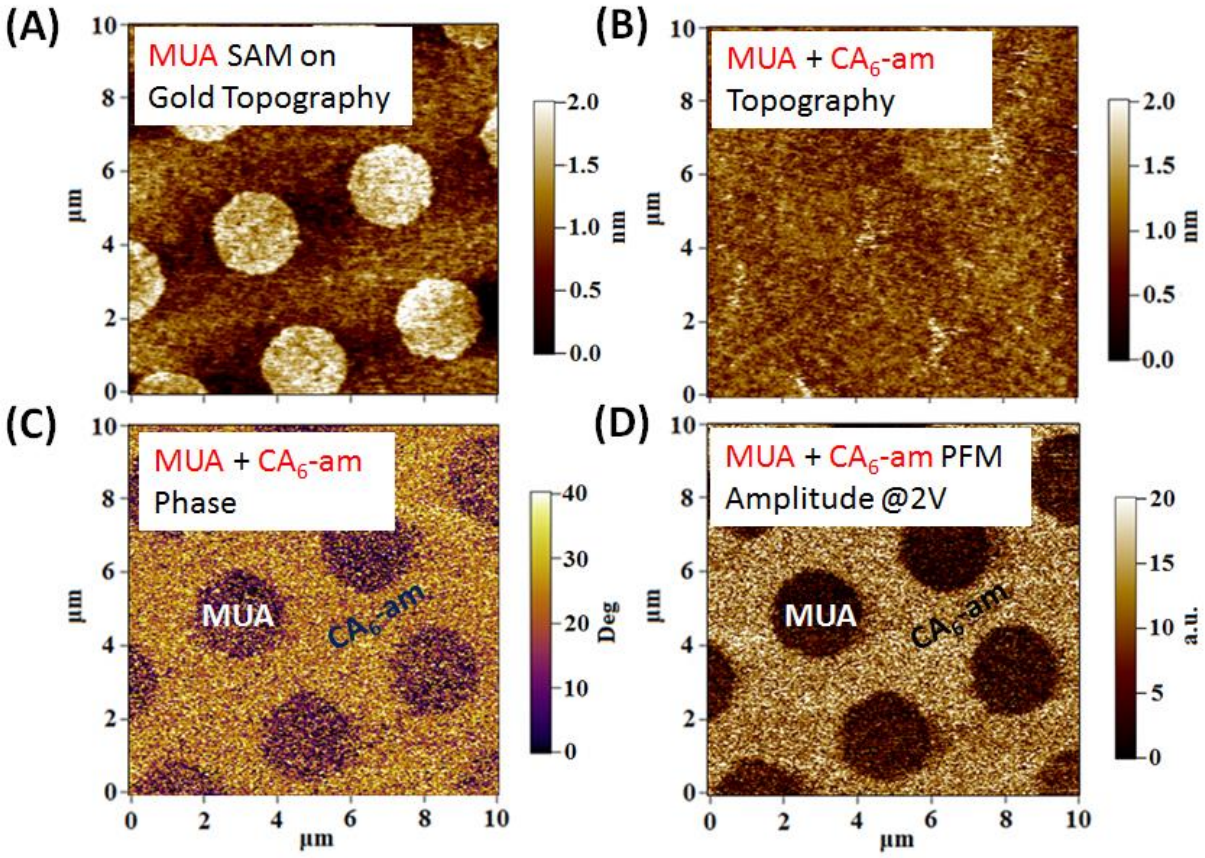

Figure 3.9 AFM topography, single-frequency PFM phase and amplitude of patterned and mixed monolayers. (A) AFM topography MUA SAMs on bare gold, (B) AFM topography of the same film after depositing a solution of CA6-am to fill all exposed gold regions, (C) single-frequency PFM phase data of mixed MUA/CA_6-am film, indicating distinct differences in phase between MUA "dots" and CA_6-am background, and (D) single-frequency PFM amplitude of a mixed MUA/CA_6-am film with an applied bias of 2V.

3.4.2 FTIR results

Grazing-angle Fourier-transform infrared spectroscopy (GA-FTIR) was used to examine the conformational change of oligopeptide CA_6 under different applied electric fields. Clear peak shift of Amide I (**Figure 3.10 A**) and Amide II (**Figure 3.10 B**) is observed when the gold substrate of CA_6 SAMs was charged with different potentials using an external battery. Since Amide I and II bands are signature to the secondary structure of proteins, the shift of the peak evidently indicates the secondary structure change of the surface attached CA_6 molecules. However, the amplitude and frequency shift of the peak is only indicative of a possible conformational change of the CA_6 under different applied potentials, and no quantitative conclusions can be deducted.

The broad peak widths indicate a highly diverse ensemble, which makes exact assignment of the vibrational peaks difficult. So we are unable to determine whether the molecule contracts or extends when a higher potential is applied. However, these results are still consistent with previous studies that peptide conformation could be changed by the change of surface charge density.[124]

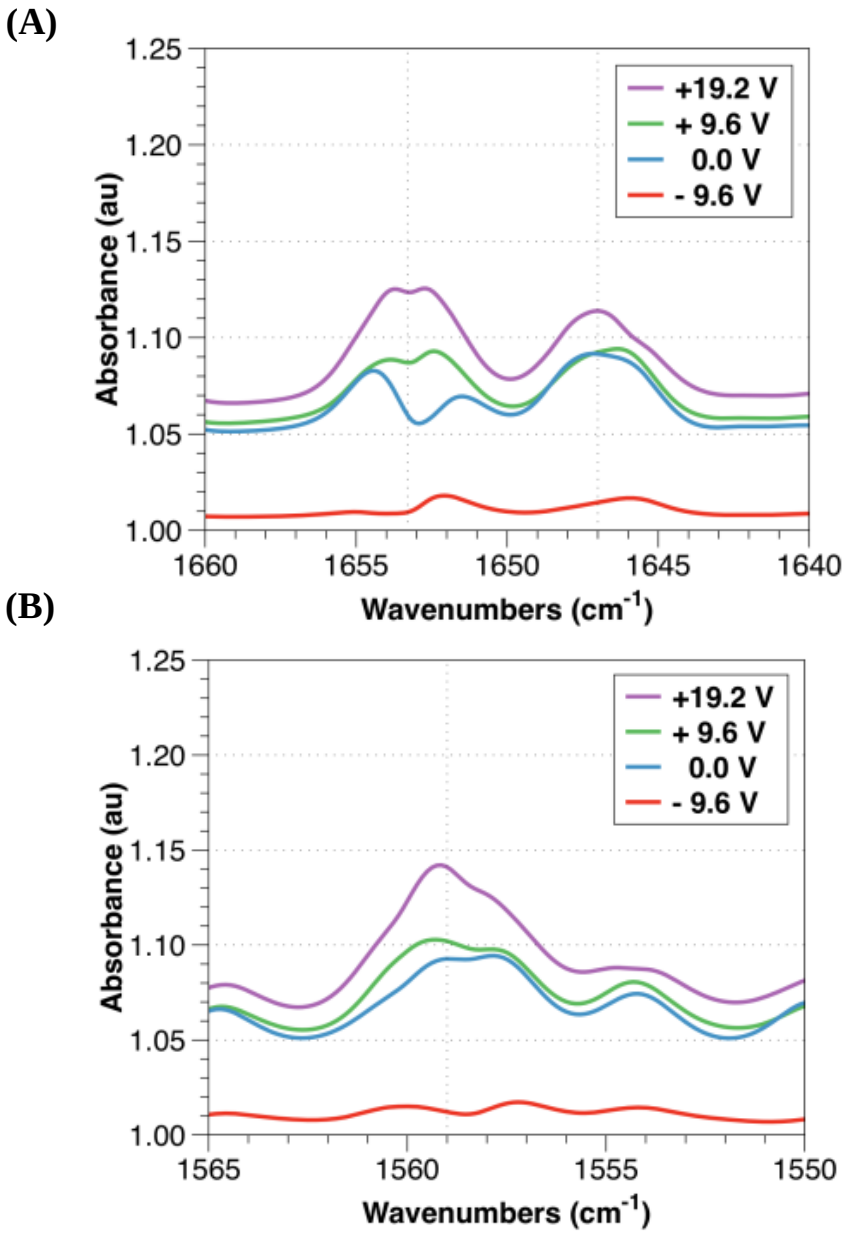

Figure 3.10 FTIR absorption of CA_6 SAMs on gold with an applied surface potential. Peak frequencies shift and intensities change under different surface potentials. Intensity of the two peaks, Amide I (A) and Amide II (B), increases as the applied voltage increases from -9.6V to +19.2V. Peak shape and peak position also changes in respond to the voltage change. The peak shift and intensity change indicate a structural change of the oligoaminoacids CA_6.

3.4.3 Molecular dynamics (MD) analysis

3.4.3.1 Computational methods

The molecular dynamics simulations consisted of a 7x7 array of 49 peptides, with sequences CAAAAAA (CA_6) or AAAAAAC (A_6C), arranged on a plane that represented a hexagonal gold surface[125] with Au…Au spacing of 2.88 Å. Each peptide started as an ideal α-helix and the sulfur atom of each cysteine in the peptide was held fixed. The initial coordinates of the peptides were generated using MOE.[126] For all MD runs, the Amber 99 force field parameters, as implemented in MOE, was used.[127]

Molecular Dynamics Protocols: The molecular dynamics simulations were performed using NAMD 2.8.[128] All simulations were done *in vacuo* using a 2 fs time step. Electrostatic and van der Waals interactions were switched off over the range of 2.5 Å starting at 10 Å. A pairlist for these interactions was calculated using a 13.5 Å distance. A temperature of 300 K was used in the simulations and was kept constant using a Langevin thermostat. The simulations were run for a total of 1 ns. For the non-zero field simulation, a 2.306 kcal/mol•Å•e (= 1.0 V/nm) or 10.0 kcal/mol•Å•e (=4.35 V/nm) external electric field was applied in the +z direction, normal to the planar surface defined by the sulfur atoms of the peptides.

The trajectory file from each of the different simulations was analyzed using VMD.[129] First, the average height of each peptide above the "gold" surface was calculated. The average height for each peptide was obtained by averaging the z coordinate for the terminal nitrogen atom of over frames 2500-4500 of a 5000 frame trajectory. Secondly, the percent helix character for each peptide was calculated, over the same 2000 frames used to determine the average height above the surface. The helix content was determined using the "sscalc" routine in VMD. The output of the "sscalc" routine was used to determine the percent helix by adding the number of

times a residue was determined to be an "h" (α-helix) or "g" (3_{10} helix) and dividing that result by 7 (the total number of residues).

3.4.3.2 Results and discussion

So far we have assumed that the CA_6 adopts an α-helical conformation. Since the CA_6 sequence is short, despite the presence of an oligo-alanine block, the preferred conformation in solution (or under ambient humidity) is likely to be a random coil. The predominant conformation, however, has been shown to change due to assembly on metal surfaces, particularly in the presence of electric field gradients.[124]

To address the preferred conformation of CA_6 in our system, particularly in light of the surface FTIR evidence, molecular dynamics (MD) calculations were performed on an array of CA_6 molecules, simulating the self-assembled monolayers, both with and without an applied electric field. Based on the pI ~5.5 of CA_6,[123] most molecules in the monolayer will be anionic at the carboxylate terminus, but the amine terminus is neutral and unprotonated. Computed MD trajectories using zero applied electric field or fields smaller than 1 V/nm are predicted to exhibit no helical structure or insignificant molecular extension (**Figure 3.11 A**). Upon increasing the applied electric field to 0.5-1 V/nm, the CA_6 molecules are predicted to extend in the applied field and adopt more helical or linear extended conformations (**Figure 3.11 B**, **Figure A14**). At an applied field of 4.3 V/nm, the MD trajectories predict the CA_6 molecules adopt almost exclusively a linear extended conformation (**Figure 3.11 C**), with a correspondingly large increase in average extension above the surface.

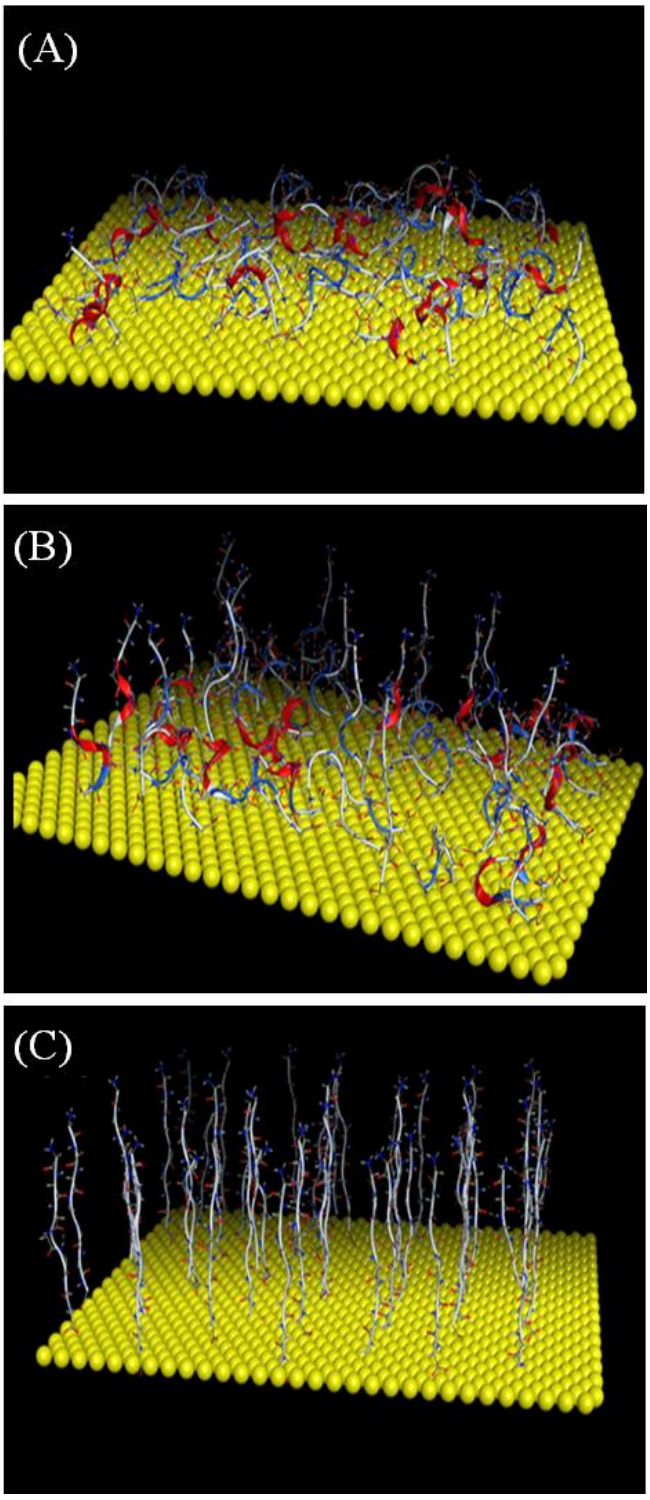

Figure 3.11 Molecular dynamics snapshots of a simulated CA_6 monolayer as a function of increasing electric field at (A) 0 V/nm, (B) 1 V/nm, and (C) 4.3 V/nm. (Data is from Dr. Jeffrey D. Madura).

Fully extended, linear conformations of CA_6 are also predicted to exhibit small piezo coefficients (1.01 pm/V, **Figure 2.17 C**), similar in magnitude to MUA. Thus, these conformations would not be expected to show the greater PFM response in the mixed CA_6/MUA films (**Figure 3.8 D**). When random coil conformations, selected from the MD trajectories at low electric field strength, are optimized as a function of applied electric field, distortions of conformation do occur but not as a smooth linear monotonic function of electric field strength (**Figure 2.17 D**). This confirms the MD results — namely that random or linear conformations of the CA_6 oligopeptide would not reliably, repeatedly deform with linear response to an applied electric field as observed experimentally.

While these MD simulations confirm the experimental observation of piezoelectric deformation in CA_6 monolayers, the predicted piezoresponse is much too large (~7.5Å, **Figure A14**), compared with experiment. Furthermore, classical force fields used in MD cannot properly treat the polarizable electrostatic response of these molecules to an applied electric field. Results from DFT calculations on oligoaminoacids in **Chapter 2** agrees more with the PFM results that the DT and MUA deform significantly less in response to applied electric field.

3.5 SUMMARY

Qualitatively, both DFT-computed response and PFM characterization yield the same conclusion, namely that CA_6 exhibits substantial piezo deformation, while DT and MUA do not because of their rigid molecular shape. The quantitative comparison of computed and PFM measured d_{33} piezo coefficients for CA_6 is good (~14.7 pm/V from DFT and up to ~2 pm/V from PFM). The DFT-computed piezoresponse of completely helical CA_6 represents an ideal upper

bound of the experimentally observed deformation, since the calculation involves a field applied exactly parallel to the molecular axis of a peptide in vacuum and assumes perfect electromechanical coupling. Moreover, peptides with some fraction of both helical and linear conformation, as suggested by MD would have an average of the two responses (e.g., ~7 pm/V for a 50:50 mixture). The PFM technique is, at best, semi-quantitative, since the field from the conductive tip will be applied through an aqueous meniscus, and across a time-varying distance, due to the mechanical frequency of the tapping. Lower indentation on soft materials also provides an effective piezoelectric coefficient smaller than the actual value.[97] Furthermore, based on the tip resolution, the PFM measurement will sample an ensemble of ~10^4 molecules which may not be responding coherently to the AC voltage. For example, recent studies have confirmed that SAMs of helical molecules are disordered and exhibit varying tilt angles near the periphery.[130]

Many previous studies have demonstrated the piezoelectric property of biological materials,[22, 131] and we find that our measured piezoelectric response of monolayers of short peptides correspond well with such reports (in the order of 1 pm/V). While the applied bias voltages used in the PFM experiment appear large (e.g., 3 V), the effective field across the monolayer is undoubtedly much smaller, judging by the computed piezoresponse using DFT. Therefore, we speculate that many proteins may exhibit significant electromechanical response, since electrostatic fields due to molecular dipole moments, ions, etc. are ubiquitous on the nanoscale. Our results also suggest that the observed piezoelectric property of skin, muscle, and other biomaterials, discussed earlier, likely results from aligned helical domains.

There are several key implications of our results. First, it suggests that piezoelectric energy conversion can be used to self-power nanoscale organic electronics, such as flexible touch

sensors. Since the piezoelectric effect also converts electric fields to motion, it also can be used to generate reliable nanoscale linear movement. Existing inorganic nanopiezotronics such as ZnO nanoribbons are difficult to align and pattern, while we demonstrate that simple self-assembly and solution patterning work with molecular piezoelectrics. Finally, one can imagine that the diversity of chemical synthetic techniques, combined with computational simulation and PFM characterization can be used to design highly piezo-responsive monolayers. If possible, this would enable a new class of piezoelectric materials, in which the deformation derives from intrinsic molecular conformational changes.

4.0 CALCULATIONS OF SINGLE MOLECULE FERROELECTRICS

4.1 INTRODUCTION

In this thesis, we show for the first time the concept of single molecule ferroelectrics, where polarization inversion of single molecules due to conformation change is induced by an applied electric field. We will demonstrate this concept using DFT calculations with several molecule prototypes. Molecule structure and functional group effects will be studied in detail for tailoring good ferroelectric single molecules. A broad range of inversion field (~8.8 V/nm) and high spontaneous polarizations (up to 4.5 μC/cm^2) are achieved for several reported and hypothetical buckybowls. These potential molecular ferroelectrics are also good candidates of single molecules piezoelectrics. A significant piezoelectric coefficient d_{33} up to 450 pm/V is calculated for a hypothetical buckybowl derivative.

4.2 COMPUTATIONAL METHODS

The computational methods used for single molecule ferroelectrics are similar to those for single molecule piezoelectrics in **Chapter 2**, namely Gaussian 09[61] and density functional theory (DFT) with the B3LYP functional[62, 63] and the 6-31G(d) basis set. The B3LYP method has been proved to provide quantitatively correct results for the calculation of bowl-to-bowl inversion energy

barrier of corannulenes[58] and sumanenes.[132] We assume this method is similarly applicable in the calculation of all reported and hypothetical buckybowls considered in this chapter.

For all optimizations, the direction of the field was applied along the z-axis defined as from the center of the bowl bottom pointing to the center of the bowl rim (high to low potential from bowl bottom to rim) (**Figure A16**). No constraints were applied to the optimization other than an electric field. Possible translations and rotations of the frame of reference were minimized by select choice of coordinates. The bowl depth is defined as the normal distance between the bottom ring to the outer carbon rims (**Figure 4.1 A**). Molecules with a planar conformation as a transition state between two curved bowls were carefully constructed and optimized to calculate the inversion energy, defined as the energy difference between the curved conformation and the flat conformation (**Figure 4.1 B**). Coercive field is usually a measurable value in real experiments and subject to change to temperature and film thickness.[133, 134] Since all calculations assumes 0 K of temperature and 0 Pa of pressure, we use "inversion field" instead of "coercive field" in refer to the field strength upon polarization inversion.

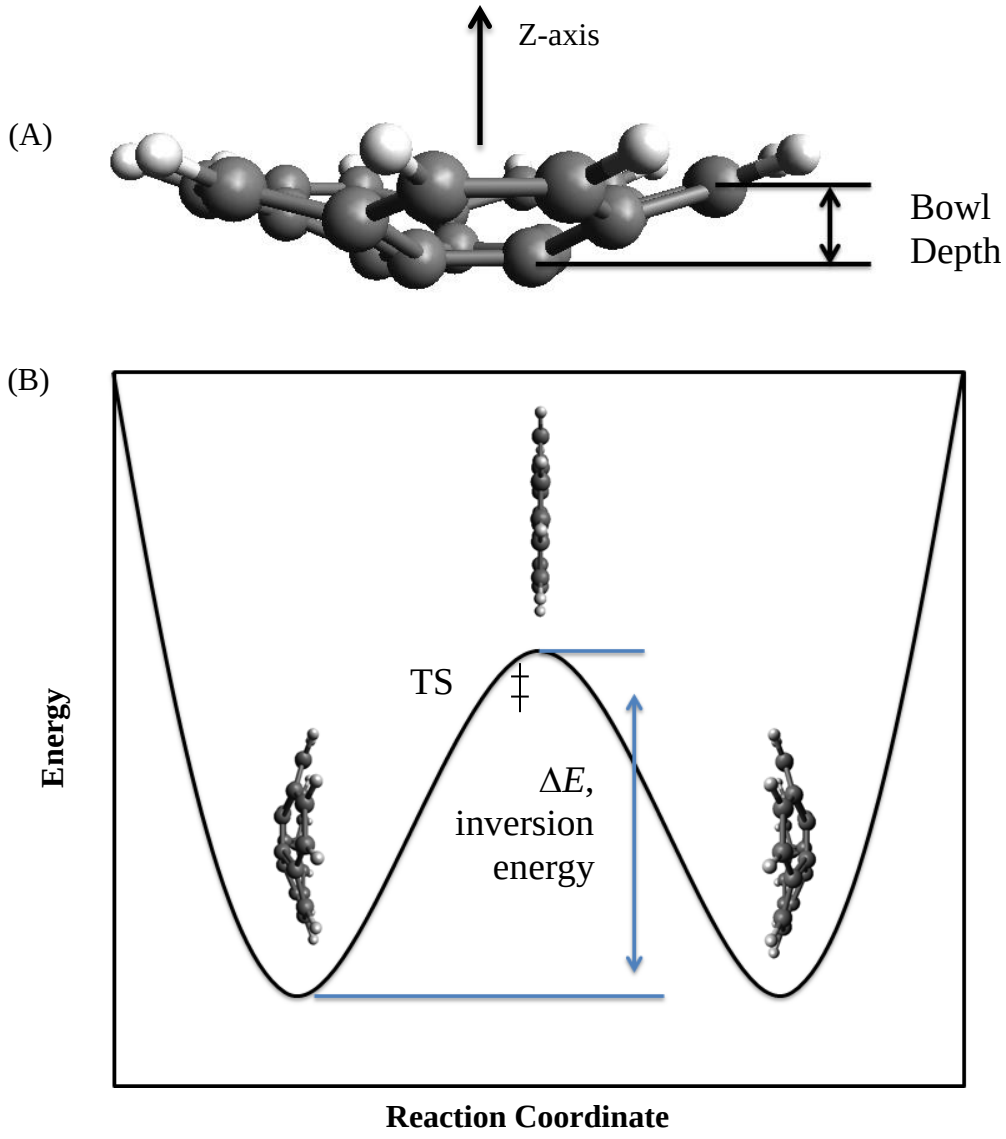

Figure 4.1 Definition of molecule bowl depth (A) and inversion energy (B).

Calculated polarization density (C/m^2) for single molecule ferroelectrics is obtained by taking the calculated total dipole moment (C • m) divided by the estimated molecular van der Waals volume (m^3).[135] In most cases, only the dipole moment was used to indicate the polarization inversion since the molecular van der Waals volume is essentially constant as the molecule deforms.

A very large electric field range (±10 V/nm) has been applied for several molecules to examine the shape – electric field correlation under extreme conditions. For this discussion of single molecule ferroelectrics, intermolecular charge transfer is ignored. Under a high applied electric field, however, intermolecular charge transfer would possibly take place in bulk or thin-films before a bowl-to-bowl inversion would occur.

4.3 RESULTS AND DISCUSSION

4.3.1 Structure effect

Previous studies, both computational and experimental, have shown that there is an empirical quartic relationship between the inversion barrier and the equilibrium bowl depth for buckybowls[60], as expressed by **Equation 5.1**, where ΔE is the inversion energy, x_{eq} stands for the equilibrium bowl depth, and a is a coefficient tailored for a certain structure.

$$\Delta E = -a(x_{\mathrm{eq}})^4 \tag{5.1}$$

We expect that molecules with larger inversion energy and a larger bowl depth will have a higher inversion field, if a possible electric field induced inversion would occur. As we have discussed in **Chapter 2**, molecules can respond to the electric field by performing both shape change and charge redistribution. Dramatic charge redistribution can possibly lead to bond dissociation and to the molecule breakdown, it is hence highly possible that molecules with very high inversion energy would not invert but break down under a large applied field.

We then start the parent calculation with corannulene instead of sumanene, since the former has a smaller bowl depth (0.86 Å) than the latter (1.12 Å). The inversion energy of corannulene is calculated to be 36 kJ/mol, close to the literature value with the same method (36 kJ/mol, B3LYP/6-31G*) and to the experimental value ΔE = 42.8 kJ/mol.[58]

Field range of ±10.28 V/nm was applied along the corannulene C_5 axis from the bottom to the rim of the bowl (the defined z-axis). As the field strength increases, the molecule bends inward and the bowl depth increases due to coupling between the molecular dipole moment and the applied field. The molecule is piezoelectric with a calculated d_{33} of 13.9 pm/V within the field range of 0-1.29 V/nm (**Figure 4.2**). The trend is slightly curved over the whole range of the applied field. At a larger positive field, the deformation above the linear fit is enhanced by the increased π-electron polarization. The bowl depth tends to saturate at larger negative field as increased tension will be experienced over the bowl rim due to bond length extension. Within the field range from 0 V/nm to -10.28 V/m, the bowl depth decreases only from 0.861 Å (at 0 V/nm) to 0.765 Å without a bow-to-bowl inversion taking place.

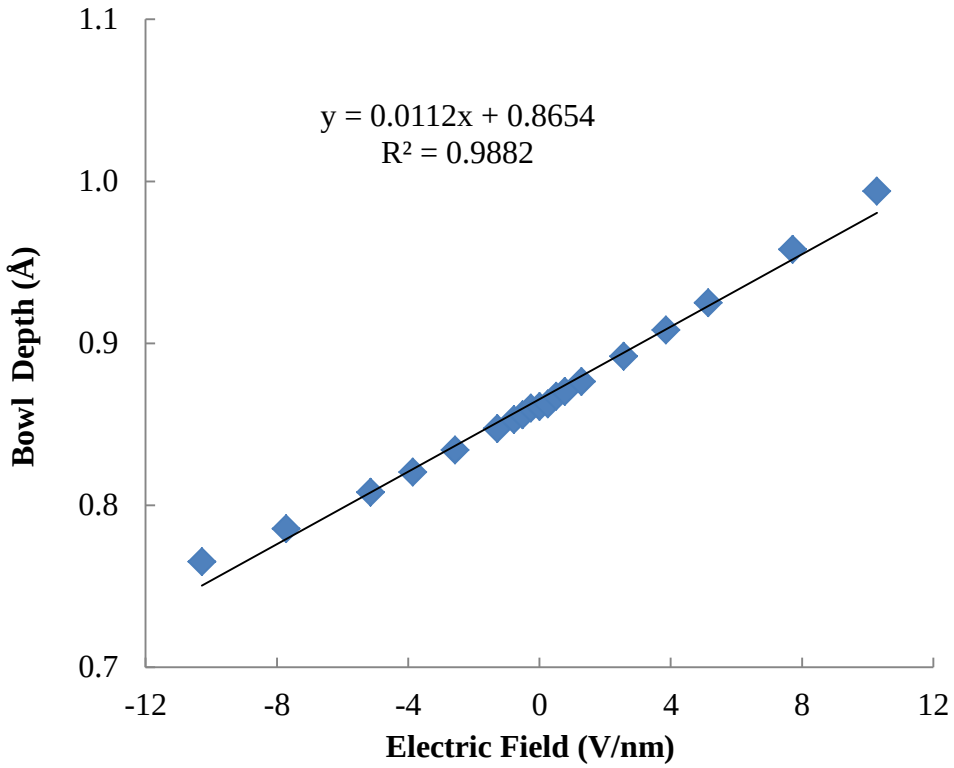

Figure 4.2 Calculated bowl depth of corannulene under applied electric field. Field is applied along the C_5 axis from the bottom to the rim of the bowl. A piezoelectric coefficient d_{33} of 13.9 pm/V is calculated for field range 0-1.29 V/nm.

Still no inversion was observed with even larger negative fields. As shown in (**Figure 4.3**), instead of a bowl inversion, a bending deformation takes place somewhere between -41 to -46 V/nm and C-H bonds dissociate between -46 to -52 V/nm.

Similar results were obtained for sumanene with a stiffer structure. Due to the higher rigidity (higher inversion energy) of sumanene, the calculated d_{33} is only 5.8 pm/V over the field range of 0-1.29 V/nm. No field driven inversion was observed over the field range of ±10.28 V/nm and we assume a similar breakdown would take place as a stronger field is applied.

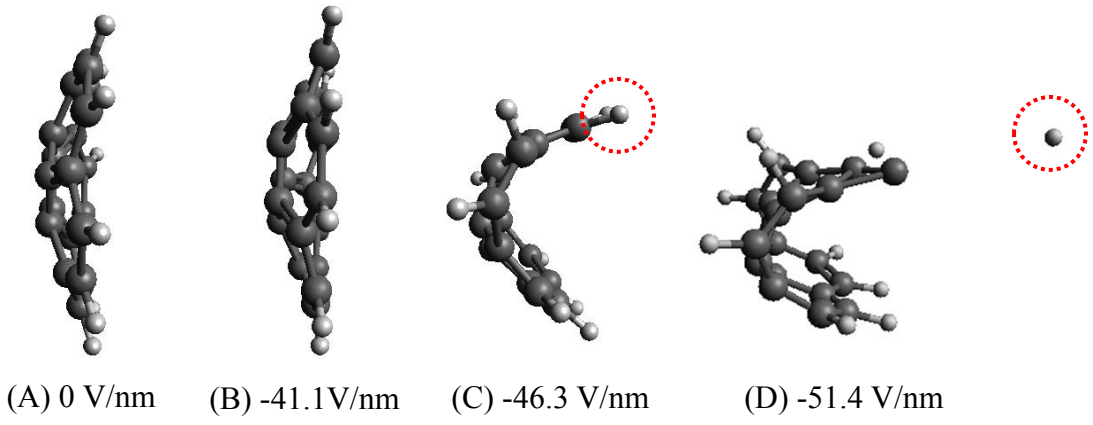

(A) 0 V/nm (B) -41.1V/nm (C) -46.3 V/nm (D) -51.4 V/nm

Figure 4.3 Optimized structures of corannulene under different applied electric field. Under large negative electric field a molecule breakdown take place instead of a bowl-to-bowl inversion.

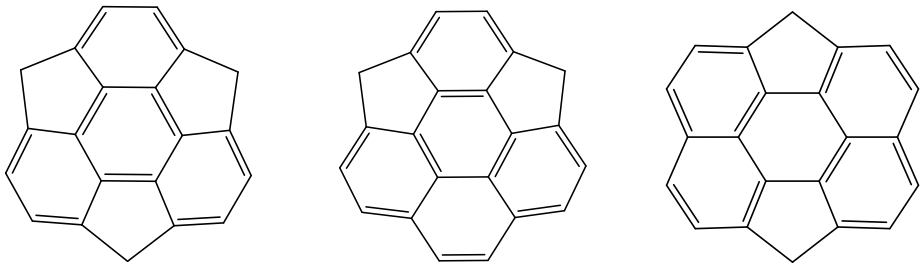

1 **2** **3**

Scheme 4.1Structures of sumanene **1**, 'marsene' **2**, and 'venusene'**3**.

Molecules with a much smaller bowl depth must be considered to enable a possible field-driven inversion. Two hypothetical molecules with a smaller bowl depth were constructed from sumanene. A shallower structure was obtained by replacing one of the five-membered ring in sumanene (**Scheme 4.1**, **1**) with a six-membered ring. A second structure was constructed by rearranging the two left five-numbered rings. We name the former structure as 'marsene' (**Scheme 4.1**, **2**) and the latter as 'venusene' (**Scheme 4.1**, **3**) for convenience. As some of the structure tension is released by replacing a five-numbered ring with a six-numbered ring, the bowl depth for marsene and venusene decreases to 0.632 Å and 0.512 Å, respectively, compared to 0.861 Å of sumanene. The quadratic relationship between inversion energy and bowl depth is satisfied for all the four basic structures considered (**Figure A17**).

Venusene **3** was examined firstly, as it has a smaller bowl depth and is easy to invert. Field range of ± 3.1 V/nm was applied to venusene, and the bowl depth of the optimized structure is measured (**Figure 4.4**). The positive bowl rim is pushed towards the bowl bottom as the electric field becomes more negative. When the field reaches -2.78 V/nm the molecule adopt a near flat conformation (**Figure 4.4 B**). The discontinuity of the depth change indicates the bowl inversion between -2.78 V/nm and -2.83 V/nm. The inversion transition state (a flat conformation) was not captured due to the relatively large default field gradient (~0.05 V/nm) in Gaussian. After the inversion, the bowl depth is identical to that of the optimized bowl at the same field in an opposite direction (e.g. -2.83V/nm to +2.83 V/nm). When the field increases, the bowl maintains its inverted direction and inverts again beyond +2.78 pm/V.

The calculated piezoelectric coefficient d_{33} of venusene is 70.3 pm/V over the field range of 0-1.29 V/nm, higher than helicenes (48.8 pm/V) and phenanthrenes (49.5 pm/V). The bowl depth is more sensitive to the electric field change close to but weaker than the inversion field. This

indicates the existence of a larger d_{33}. When field range of -2.73 to -2.57 V/nm is considered, the calculated d_{33} reaches up to 600 pm/V!

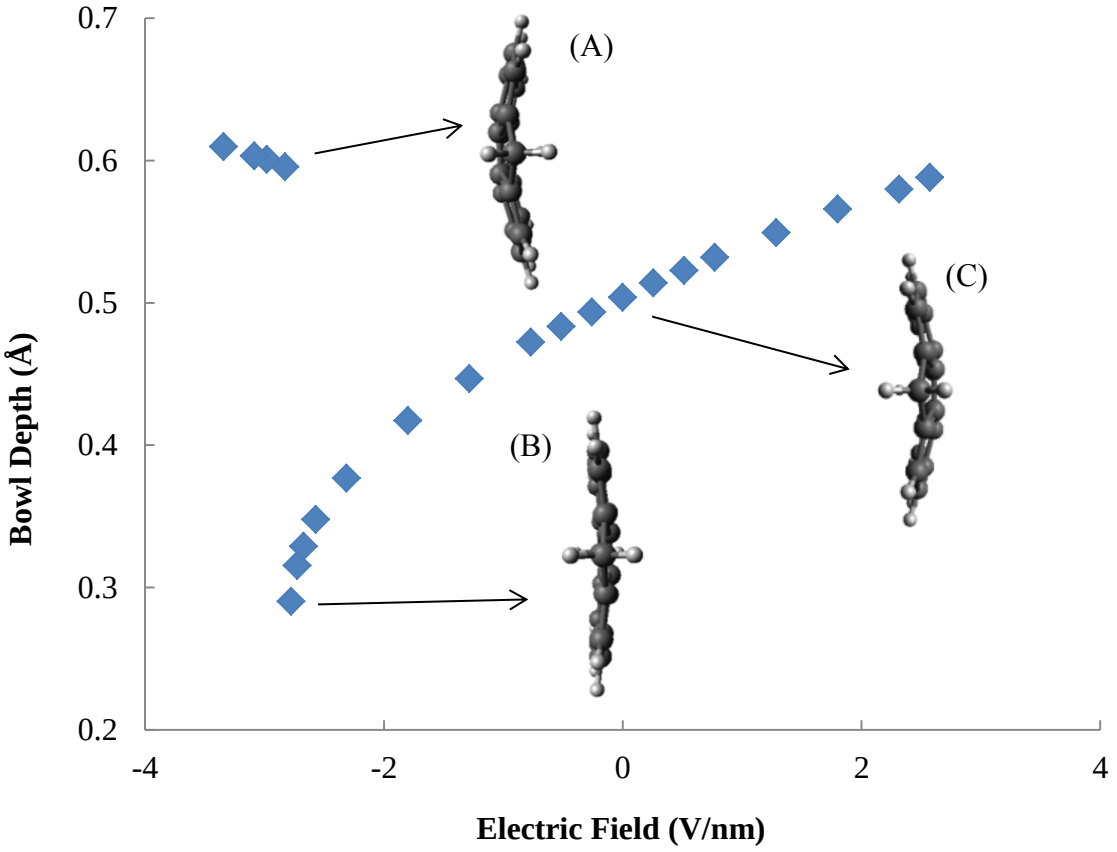

Figure 4.4 Bowl depth of venusene under different applied electric field. Bowl inverts between -2.78 to -2.83 pm/V. The calculated d_{33} is 70.3 pm/V across the field range of 0-1.29 V/nm.

The calculated dipole moment of venusene is 0.97 D along the z-axis and pointing to the positive z-direction. The calculated dipole - field relationship is shown in **Figure 4.5**. When the electric field increases from 0 pm/V (**Figure 4.5 A)** to around -2.7 V/nm, the molecule dipole moment decreases almost linearly. Major dipole moment changes are found when field is approaching negative 2.7 V/nm, where the molecule is "pushed" into a relatively flat conformation (**Figure, 4.5 B, and Figure 4.4 B**). The inverted venusene adopts a conformation with a much larger curvature (**Figure 4.5 C**) and a more negative dipole moment.

When increasing fields were applied to the inverted conformation, only gradual and minor dipole moment change was observed before the field reaches up to 2.7 V/nm. At zero field the dipole (as well as the shape) of the inverted molecule (**Figure 4.5 D**) mirror images the molecule at its initial state (**Figure 4.5 A**). A second dipole inversion takes place between field strength of 2.78 V/nm and 2.83 V/nm, similar to the first inversion at the negative field range. The hysteresis feature of the centrosymmetric dipole-field loop indicates the ferroelectric nature of bowl-shaped venusene.

The estimated spontaneous polarization without applied electric field of single molecule venusene is around 1.1 μC/cm^2. Upon substituents modifications, as will discuss below, polarization up to 4.5 μC/cm^2 is estimated for a cyano-substituted corannulene (decacyanocorannulene, **Scheme 4.2**, **9c**). Such high spontaneous polarization is comparable to that of inorganic (5-75 μC/cm^2) and organic (~10^{-3} to 13 μC/cm^2) ferroelectrics.[13]

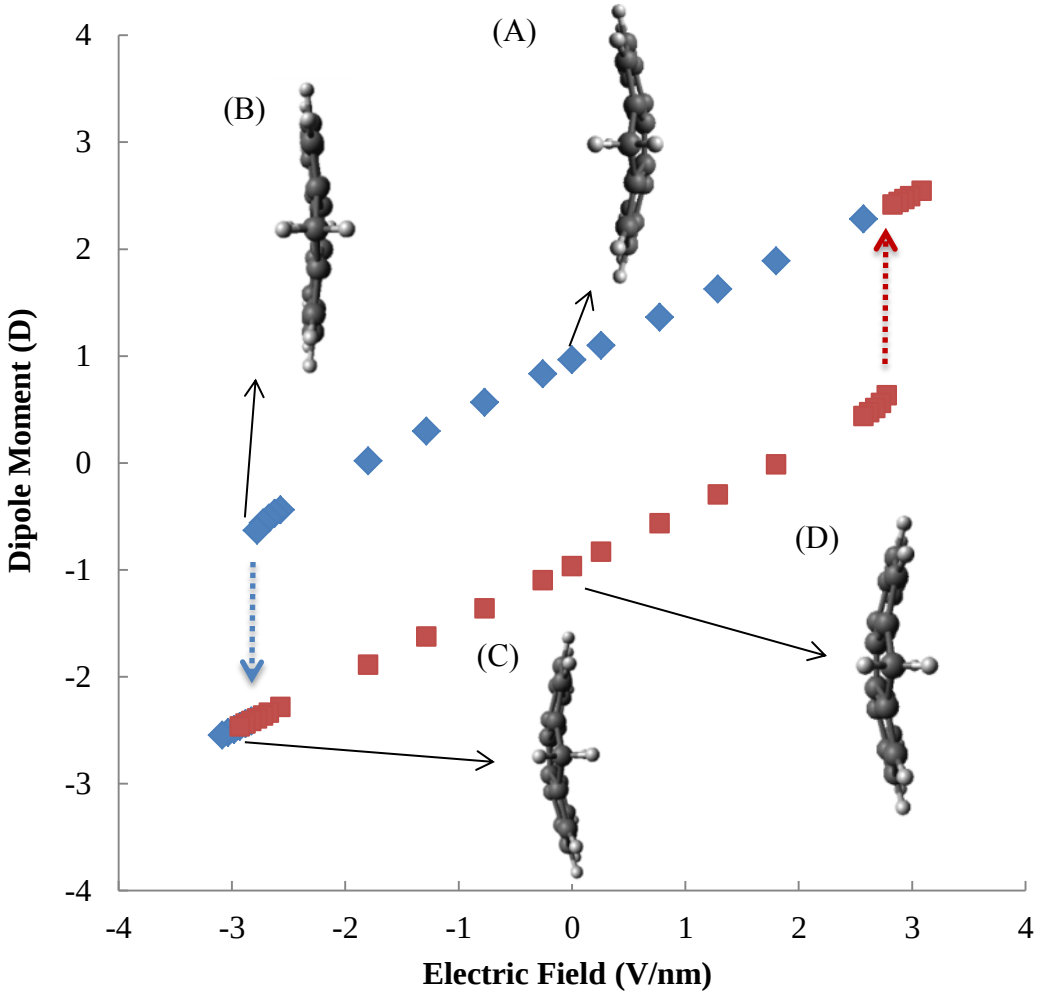

Figure 4.5 Dipole moment change of venusene **3** under different applied electric fields. The initial conformation is indicated as **A**. The upper curve (blue diamond) indicates the dipole moment of optimized venusene starting with conformation **A** under both increasing and decreasing applied fields. The lower curve (red square) indicates the dipole moment of optimized venusene starting with the inverted conformation **C** under increasing applied electric field. At zero field, the inverted conformation **D** is a mirror image of the initial conformation **A** in relate to the defined X-Y plane.

When electric field was applied to the deeper molecular bowl marsene, a similar bowl-to-bowl inversion was observed at a higher inversion field ~±3.9 V/nm. The dipole-field loop has a similar hysteresis feature. The calculated d_{33} within the same field range (0-1.29 V/nm) of marsene is 45.0 pm/V, predictably smaller than that of venusene. Such comparison indicates that buckybowls with a smaller bowl depth are more flexible to deform in response to an applied electric field. However more structures are required for a detailed examination of the relationship between bowl depth and inversion field, as discussed in the following section.

4.3.2 Substituents effect

Previous studies[60, 132] have shown that substituents on corannulene can either increase or decrease the inversion barrier depending on whether the bowl depth is increased or decreased. The repulsion between two *peri* substituents is likely to increase the distance between the two *peri* carbon atoms and hence decrease the bowl depth. If the *peri* substituents tether to form a five-numbered ring (or a six-numbered ring), distance between the two *peri* carbon atoms will decrease leading to an increased bowl depth. Several substituted corannulenes and venusenes (**Scheme 4.2**) are constructed to examine the effect of the bowl depth to the inversion field. All calculated data are listed in **Table 4.1**, including bowl depth, inversion energy, inversion field, dipole moment, and d_{33}.

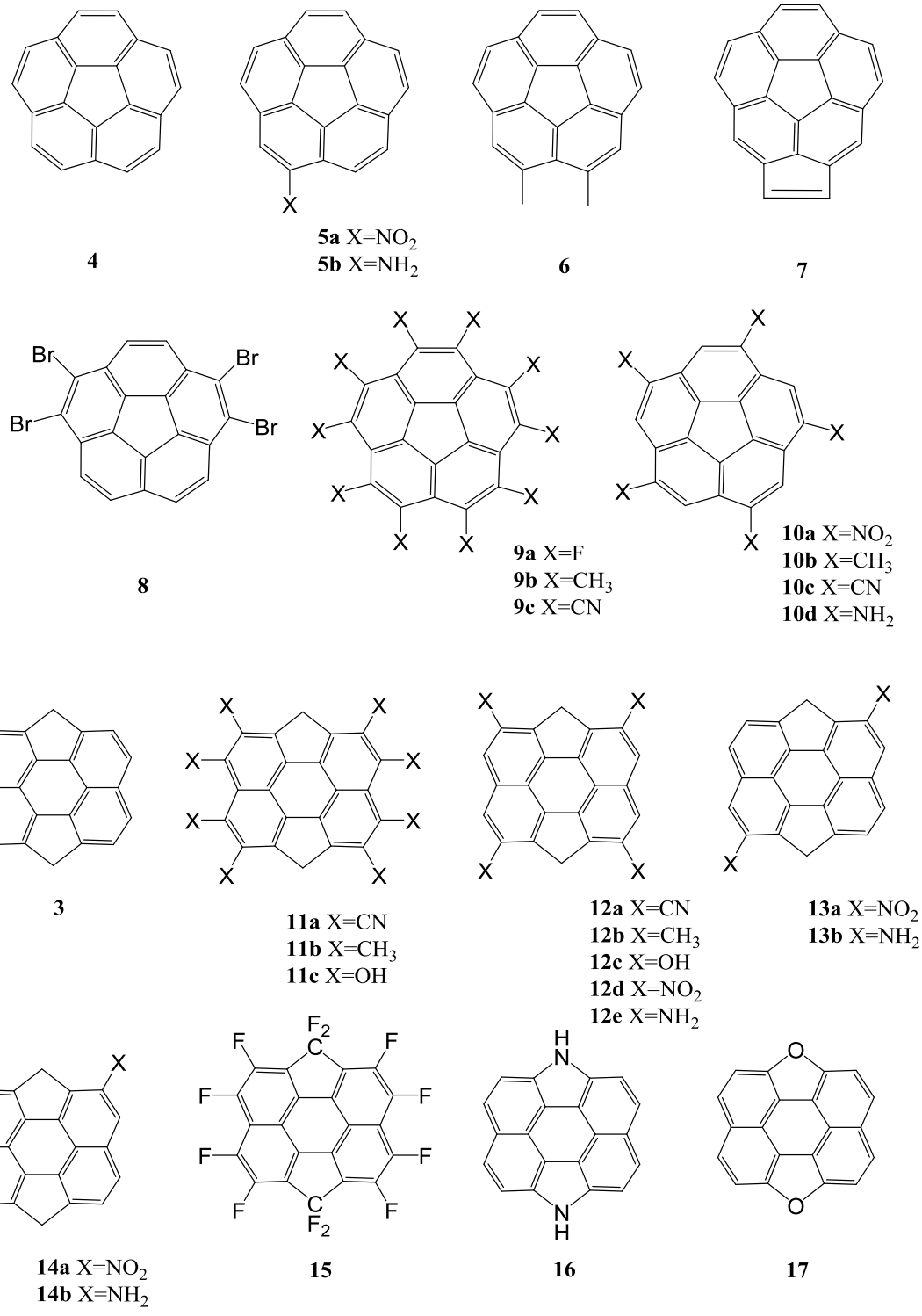

Scheme 4.2 Structures of corannulene, venusene and their derivatives.

Table 4.1 Calculated bowl depth, inversion energy, dipole moment (z-component), inversion field, and d_{33} of substituted corannulenes and venusenes.

structure	bowl depth (Å)	inversion energy (kJ/mol)	dipole moment (D)[a]	Inversion field (V/nm)	d_{33}[b]
corannulenes					
9b	0.597	N/A[c]	-1.13	6.53	29.8
9c	0.642	13.17	4.44	-2.26	66.8
10a	0.693	16.30	2.38	-5.71	31.3
6	0.815	30.32	-1.64	N/A[d]	14.6
8	0.823	34.10	-0.71	N/A[d]	8.68
10d	0.838	33.60	-3.78	9.05	25.9[e]
10b	0.839	35.15	-1.84	N/A[d]	15.6
10c	0.841	34.00	3.43	-7.87	23.2
9a	0.842	34.99	1.38	N/A[d]	9.46
5a	0.856	31.54	-1.03	N/A[d]	6.22
5b	0.857	40.16	-0.94	N/A[d]	16.0
4	0.861	35.83	-1.72	N/A[d]	13.4
7	1.065	111.9	-2.38	N/A[d]	6.15
venusenes					
11a	0.332	0.81	2.38	-0.26	450
11b	0.340	N/A[c]	-0.76	1.08	151
12d	0.447	2.31	1.50	-1.18	134
13a	0.494	2.97	0.43	-5.96	31.4
14a	0.508	3.13	-0.51	N/A[d]	31.8
3	0.512	3.40	-0.97	2.78	70.3
12a	0.522	3.91	1.90	-1.54	101
14b	0.533	8.36	-0.15	-3.60	69.5
13b	0.538	13.57	0.65	-3.29	82.6
12b	0.547	4.60	-1.13	3.14	56.8
12e	0.554	26.07	2.30	-3.60	103
15	0.577	5.49	1.18	-3.70	47.3
12c	0.638	3.38	-1.75	1.49	144
11c	0.725	7.61	-0.95	3.34	206
16	0.839	30.77	-2.63	N/A[d]	22.0
17	1.005	65.18	-1.50	N/A[d]	8.37

[a] Dipole moment z-component if the dipole is not parallel to the z-axis. [b] The d_{33} is calculated over the field range of 0 V/nm to 1.29 V/nm (or -1.29 V/nm if negative field leads to larger bowl depth). [c] An optimized planar conformation is not available for inversion energy calculation. [d] Inversion field is either beyond ± 10.3 V/nm or absent due to molecule breakdowns. [e] The d_{33} is calculated over the field range of 0.26 to 1.29 V/nm.

Upon the 29 structures (**Scheme 4.2**) examined, we find that a larger bowl depth is generally accompanied with a larger inversion energy. The quartic relationship between inversion energy and bowl depth basically holds for all corannulenes and venusenes (**Figure 4.6**). Different substituents could provide a large range of bowl depth (0.597 Å to 1.065 Å for corannulenes and 0.332 Å to 1.005 Å for venusenes) and a large range of inversion energy. A minor jump in bowl depth can significantly increase the inversion energy due to the quadratic relationship.

The apparent deviations from the linear fit are the two hydroxyl- and amino- substituted venusenes (**11c, 12c, 12e, 12b, and 14b**) (**Figure 4.6 B**). For the two hydroxyl-substituted venusenes the deviation in energy might result from the rotation of the C-O bond which could lower the transition state energy. In the case of the amino-substituted venusenes, the planar conformation assumes that the H-N-H angle in $-NH_2$ group is close to 120˚, and all the atoms are in the same plane. However, this may not be true when those molecules invert. The inversion energy of pyramidal $-NH_2$ in methyl carbomate is reported to be only 0.66 ± 0.07 kJ/mol,[136] close to our calculated energy difference (~0.73 kJ/mol) of two $-NH_2$ pyramids pointing to the opposite direction relative to the bowl rim.

Such a small energy barrier can also be overcome by an applied electric field. The inversion of pyramidal $–NH_2$ could change the molecular dipole moment dramatically. This effect of the pyramidal $–NH_2$ inversion will be discussed in detail later in this chapter.

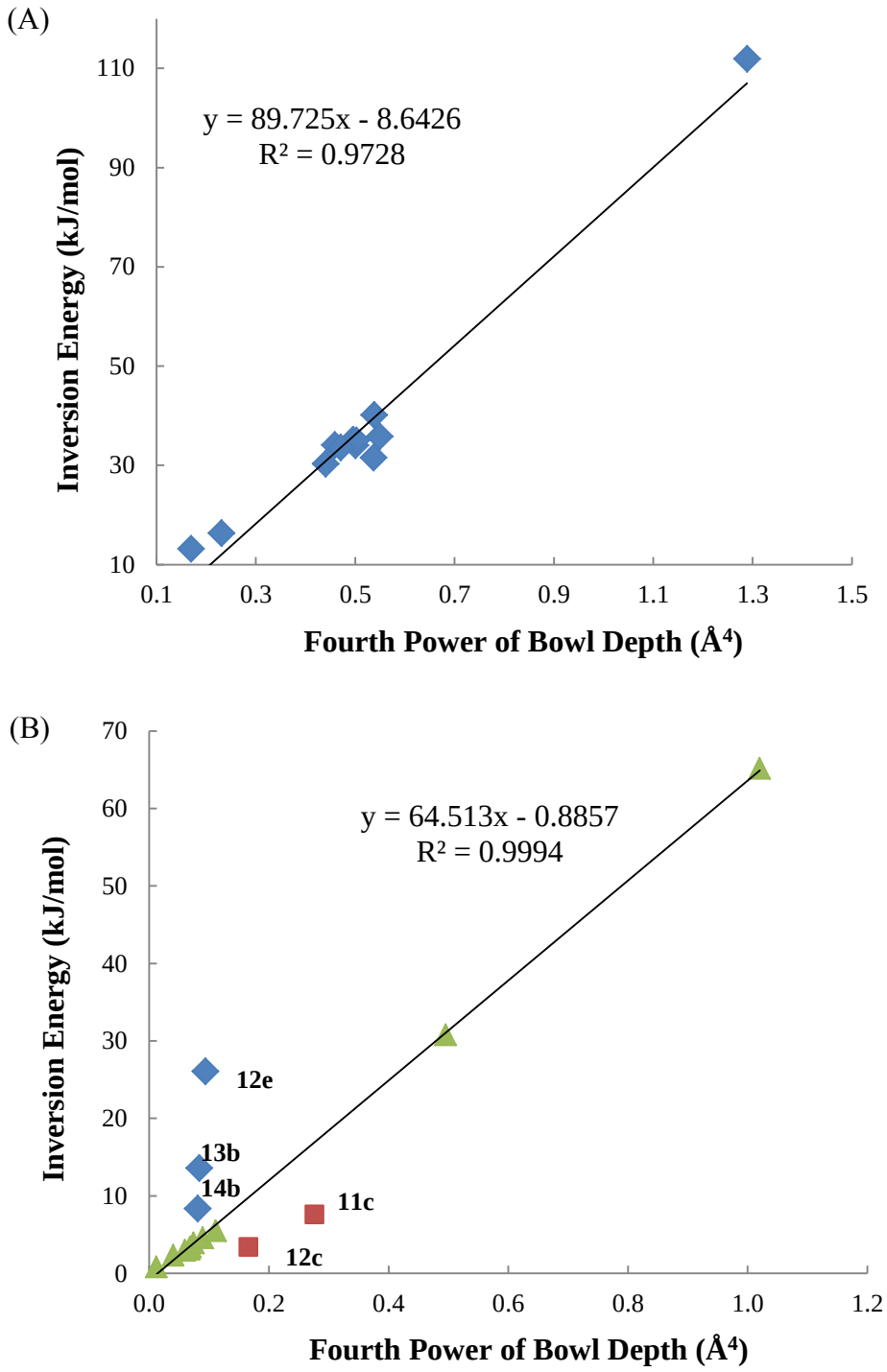

Figure 4.6 The inversion energy - bowl depth correlation of corannulenes (A) and venusenes (B). The C-O bond rotation of-OH group and the inversion of pyramidal -NH_2 complicate the calculation of bowl-to-bowl inversion.

Substituents play a significant role in tuning the molecule bowl depth and the inversion field. In general, shallower bowls are more likely to be inverted by an electric field (**Figure 4.7**). As the bowl depth decreases, an inversion field below 10 V/nm starts to appear for substituted corannulenes. A similar trend is present for substituted venusene, although some substitution elevates the venusene bowl depth. A large range (~ 8.8 V/nm) of the inversion field is observed across all 29 structures with the lowest inversion field of 0.26 V/nm for octacyanovenusene (OCV, **11a**). Such low inversion field is well below the breakdown voltage of dielectric polymer PVDF (0.77 V/nm),[137] making single molecule ferroelectrics more promising in real applications.

For PZT ferroelectric (ultra)thin films and alike, the coercive field *increases* as the film becomes thinner, following an empirical law $E_c\ (d) \propto d^{-2/3}$, where E_c stands for the coercive field and d for the film thickness.[138, 139] However, the molecular bowl depth and PZT film thickness are different in nature and thus not a valid comparison in concept. A deeper molecular bowl stands for a higher inversion barrier and hence a higher inversion field; while a thicker PZT film doesn't change much of the crystal structure. The increase of the coercive field in ultrathin ferroelectric films may partially result from the effect of a conductive nonferroelectric layer between the film and the metal electrode.[140] As the film becomes thinner, the screening effect of the conductive layer (a voltage drop) reduces the voltage applied to the ferroelectric film.

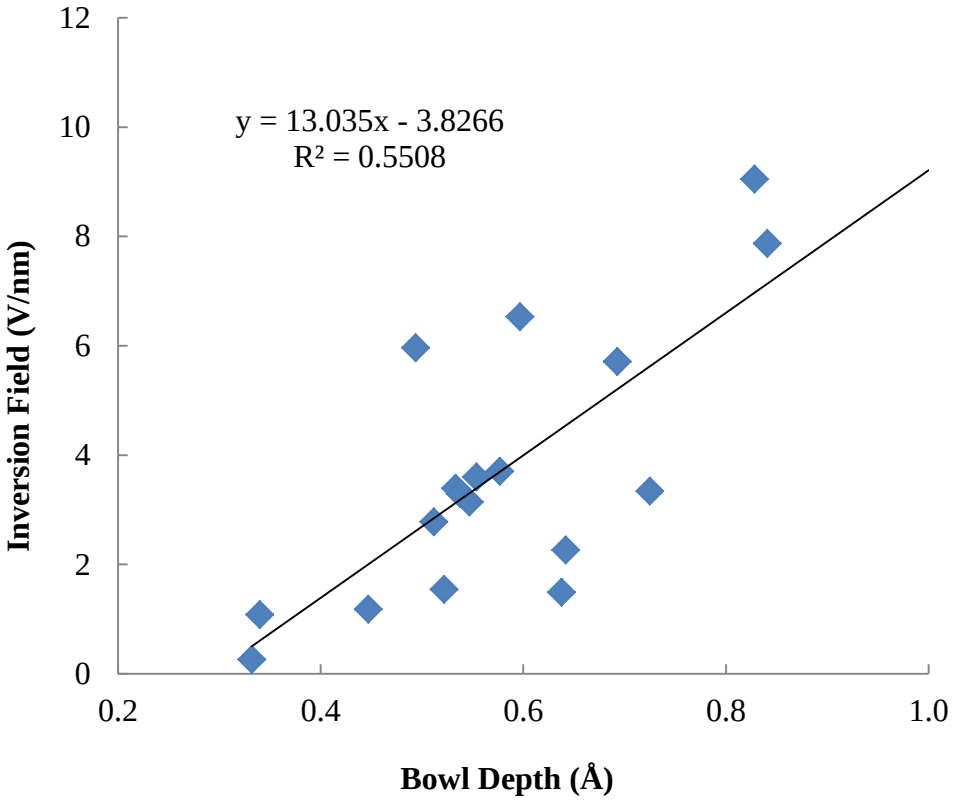

Figure 4.7 Calculated inversion field - bowl depth correlation of all corannulene, venusene, and their derivatives. The inversion field is absent for some molecules, as listed in **Table 4.1**.

In the case of corannulenes, it seems that either a strong electron withdrawing group (-CN, -NO_2, etc.) or a strong electron donating group (-OH, -NH_2, etc.) could significantly lower the inversion field without dramatically decreasing the bowl depth. For example, pentacyanocorannulene (PCC, **10c**) has a slightly larger bowl depth (0.841 Å) than that of pentamethylcorannulene (PMC, **10b**) (0.839 Å), but PCC inverts at much lower electric field (7.87 V/nm) than PMC, which may breakdown under a larger electric field instead. However, such trend is not so clear in the case of venusenes.

It is noticeable that for all the molecules considered (except for 1-aminovenusene, **14b**) the dipole moment is in the same direction of the inversion field (**Figure 4.8**). It suggests that the electric field induced inversion is a result of the dipole-field coupling due to limited charge redistribution within the molecule π-orbitals. This also helps explain the lower inversion field of stronger electron withdrawing/donating group substituted structures.

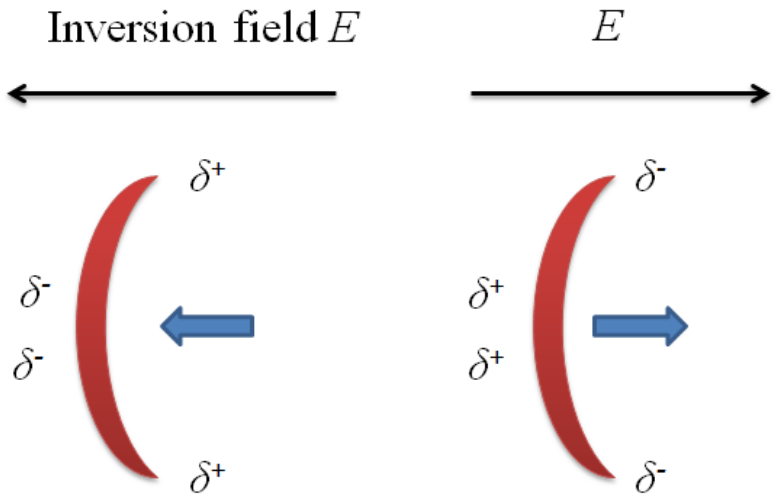

Figure 4.8 Inversion field is in the same direction of the molecule dipole.

The change of the bowl depth, or the molecule thickness, to the electric field of all structures is similar in shape (see **Figure 4.4**) with the inversion field occurring at different electric field strength. A linear trend is observed within a small electric field range (e.g. within ± 1.29 V/nm) and a dramatic jump near but before the inversion field. Surprisingly large calculated piezoelectric coefficients are observed for venusene and substituted venusenes. All of the calculated d_{33} values are listed in **Table 4.1**. The d_{33} of octacyanovenusene (OCV) reaches up to 450 pm/V over the field range of 0 - 1.29 V/nm, which is comparable to PZT piezoelectrics and higher than all the rest known piezoelectrics. Such a significant d_{33} of OCV may result from the small bowl depth and the resulted great flexibility of the bowl.

The trend is not clear in both the relationship of bowl depth to d_{33} and the relationship of dipole moment to d_{33} (**Figure A18**). However, the d_{33} seems to decrease exponentially as the inversion field increases (**Figure 4.9**). Similar phenomena have been reported for conventional PZT ferroelectrics and alike.[36-38] The so-called size effect discussed in **Chapter 2** describes the decreasing trend of d_{33} to the decrease of the film thickness. On the other hand, the d_{33} decreases as the coercive field increases based on the fact that thinner films tend to have a higher coercive field. Such similarity, along with the significant calculated piezoelectric coefficient of venusene derivatives, may shed lights on the possible replacement of conventional perovskite ferroelectrics by their counterparts of single molecule piezoelectrics for future small scale, flexible, high density, and patterning-rich applications.

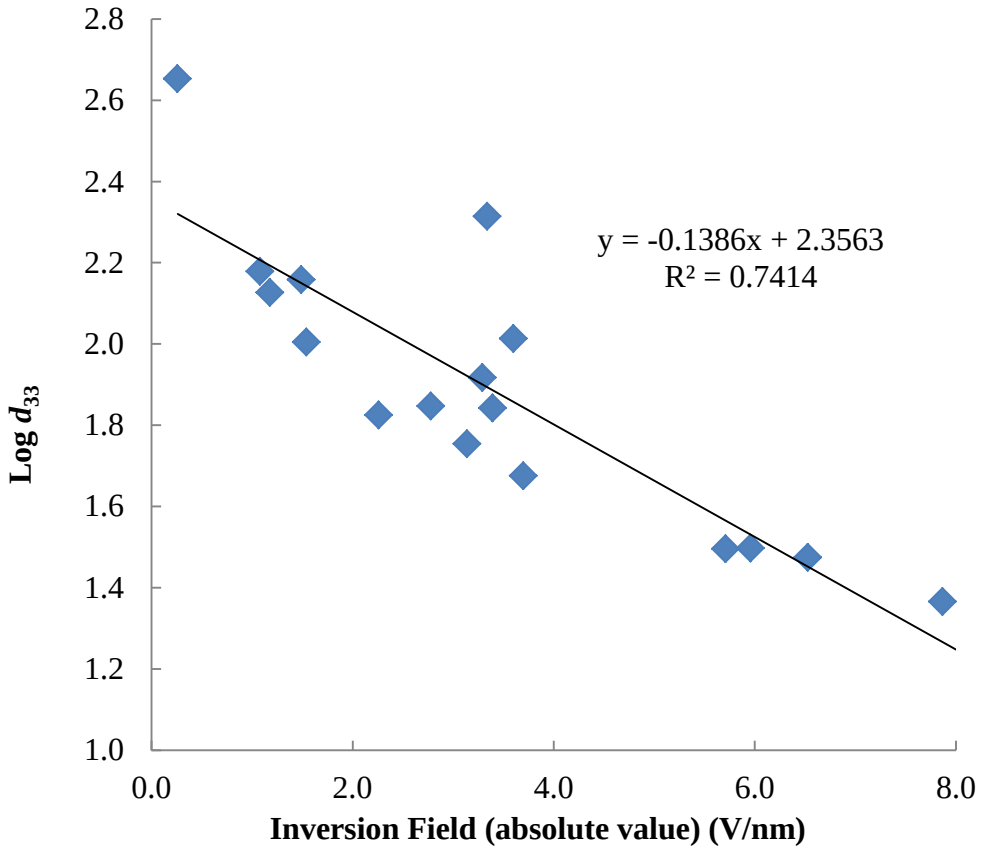

Figure 4.9 Correlation of d_{33} to bowl depth and inversion field. The absolute value of inversion field is considered as a measure of the easiness to invert.

4.3.3 Multistate ferroelectrics

The inversion of pyramidal -NH_2 mentioned earlier (Section **5.3.1** and **Figure 4.6 B**) will change the molecular dipole moment dramatically without inverting the molecular bowl. Depending on the orientation of the -NH_2 groups, the overall dipole moment of amino-substituted buckybowls could reside at four different states of different magnitude and/or directions. Such molecules can be viewed as a model of multistate ferroelectrics.[33, 141, 142] The working principle of this multistate ferroelectric model is illustrated using tetraaminovenusene (TAV, **12e**) as an example in **Figure 4.10**.

TAV has a large dipole moment of 5.88 D under zero electric field if the two hydrogen atoms in each -NH_2 group bend to the positive direction of the z-axis (**Figure 4.10 *a***). The dipole moment decreases in a near linear fashion as the field increases. At around 1.39 V/nm the molecular bowl inverts and the dipole moment drops from 4.45 to 0.73 D. The inverted TAV has a dipole moment of 2.29 D if zero field is applied (**Figure 4.10 *b***). Under larger electric field, the dipole moment continues to decrease and dramatically drops from -1.54 to -8.26 D at around 3.19 V/nm where the four -NH_2 groups invert to the negative direction of the z-axis (**Figure 4.10 *d***). When the field starts to decrease, conformation ***d*** maintains (with gradual attenuation of the bowl depth), and the bowl inverts again at -1.39 V/nm with the dipole moment increase from -4.45 to -0.73 D. The inverted conformation has a dipole moment of -2.29 D free of applied electric field (**Figure 4.10 *c***). The dipole moment - electric field curve is centrosymmetric with multiple hysteresis loops.

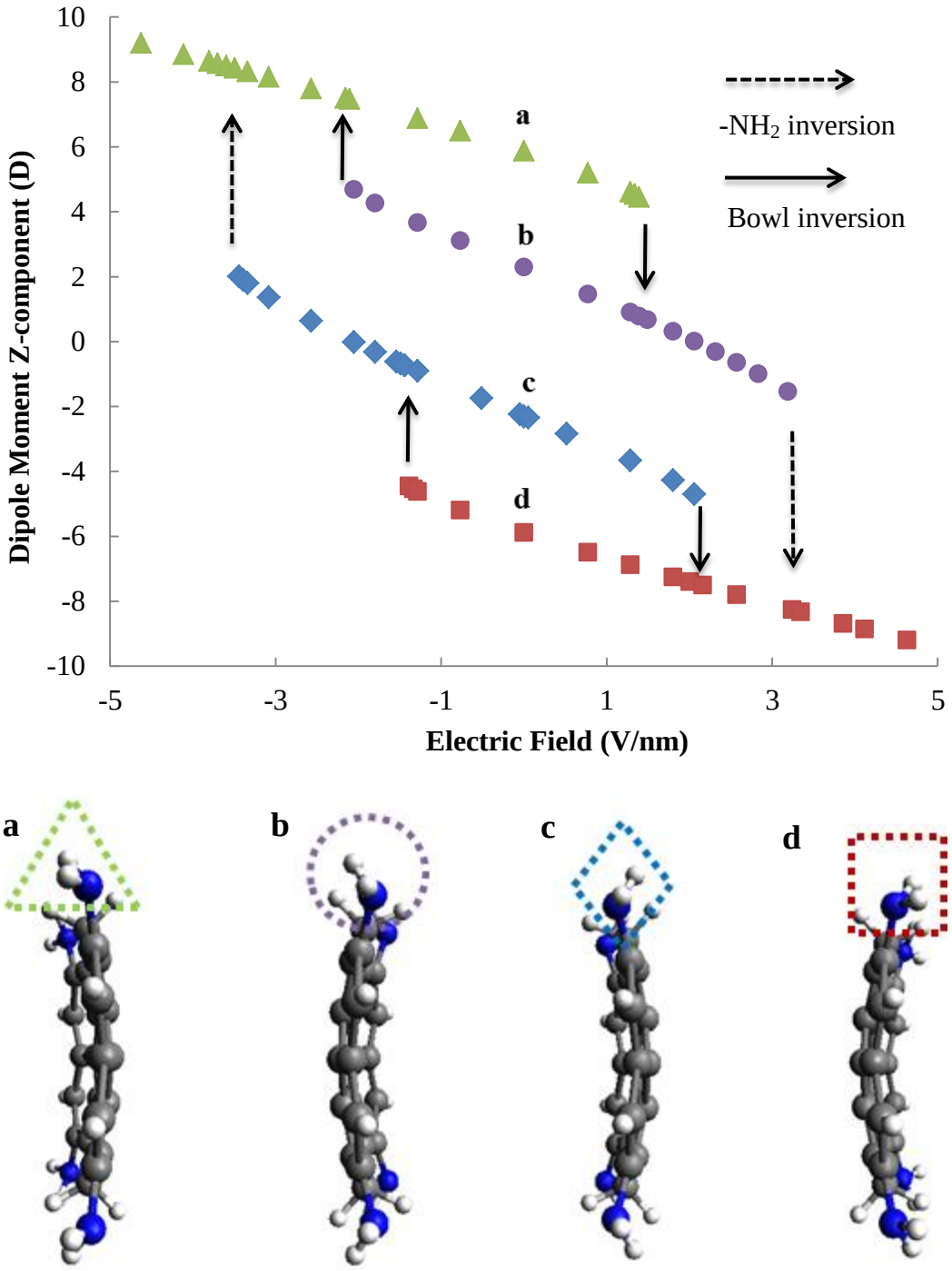

Figure 4.10 (Top) Dipole moment z-component of tetraaminovenusene (TAV, 12e) under different applied electric fields. (Bottom) The four stable conformations TAV adopt at 0 V/nm with a dipole moment different in magnitude and/or direction. TAV can be viewed as a single molecular model of four-state ferroelectrics.

TAV has four spontaneous polarization states which can be altered by applied electric fields. One step switch is infeasible between conformation ***a***, ***d***, and ***b***, ***c***, respectively. Switch between any two of the four states can be achieved by applying a maximum of two sequential applied electric fields.

4.3.4 The effect of temperature and crystal lattice

Note that the DFT calculations assume 0 K of temperature and thus zero kinetic energy of the molecule. So the calculated inversion field cannot be directly used to estimate the behavior of molecules in reality (e.g. in room temperature). A higher temperature will lower or eliminate the energy barrier of such an inversion. Corannulene is reported to invert above -64˚C in solution, and the inversion is estimated to take place over 200,000 times per second at room temperature.[143] Giving that a huge range of inversion energy can be achieved through structures and substituents modification of buckybowls, it is highly promising that careful computational design and versatile synthetic strategy could lead to room temperature or even high temperature single molecule ferroelectrics.

Similarly, the multistate ferroelectricity of TAV could be possibly achieved only at very low temperatures due to the small energy barrier of pyramidal -NH_2. However, the concept of combining two different types of field-induced polarization inversions is still inspiring in the design of new multistate ferroelectrics.

On the other hand, molecular packing constraints in crystals or multilayers may prevent the molecule from inverting and elevate the inversion field. Such constraints may also obstruct the inversion of the pyramidal -NH_2 group hence chances of the inversion may be left for applying an electric field. Single molecule based ferroelectrics with a broad range of inversion field in

room temperature or higher could be promisingly constructed combining both structures/substituents effect and molecular packing constraints.

4.4 SUMMARY

We have demonstrated the polarization hysteresis of single molecules under applied electric fields. The polarization inversion is achieved via molecular conformational change, namely the bowl-to-bowl inversion, of a group of hypothetical buckybowls and their derivatives. Such mechanism is different from both 'displacive' and 'proton-transfer' mechanisms of conventional inorganic and organic ferroelectrics. Recently, this idea has been experimentally realized via a hexagonal columnar liquid crystal assembly consisted of umbrella-shaped molecules,[144] which is analogous in shape to buckybowls.

Both molecule structure (bowl depth) and substituents play an important role in determining the ferroelectric property of the molecules. A large bowl depth elevates the inversion energy barrier and leads to a higher inversion field. Molecules with a barrier larger than 34 kJ/mol are likely to break down rather than invert under stronger electric field. The bowl depth also changes as different substituents are introduced to add or release tension of the curved bowl. For example, the bowl depth of corannulene is likely to decrease due to the repulsion from two *peri* substituents and to increase if the two *peri* substituents bridge to a five-numbered ring. Both the magnitude and direction of the dipole moment can be changed by different substituents which could change the polarization and the sign of the inversion field.

From above findings, structures of good single molecule ferroelectrics are proposed with a large range of inversion field (~8.8 V/nm), a high spontaneous polarizations (up to 4.5 μC/cm^2

for decacyanocorannulene), and a huge piezoelectric coefficient d_{33} (up to 450 pm/V for octacyanovenusene). Such values are comparable or even superior to all ferroelectric materials reported so far. A new type of single molecule ferroelectrics via molecule conformational change may be created.

5.0 CONCLUSIONS AND OUTLOOK

5.1 SUMMARY OF RESULTS

This thesis studies single molecule piezoelectrics and single molecule ferroelectrics via both computational and experimental means.

In particular, we propose and study three kinds of single molecule piezoelectrics and one kind of single molecule ferroelectrics through density functional (DFT) calculations. Fundamental insights into the effects of molecular structure, functional groups, dipole moment, and regiochemistry on single molecule piezoelectrics/ferroelectrics are developed. Guided by those design rules, significantly large piezoelectric coefficients and a broad range of inversion field are found for hypothetical helicenes, phenanthrenes, and molecular "buckybowls".

We perform piezoresponse force microscopy (PFM) and Fourier-transform infrared spectroscopy (FTIR) studies on samples of patterned self-assemble monolayers (SAMs) of oligoaminoacids, and demonstrate single molecule piezoelectricity for the first time. By introducing alkylthiols as built-in controls, we were able to rule out instruments artifacts and to distinctively show the piezoelectric amplitude of oligoaminoacid SAMs.

Combining with our computational predictions, we propose a new class of piezoelectric/ferroelectric materials from the "bottom up" for fabricating next generation flexible,

large scale, ultrathin, and lightweight electronic devices. Here I briefly summarize the main conclusions in the previous chapters.

- We demonstrate that single molecules can perform large conformational change in response to an applied electric field. Regioisomers, polarizability, and Hammett-Taft constant of functional groups are important factors to good single molecule piezoelectrics. Piezoelectric responses, up to 272 pm/V, have been predicted for helicenes, phenanthrenes, and their derivatives with extended fused benzene rings.
- We provide both qualitative and quantitative experimental results to show that oligoaminoacid CA_6 is piezoelectric. The computational and experimental piezoelectric coefficients of CA_6 agree semi-quantitatively with each other, and are larger than the more rigid built-in control molecules. Using microcontact printing methods, fabricating large scale monolayer electronics devices is becoming possible.
- We further extend the idea of single molecule piezoelectrics to single molecule ferroelectrics via computational study on molecular buckybowls. We show that the conformation and polarization of these bowl-shaped molecules can be inverted by an applied electric field of a broad range (~8.8 V/nm). We construct a hypothetical buckybowl derivative with a huge piezoelectric coefficient of 450 pm/V, comparable to the best conventional PZT piezoelectrics. We also propose a molecular model for multistate ferroelectrics.

5.2 OUTLOOK OF FUTURE DIRECTIONS

Single molecule piezoelectrics and ferroelectrics are promising candidates for fabricating next generation flexible, large scale, ultrathin, and lightweight electronic devices. Computational studies have shown molecular prototypes with high piezoelectric coefficients and a broad range of inversion fields. Comprehensive synthetic, fabricating, and characterizing methods are necessary for further demonstration and development of this new class of materials.

Beyond the work in this thesis, the following questions remain interesting for future studies.

- DFT calculations assume 0 K of temperature and 0 P of pressure. We have shown large piezoelectric/ferroelectric responses of single molecules under such conditions. It would be interesting to know how such behaviors would change if temperature and pressure are concerned. It would also be interesting to study the collective behavior of single molecule piezoelectrics and ferroelectrics in the form of multi-layers and crystals.
- Many of the synthetic methods only yield un-substituted or symmetrically substituted helicenes,[145] which are predicted to be non-piezoelectric. More effective and efficient synthetic methods are needed to provide potential piezoelectric molecules for testing and device making.
- Using PFM and FTIR, we have demonstrated the converse piezoelectric effect, namely the electric field-induced deformation, of oligoaminoacids at the level of a self-assembled monolayer. To push single molecule piezoelectrics further into real applications, it is necessary to demonstrate the direct piezoelectric effect (strain-induced potential change) as well. The fabrication of multi-layers and bulk materials is also appealing.

APPENDIX A

SYNTHESIS OF ASYMMETRICALLY SUBSTITUTED HELICENES

1. Introduction

Helicenes are a class of phenanthrene derivatives in a regular cylindrical helix form, which is formed by the repulsion of nuclei on the overlapped terminal aromatic rings. Such a helical structure renders helicenes chiral, though no asymmetric carbons or other chiral centers are present. As such helicenes have achieved wide applications ranging from asymmetric catalysis,[146, 147] molecular machines,[148-150] molecular recognition,[151, 152] and to liquid crystals.[153]

Depending on the number of the ortho-fused benzene rings, a Greek prefix or a number in brackets, [n], is added before the name 'helicene' for simplicity.[154] Hexahelicene or [6]helicene, for example, stands for helicenes with six fused benzene rings, as shown in **Scheme A1**. Since [6]helicene is chosen as a piezoelectric prototype in this thesis, the nomenclature 'helicene' is referred to [6]helicene unless otherwise specified.

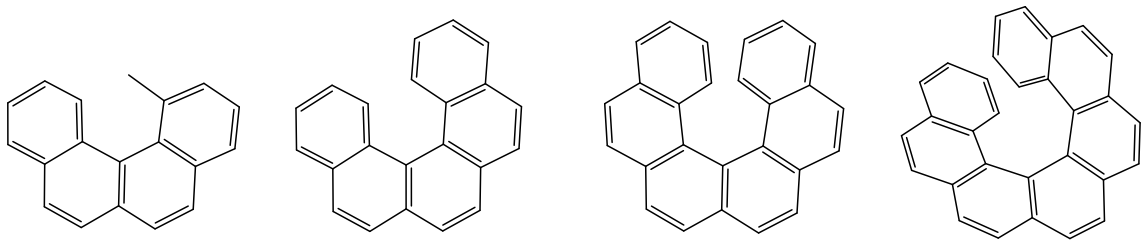

1 **2** **3** **4**

Scheme A1. Structure of [4]helicene **1**, [5]helicene **2**, [6]helicene **3**, and [7]helicene **4**.

The first [6]helicene was synthesized in 1956 by Friedel-Crafts cyclization of carboxylic acid compounds.[154] Since then, the synthesis of [6]helicenes with different number of fused benzene rings and different substituents has been reported with many different methods.[155-163] Since we are targeting asymmetrically substituted [6]helicenes as promising single molecule piezoelectrics, only a limited number of synthetic methods are potentially adoptable. In this thesis, we will follow the synthetic route reported by Aloui *et. al*,[155] where an asymmetrically substituted helicene, 3-bromo-14-methoxo[6]helicene (**3b14m**, **11**) is obtained with only four steps. The first and the third step is a Heck coupling reaction where 4-bromostyrene **5** and 3-bromostyrene **9** is attached to 2-bromo-6-methoxynaphthalene **6** and 2-bromo-10-methoxy-benzo[*c*]phenanthrene **8**, respectively, in the presence of sodium acetate and Hermann's catalyst in *N*,*N*-dimithylacetamide. The second and the last step is a photocyclodehydrogenation where the diarylethene of **7** and **10** fused into a benzene ring using a high-pressure mercury lamp in cyclohexane with 1.1 equiv. of I_2 and excessive propylene oxide (**Scheme A2**).

The calculated d_{33} of **3b14m** is 19.3 pm/V over the field range of 0 - 1.29 V/nm, smaller than the best piezoelectric helicenes (**4a15n**, 48.8 pm/V) but greater than the calculated d_{33} of helical CA_6 (14.7 pm/V). **3b14m** is still a good single piezoelectric candidate for PFM measurements.

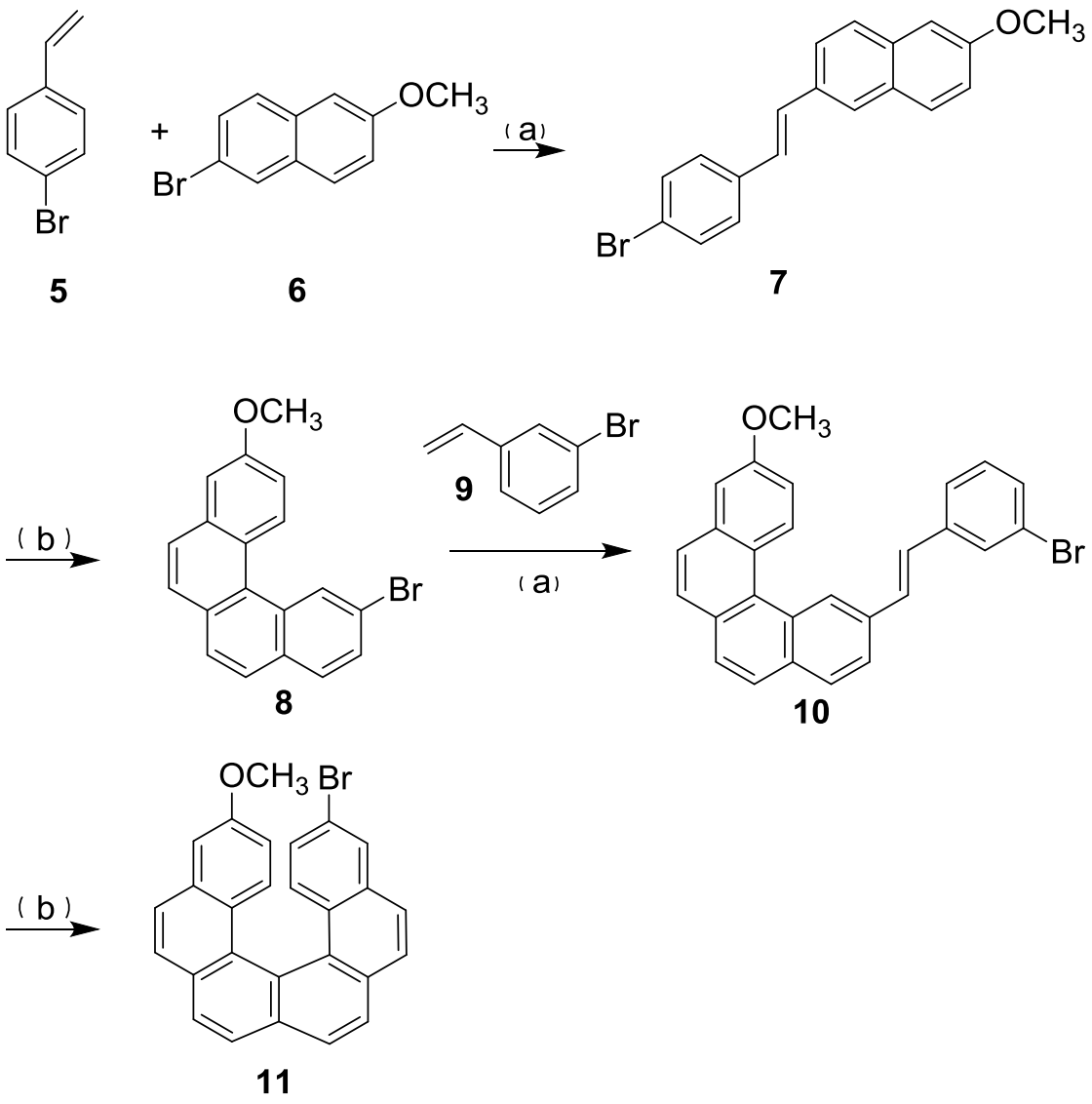

Scheme A2. Reagents and conditions: (a) Hermann's catalyst (1%), NaOAc (1.1 equiv), *N*,*N*-DMA, 140 ℃, 48h; (b) *hv*, I_2 (1.1 equiv), propylene oxide (excess), cyclohexane, 1.5h. (Ref.[155])

2. Experimental Methods

Materials and equipment

2-bromo-6-methoxynaphthalene (97%) and 3-bromostyrene (97%) were purchased from Fisher/Acros. 4-bromostyrene (98%), *N*,*N*-dimethylacetamide and (±) propylene oxide (98%) were purchased from Aldrich Chemical Co., Inc. Hermann's catalyst (trans-di(μ-acetato)bis[o-(di-o-tolylphosphino)benzyl]dipalladium(II), 97+%) was purchased from Stream Chemicals, Inc. All chemicals were used as received without further purification.

Argon (grade 4.8) was supplied by Valley National Gases. The photo-reactor is self-designed and fabricated from the university glass shop (**Figure A1**). The UV light source is from Philips (319657 H39kb-175 Mercury Vapor Lamps, 175W, with outer glass shell removed by the University of Pittsburgh glass shop). Electronic ballast is allocated from the University of Pittsburgh electronics shop.

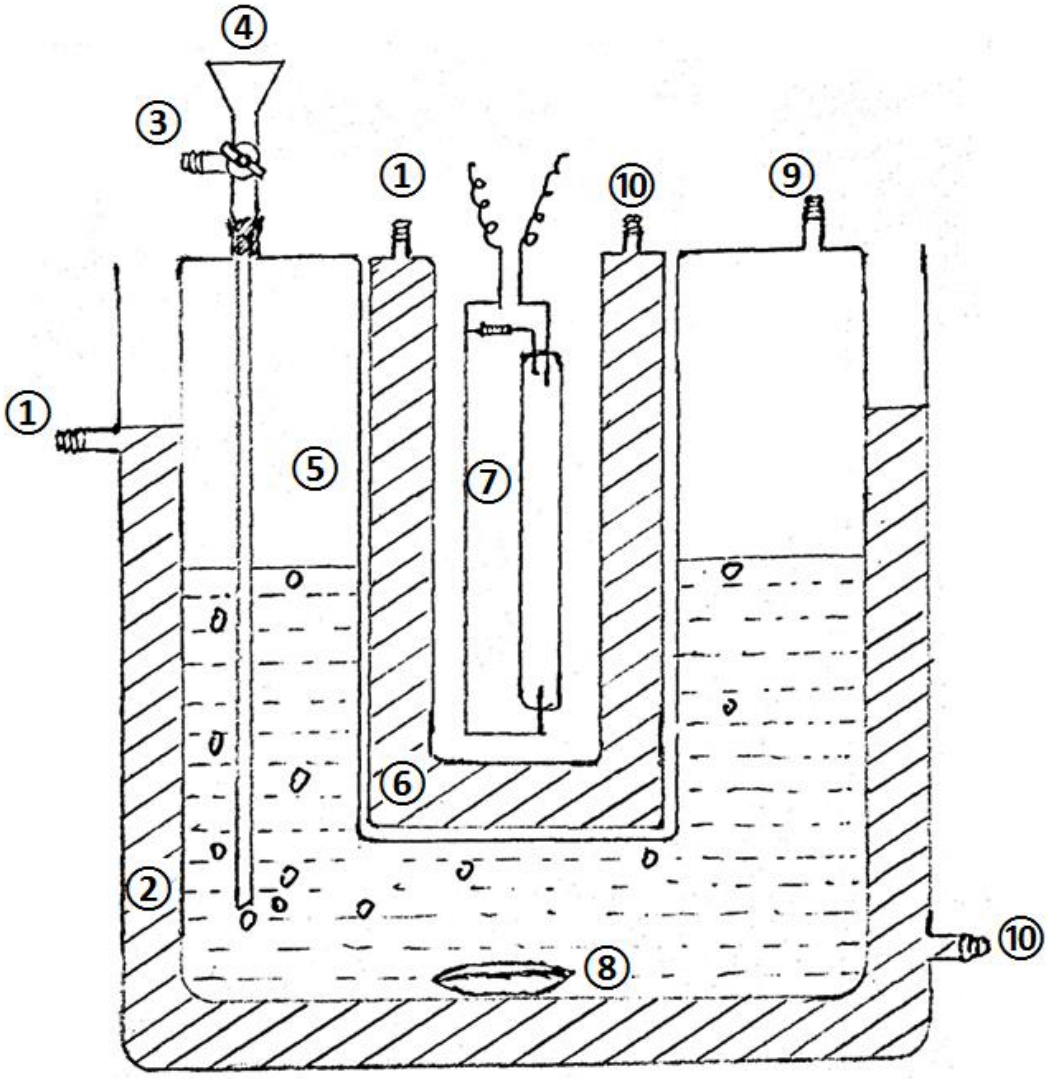

Figure A1 Design of the home-made photo reaction system. 1) Cooling water outlet , 2) Cooling water bath A, 3) Gas inlet, 4) Materials inlet, 5) Reaction chamber, 6) Cooling water bath B, 7) Mercury Vapor Lamp, 8) Magnetic stir bar, 9) Gas and material outlet, 10) Cooling water inlet.

Synthesis

In the first step, the Heck reaction of 4-bromostyrene **5** (1.65 mL, 12.6 mmol) with 2-bromo-6-mothoxynaphthalene **6** (2.0 g, 8.4 mmol) in the presence of sodium acetate (0.72g, 8.5mmol) and Hermann's catalyst (0.75mg, 2%) in *N*,*N*-dimethylacetamide (20 mL) produced diarylethene **7** with yield of ~30%. **7** was then irradiated with the 175W high-pressure mercury lamp on a 70~90 mg scale in cyclohexane, to give 2-bromo-10-methoxybenzo[*c*]phenanthrene **8** in ~50% yield.

The Heck coupling of benzo[c]phenanthrene derivative **8** (~250 mg, 0.75 mmol) with 3-bromostyrene **9** (1.5 equiv) and 2% (14 mg) Hermann's catalyst produced the coupled product **10** (45% yield). About 15 mg of **10** was irradiated in cyclohexane for about 90 min with yield of **11** at ~60%. Crude product is purified via column chromatography and characterized by NMR and XRD crystallography.[164]

3. Results and Discussions

The yield of each step is low but comparable to the original work of Aloui *et al*. The as-synthesized product **11** (**3b14m**) is a light yellow-brown colored crystal with a rod-like shape. The NMR data of product **11** (**Figure A15**) agrees well with the reported data.[155] Unit cell parameters from the XRD experiment agree with the reported value (a = 10.4825 Å, b = 16.5510 Å, and c = 22.4485 Å compared to the reported a = 10.54(7) Å, b = 16.563(6) Å, and c = 22.525(7) Å). The crystallography information of **3b14m** from Cambridge Crystallographic Data Centre (CCDC)[165] shows an orthorhombic crystal structure (**Figure A2 A**). In the crystal each molecule and its enantiomer form a molecule pair with an inversion center (**Figure A2 B**).

This orthorhombic crystal structure is centrosymmetric and is therefore non-piezoelectric. Possible electric induced deformation of each helicene will be canceled out by its paired enantiomer with deformation in the opposite direction. While **3b14m** in crystal form is not likely to be piezoelectric, orderly oriented molecular monolayers on smooth surfaces would be intrinsically non-centrosymmetric and thus still deform in uniform response to applied electric field. The racemic mixtures could also be separated via chiral resolution processes.

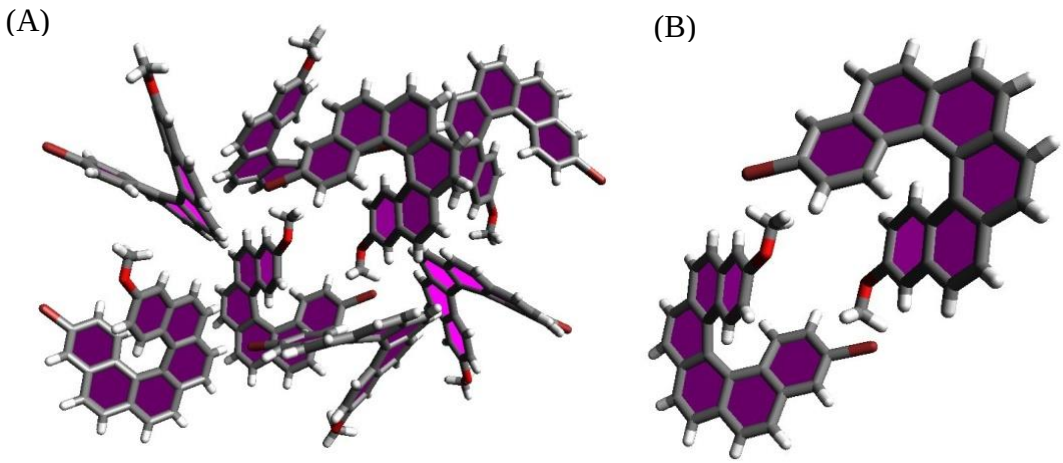

Figure A2 Crystal structure of 7 (3-bromo-14-methoxo[6]helicene) (A). Enantiomers form a centrosymmetric molecule pair in the crystal. Data is from the Cambridge Crystallographic Data Centre (CCDC).

4. Future Directions

According to our computational studies in **Chapter 2**, the combination of a stronger electron donating group and a stronger electron withdrawing group are likely to yield a larger piezoelectric coefficient. The pair of amino- and nitro- substituents, for example, show the highest d_{33} of 48.8 pm/V for all substituted helicenes tested.[76] If the bromide group of **3b14m** is substituted with the stronger electron withdrawing group -NO_2, the calculated d_{33} will increase from 19.3 pm/V to over 38.1 pm/V. Such substituents effect could provide a large pool of single molecule piezoelectric candidates.

Future directions related to helicene synthesis include the following aspects to: 1) synthesize multiple helicenes with other substituents to provide molecules with different levels of piezoelectric coefficient; 2) fabricate (patterned) SAMs of helicenes; 3) perform PFM measurements on the SAMs to test and verify the agreement between computational and experimental studies; and 4) identify molecules with the best piezoelectric performance and make helicene based piezoelectric devices.

So far, there has been no reported study on the synthesis of amino- and nitro- substituted helicenes. Here we propose a synthetic route to amino- and/or nitro- substituted helicenes starting from **3b14m** (**Scheme A3**). The first step is a transform the bromohelicene **11** to aminohelicne **12** via a sodium amide treatment in liquid ammonia.[166] Nitrohelicene could be achieved through amine oxidation using pertrifluoroacetic acid (CF_3CO_3H).[167]

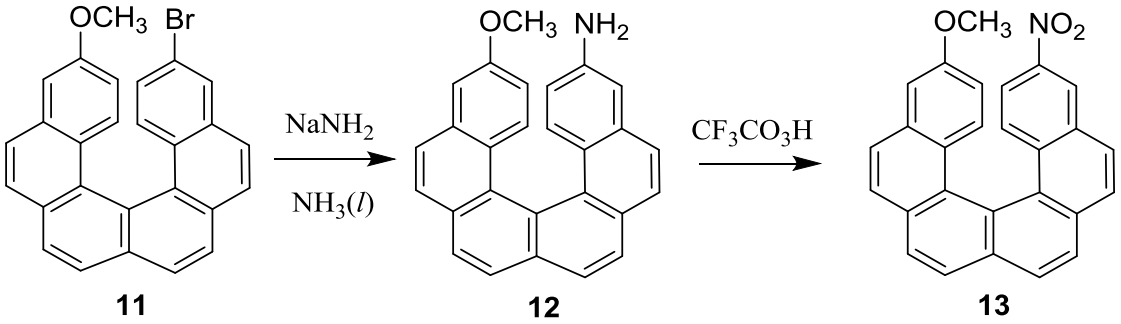

Scheme A3. Proposed synthetic route from aryl bromide to nitrobenzene.

APPENDIX B

FLEXIBLE MOLECULAR PIEZOELECTRIC DEVICE

Chapter 3 details the experimental demonstration of the converse piezoelectric effect of oligoaminoacids, namely the electric field induced shape change. The experimental demonstration of direct piezoelectric effect, strain induced electricity, has been attempted. Respectively, CA_6 and A_6C were deposited onto two separate flexible gold electrodes. The two electrodes were then faced to each other with a layer of PDMS spacer in between. The close circuit current was then measured with the employment of a controllable pressure against the two electrodes.

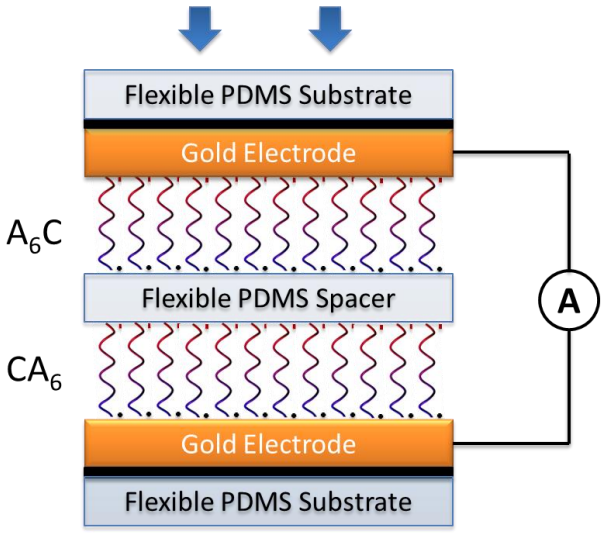

Figure A3 Flexible molecular piezoelectric testing device based on CA_6 and A_6C. Note that the polarization of the CA_6 layer and the A_6C layer are in the same direction.

Piezo generator fabrication

A ~5 mm thick polydimethylsiloxane (PDMS) substrate was achieved by mixing the two components of the epoxy adhesive thoroughly and annealing the mixture in an oven at 60°C for 1.5 hours. A 5 nm thick layer of Cr was deposited onto the flat surface of the PDMS substrate followed by a 200 nm thick Au layer deposition using an e-beam evaporator.

A gold substrate (pre-cut into 1 cm × 2 cm) was then immersed in CA_6 solution (1:1 acetonitrile/water) for hours to allow a compact layer of CA_6 to grow on the surface of the gold. The CA_6-loaded gold substrate was then rinsed with 1:1 acetonitrile/water and ethanol followed by a flow of nitrogen for drying. A separate substrate coated with a layer of A_6C was fabricated similarly. A piece of electric wire was soldered onto each gold electrode.

The PDMS spacer layer, as shown in **Figure A3**, was achieved by spin-coating a thin layer of the epoxy adhesive precursor mixture onto two as-prepared gold substrates (one with A_6C and one with CA_6). The two pieces were then faced against each other and annealed in an oven at 60°C for 1.5 hours.

Piezoelectric testing

The entire device was mounted onto a mechanical test system (MTI-1K, Measurements Technology Inc.). The displacement was set to 1 mm and the force applied to the device was recorded. The short circuit current was measured using a Keithley 2612 SYSTEM SourceMeter (Keithley Instruments, Inc.).

Results and discussion

Current at sub nanoampere was observed when a total strain of 10% was applied to and released from the device (**Figure A4**). A negative current pulse was generated upon the applied stress and a positive current pulse was detected when the stress was released. When the two electrodes were switched, however, an expected sign change of the current was not seen.

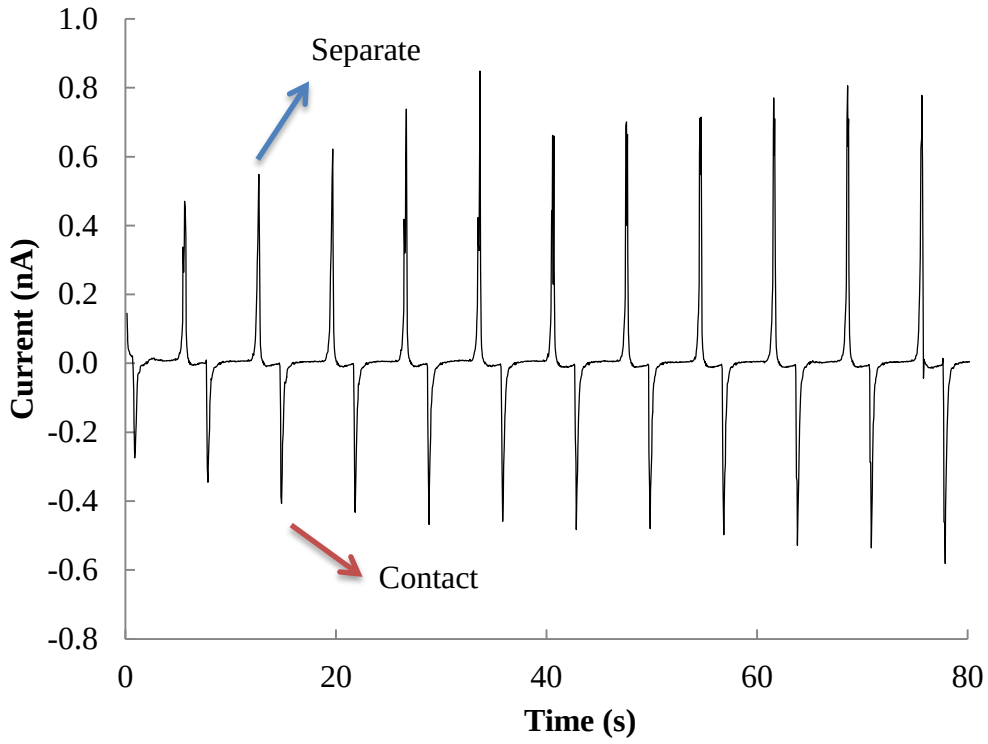

Figure A4 Typical curve of the short-circuit current under total stain of 10% of the piezo generator. Contact and separate correspond to a negative current pulse and a positive current pulse, respectively.

A control device was then fabricated with the same structure as shown in **Figure A3** but without the two oligoaminoacid layers. A similar current curve was still observed (**Figure A5**). The current observed from the control device may result from the contact electrification effect,[168] which has been demonstrated in similar structures reported as triboelectric nanogenerators.[169, 170] Electrostatic charges will redistribute between the PDMS film and the gold layer when contacted. A periodic contact and separation will then lead to a cycling positive and negative current peak.

The possible piezoelectric current due to the deformation of the oligoaminoacids may have been overwhelmed by the electrification current. Further investigations are needed to demonstrate the direct piezoelectric effect of oligoaminoacids CA_6 and A_6C.

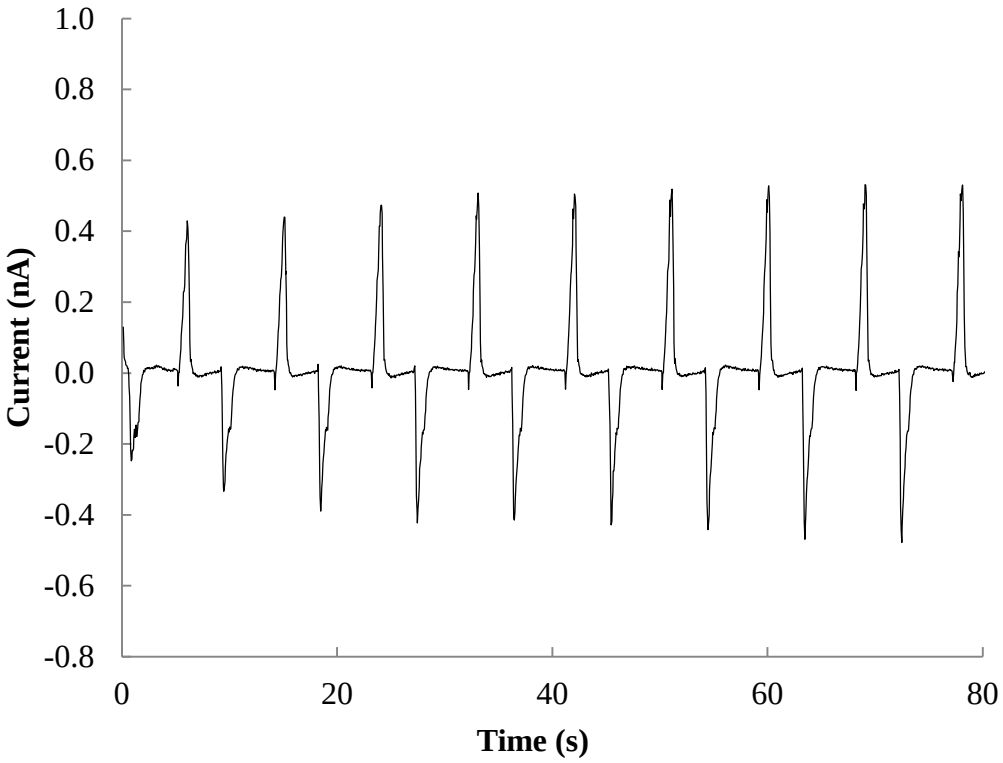

Figure A5 Typical short-circuit current curve under total stain of 10% of a control device without oligoaminoacid layers.

APPENDIX C

TABLES AND FIGURES

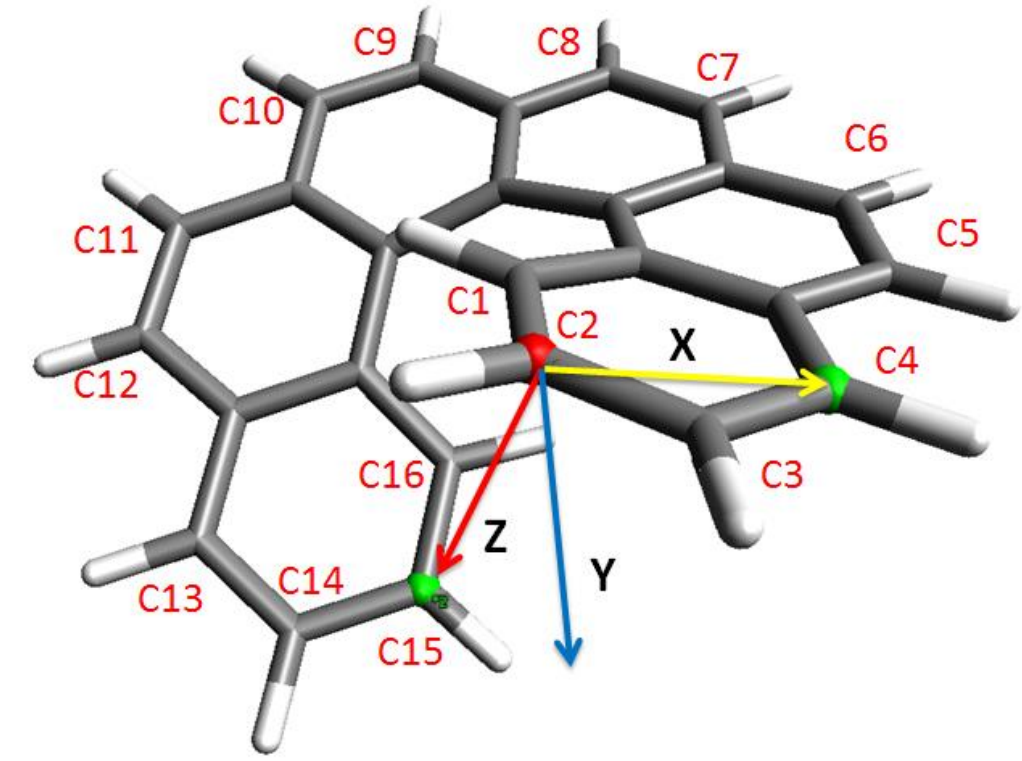

Figure A6 Internal coordinate of a helicene structure with numbering of atoms. The Z-axis is chosen to be along C2 to C15 and the X-axis is along C2 to C4. Y-axis is perpendicular to both x- and z-axis. Since the coordinates are defined only to assign the direction of the applied electric field, the angle between X- and Z- axis doesn't have to be exact 90˚. Electric field is applied to each of the thirteen directions defined in Table A1 and electric field along Z-axis provide the largest molecular deformation. Z-axis is then chosen as the default direction along which the field is applied for all the helicenes calculations.

Table A1 Thirteen directions chose in a three dimensional coordinates.

Directions	Notes
X (D1)	Along X-axis (y=0, z=0, $-\infty<x<+\infty$)
Y (D2)	Along Y-axis (x=0, z=0, $-\infty<y<+\infty$)
Z ((D3)	Along Z-axis (y=0, x=0, $-\infty<z<+\infty$)
X+Y (D4)	In plane X-Y, bisect of +X and +Y (z=0, x=y)
X-Y (D5)	In plane X-Y, bisect of +X and -Y (z=0, x=-y)
X-Z (D6)	In plane X-Z, bisect of +X and -Z (y=0, x=-z)
X+Z (D7)	In plane X-Z, bisect of +X and +Z (y=0, x=z)
Y-Z (D8)	In plane Y-Z, bisect of +Y and -Z (x=0, y=-z)
Y+Z (D9)	In plane Y-Z, bisect of +Y and +Z (x=0, y=z)
X+Y+Z (D10)	Bisect of +X, +Y and +Z (x=y=z)
X+Y-Z (D11)	Bisect of +X, +Y and -Z (x=y=-z)
X+Z-Y (D12)	Bisect of +X, -Y and +Z (x=-y=z)
X-Y-Z (D13)	Bisect of +X, -Y and -Z (x=-y=-z)

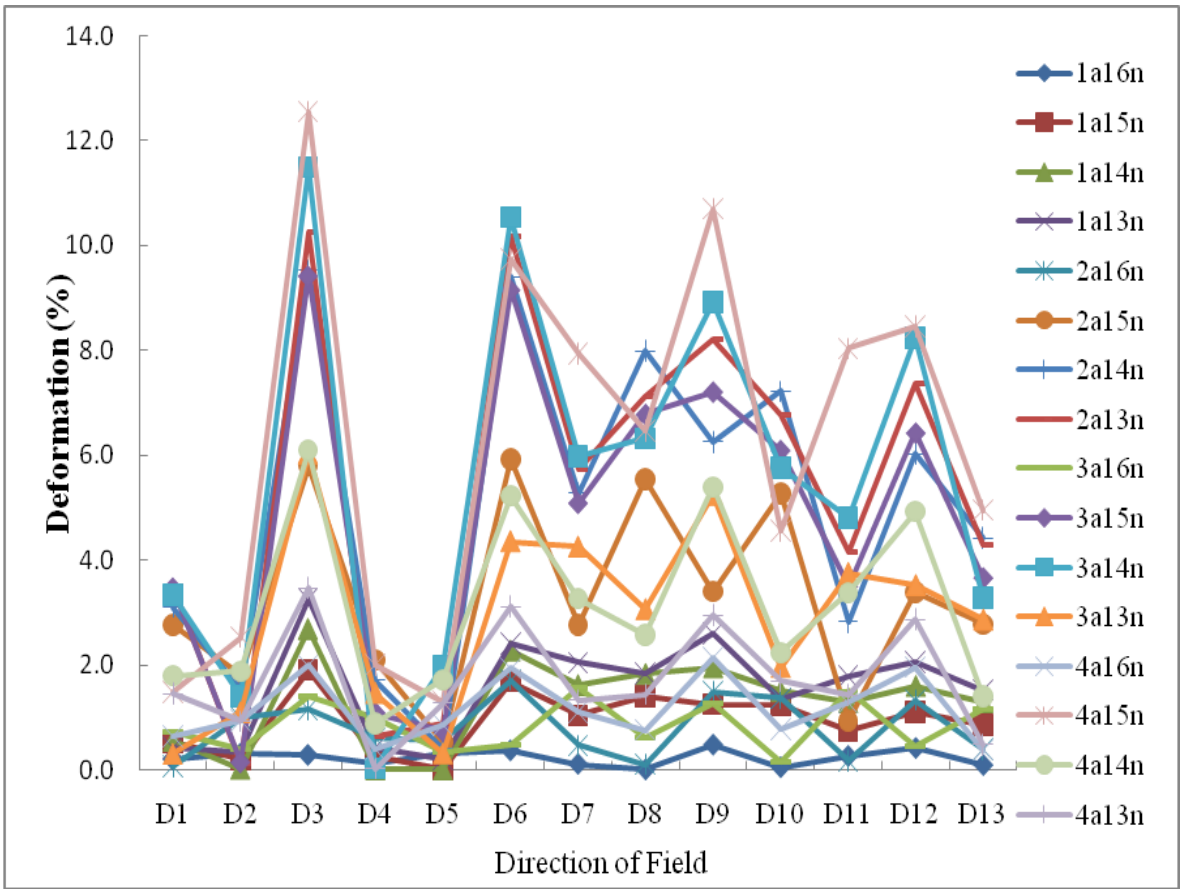

Figure A7 Deformation of all 16 amino- and nitro- substituted [6]helicene isomers along 13 different direction, as listed in **Table A1**. Field strength is within ±1.29 V/nm.

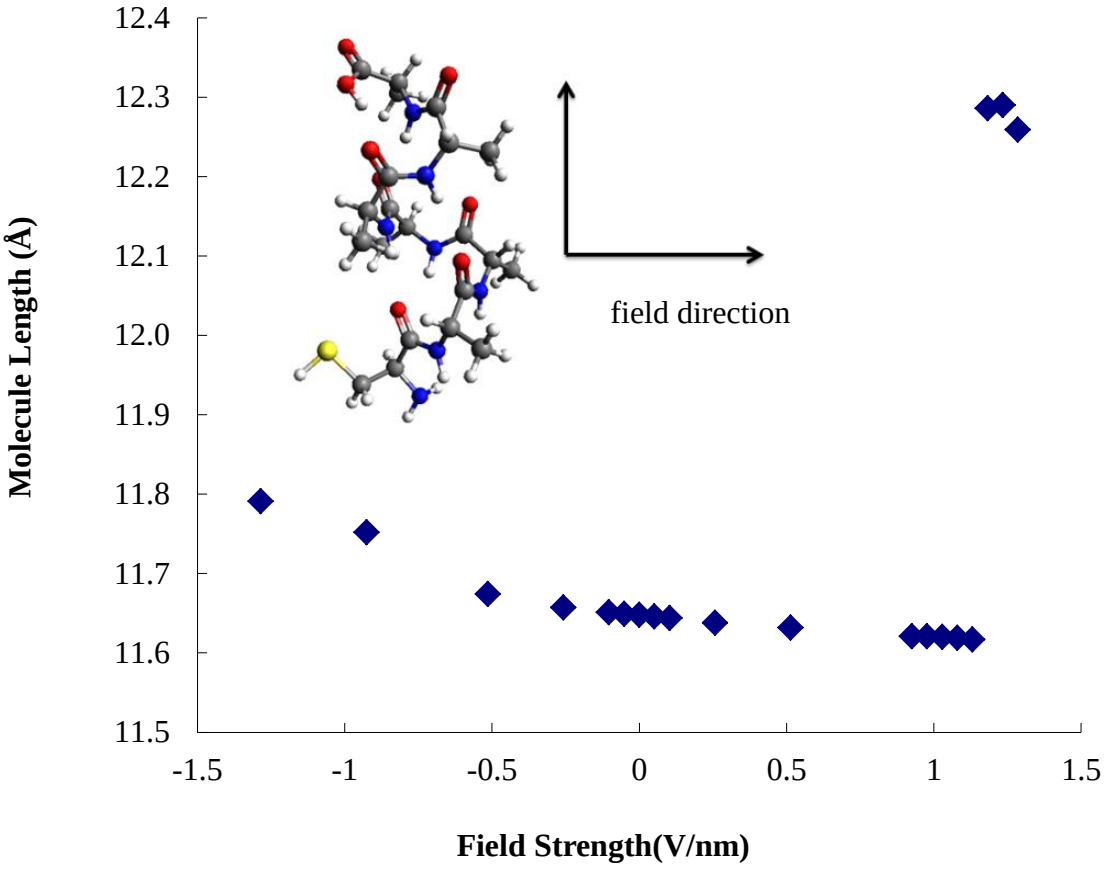

Figure A8 Calculated molecular length of CA_6 under different applied external electric fields. The field is applied perpendicular to the molecule helix. The calculated d_{31} over the range of (-0.26 to 0 pm/V) is 3.0 pm/V. α-helix to 3_{10}-helix transformation takes place at 1.18 pm/V.

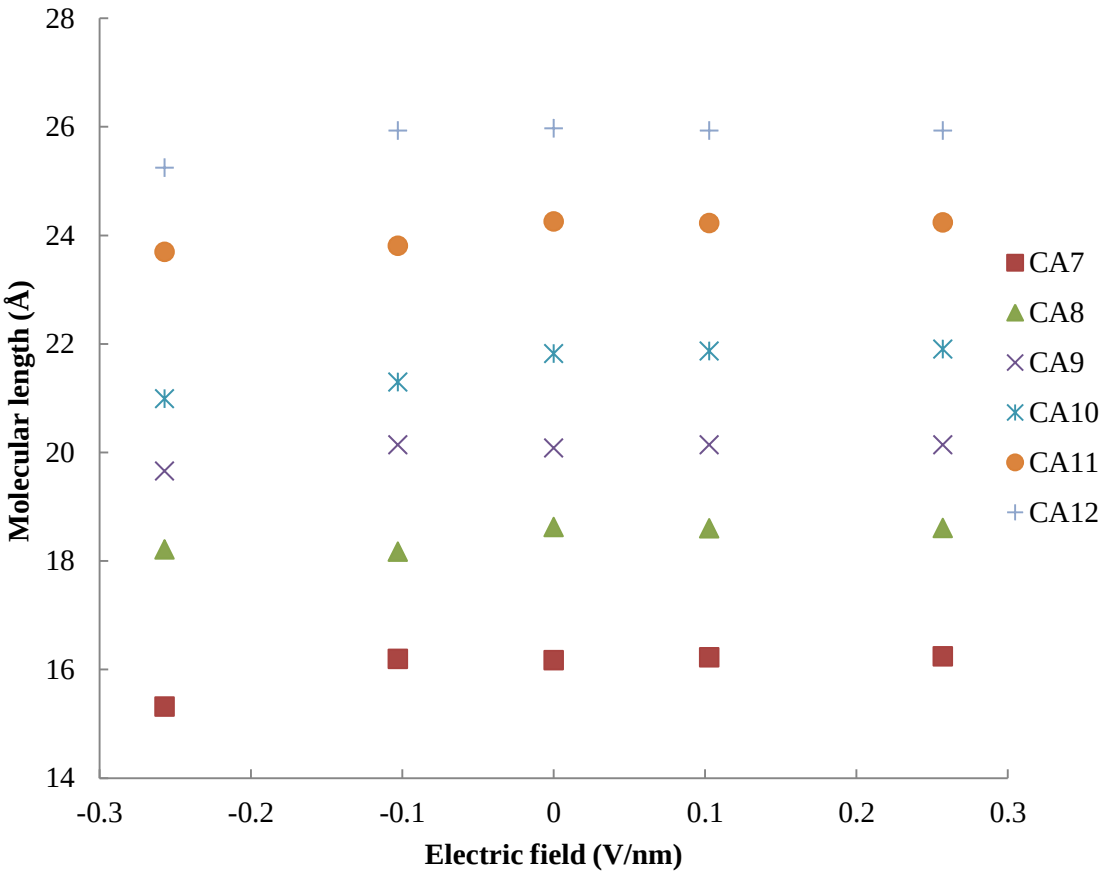

Figure A9 Calculated molecular length of CA_7 to CA_{12} over the field range of ±0.26 V/nm. Long molecules require longer computation time and some non-linearly are observed above CA_7.

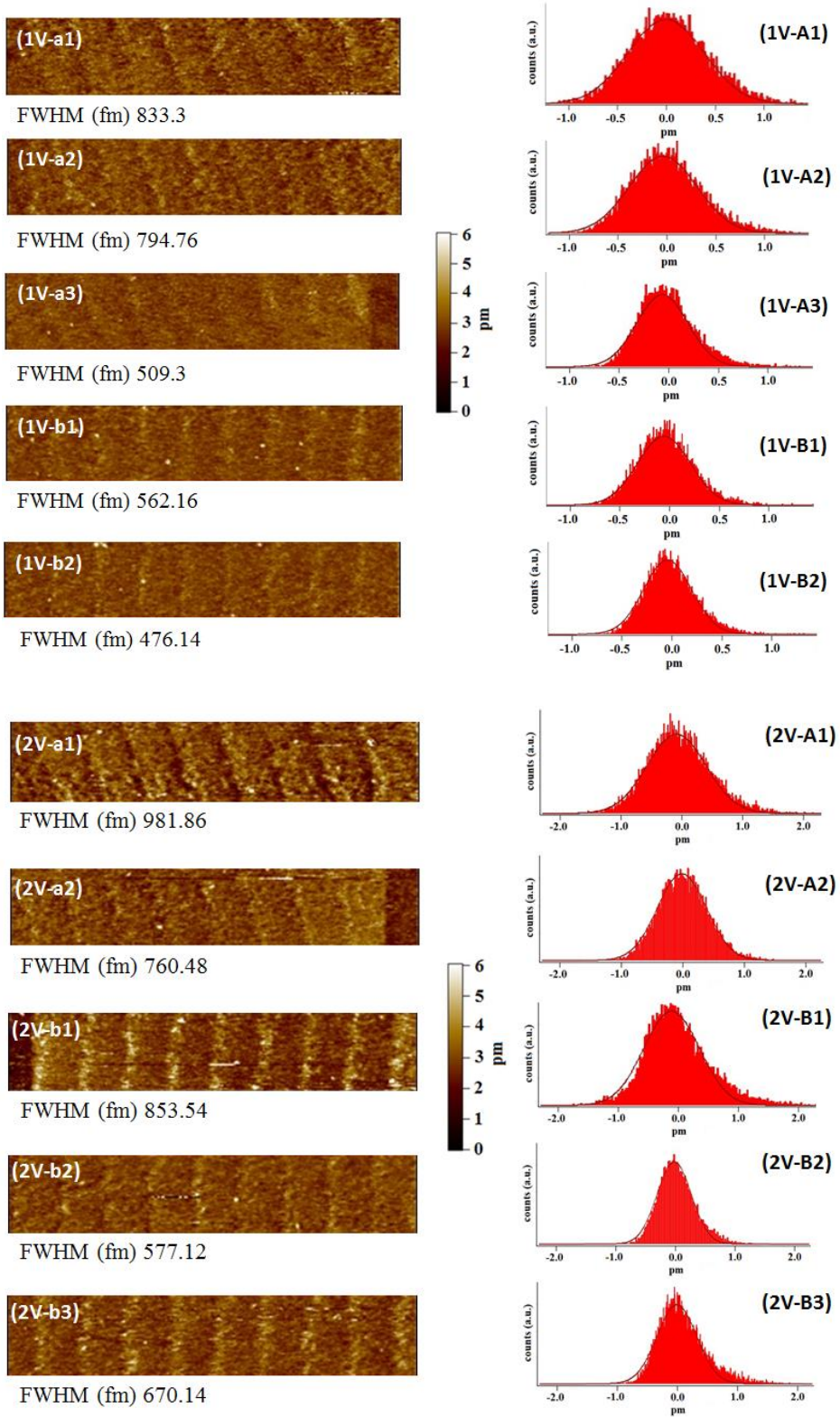
(1V-a1)
FWHM (fm) 833.3
(1V-a2)
FWHM (fm) 794.76
(1V-a3)
FWHM (fm) 509.3
(1V-b1)
FWHM (fm) 562.16
(1V-b2)
FWHM (fm) 476.14
(2V-a1)
FWHM (fm) 981.86
(2V-a2)
FWHM (fm) 760.48
(2V-b1)
FWHM (fm) 853.54
(2V-b2)
FWHM (fm) 577.12
(2V-b3)
FWHM (fm) 670.14
pm
counts (a.u.)
(1V-A1)
(1V-A2)
(1V-A3)
(1V-B1)
(1V-B2)
(2V-A1)
(2V-A2)
(2V-B1)
(2V-B2)
(2V-B3)

Cont'd

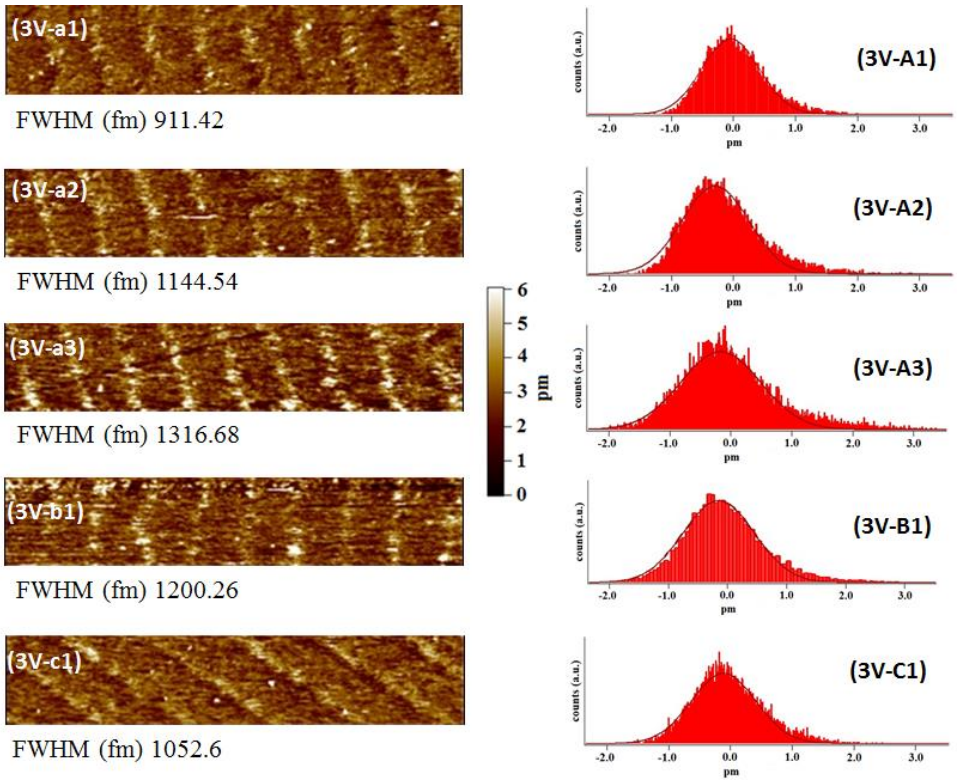

Figure A10 DART PFM amplitude images (left column) and amplitude histogram (right column) of CA_6. Data was taken from three samples a, b, and c. Each image was taken from a different location.

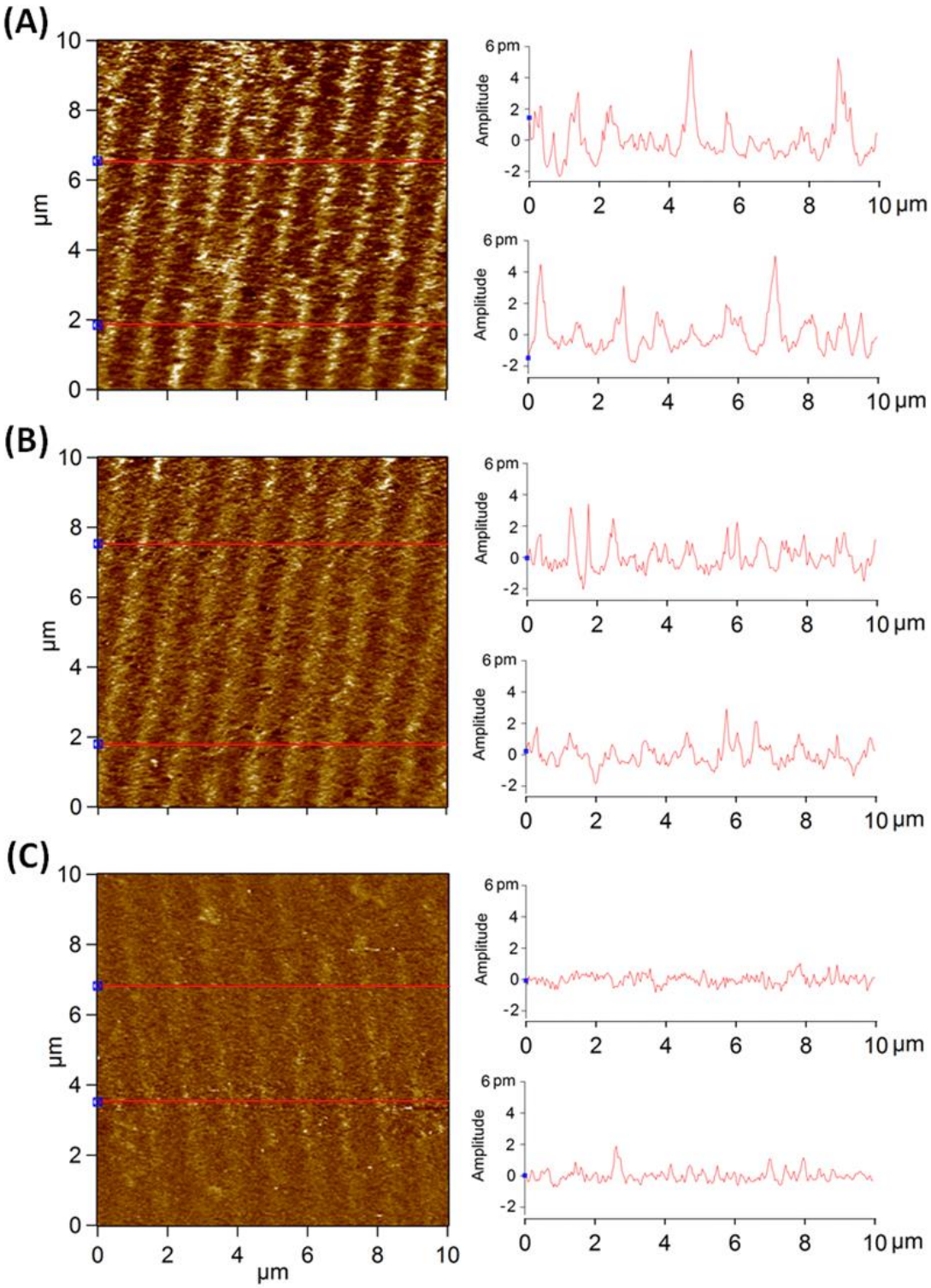

Figure A11 DART PFM amplitude images and section data of (A) CA_6, (B) A_6C, and (C) DT with an applied bias of 3 V.

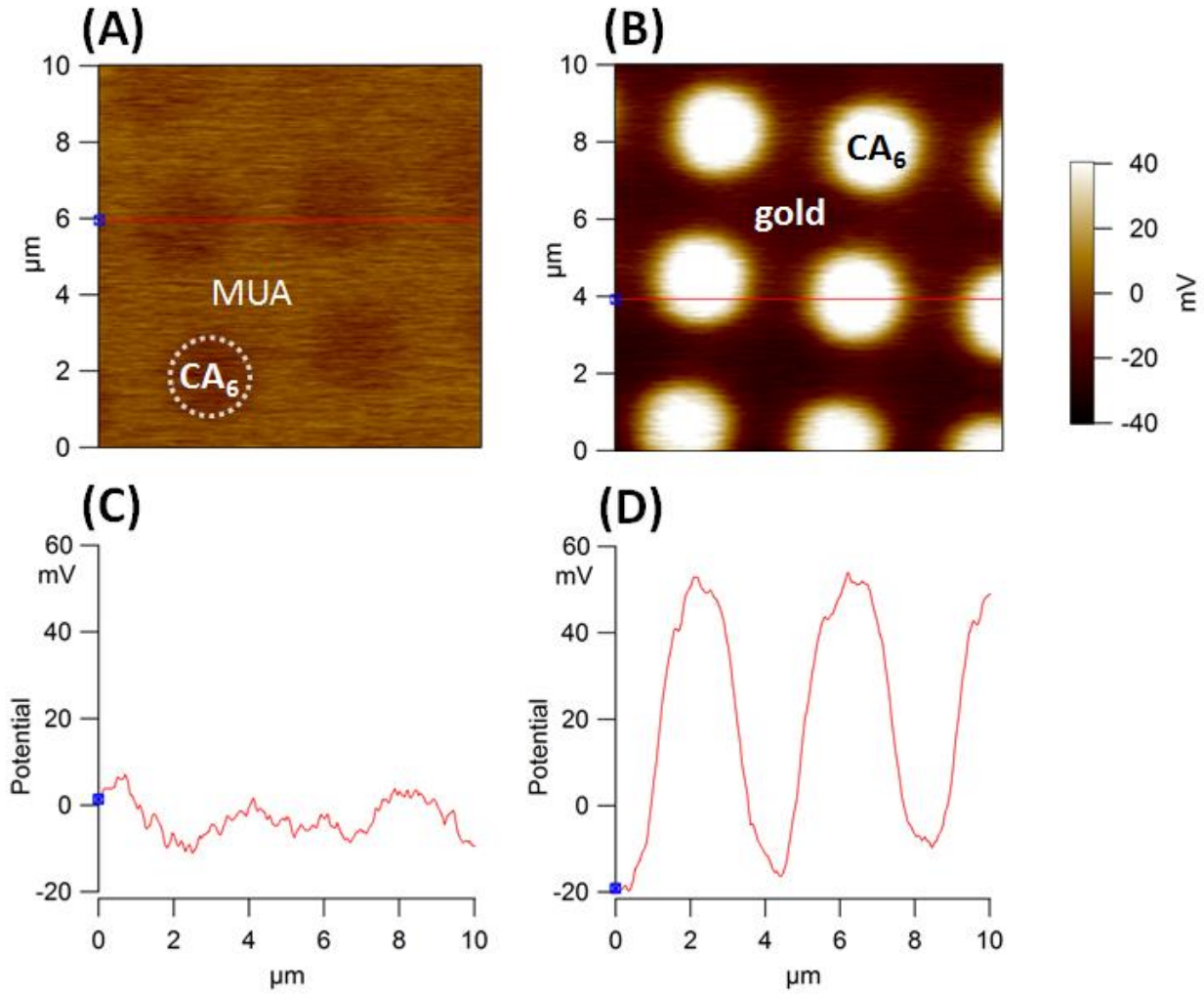

Figure A12 Surface potential images via Kelvin probe force microscopy (KPFM) of CA_6-MUA mixed SAMs (A and C) and CA_6 patterned SAMs (B and D). Potential difference between CA_6 and MUA (<20 mV) is significantly smaller than that between CA_6 and gold (>70 mV).

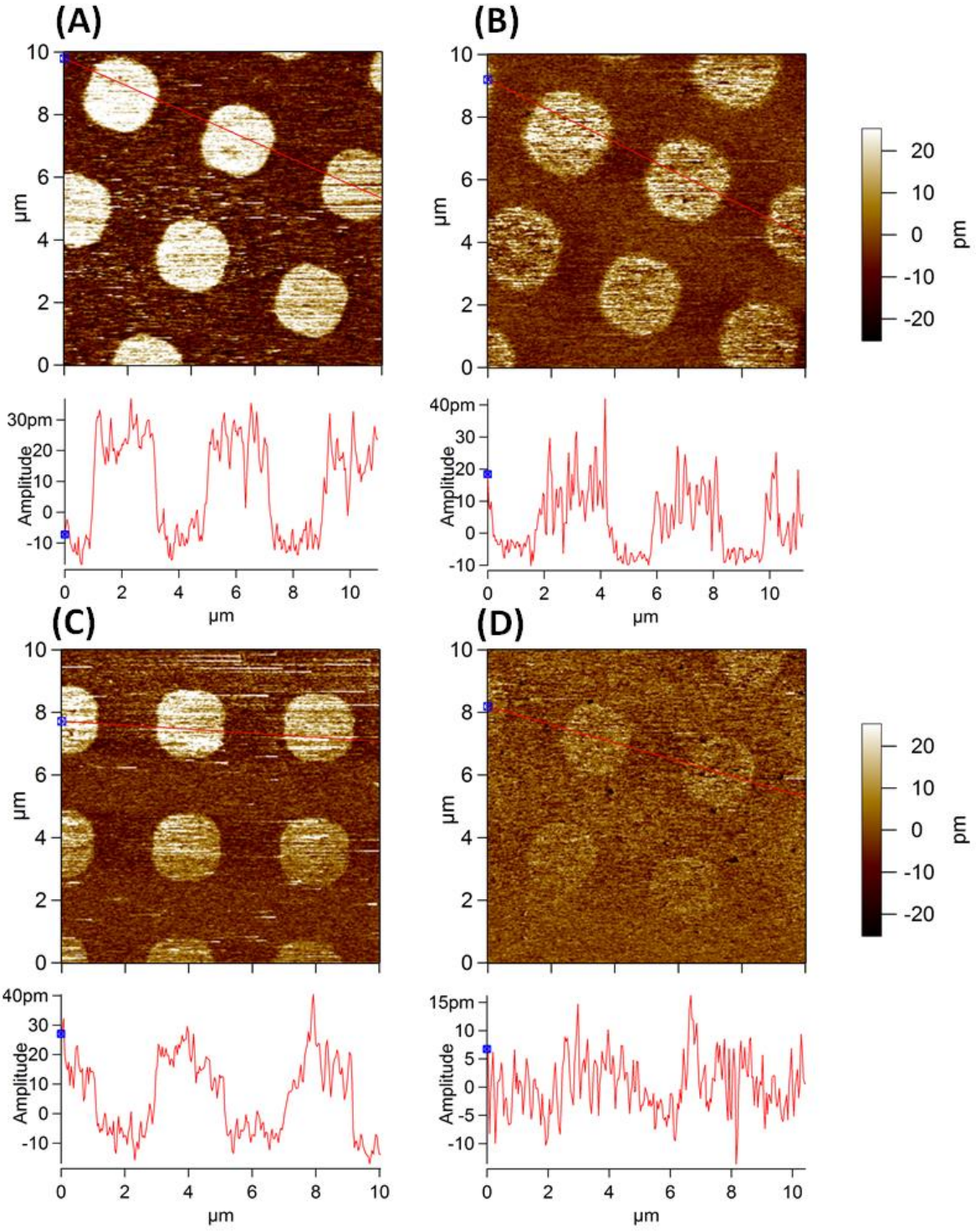

Figure A13 Single-frequency PFM amplitude images and section data of mixed CA_6 / MUA monolayers over time, from (A) as-prepared "0-day," (B) 8 days later, (C) 21 days later, to (D) 42 days later.

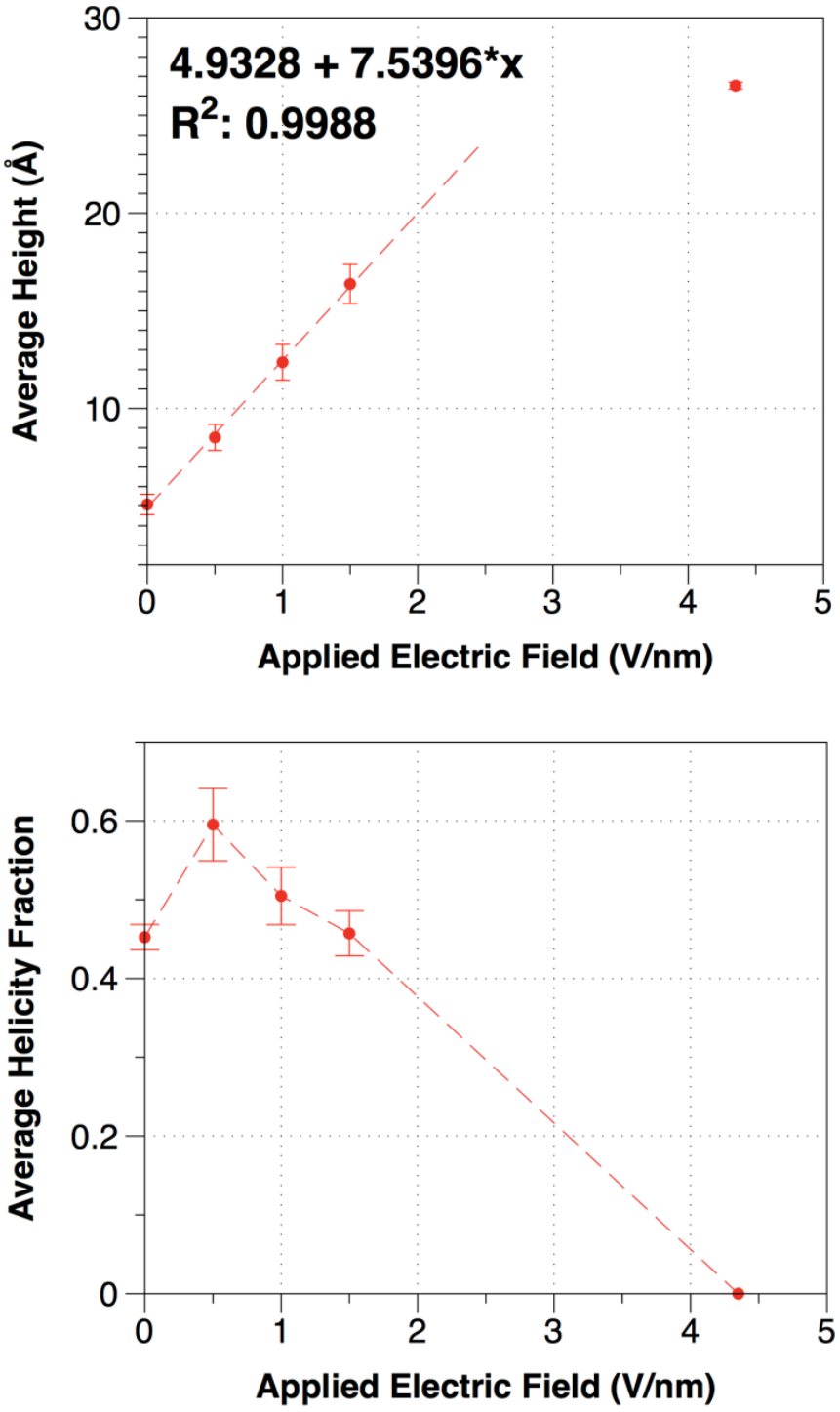

Figure A14 (top) Average computed "z" height between the peptide and the gold surface from MD runs, as a function of electric field. Note that the computed deformations are on the ~7-8Å scale, an order of magnitude larger than observed experimentally. This suggests that the large

change in conformation from random coil to helix to linear CA_6 observed in the MD runs is not observed experimentally. (bottom) Average fraction of helical residues in peptides (over 2000 frames), among those showing helical domains as a function of applied electric field.

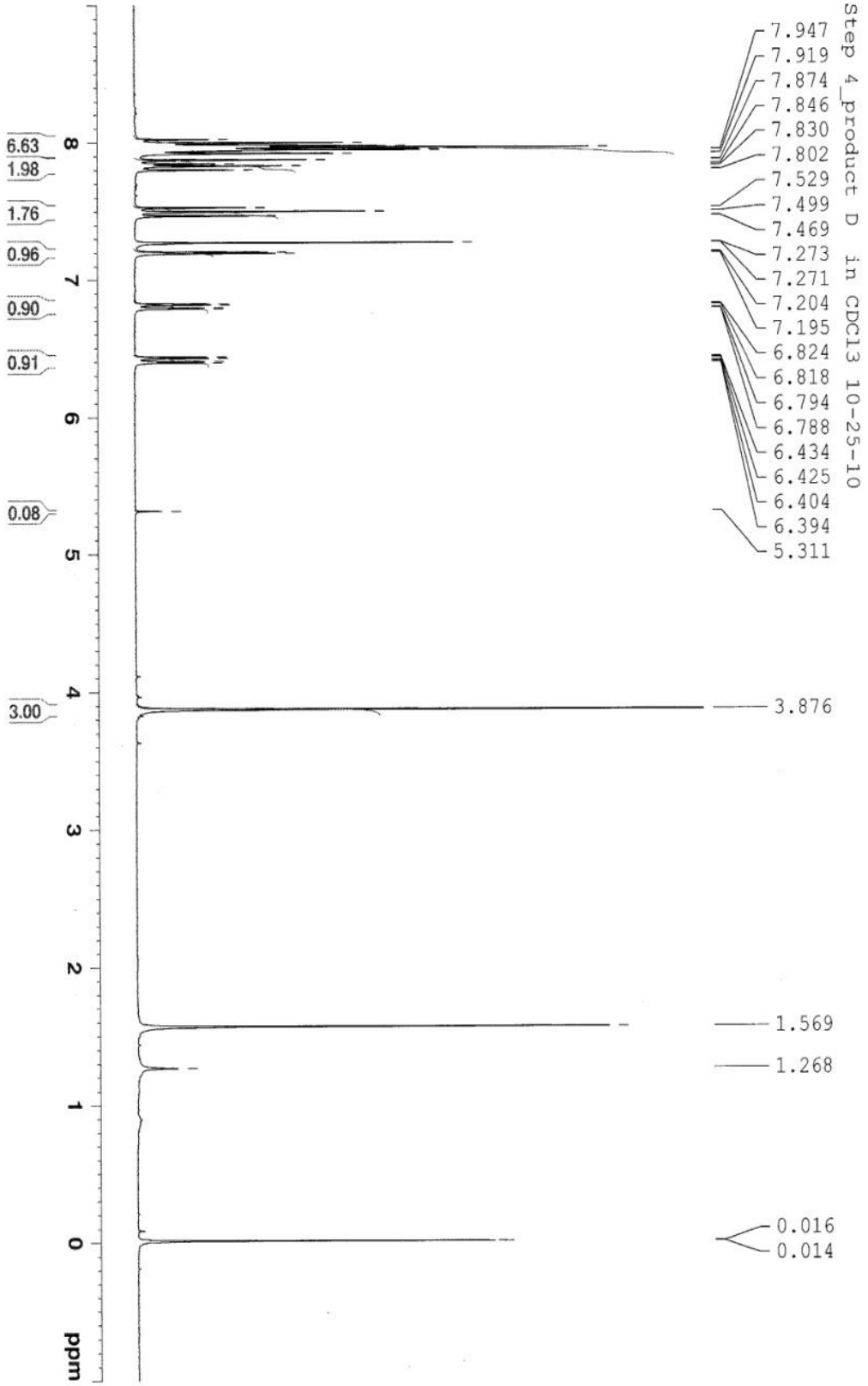
Step 4_product D in CDCl3 10-25-10
7.947
7.919
7.874
7.846
7.830
7.802
7.529
7.499
7.469
7.273
7.271
7.204
7.195
6.824
6.818
6.794
6.788
6.434
6.425
6.404
6.394
5.311
3.876
1.569
1.268
0.016
0.014
6.63
1.98
1.76
0.96
0.90
0.91
0.08
3.00
ppm

Cont'd

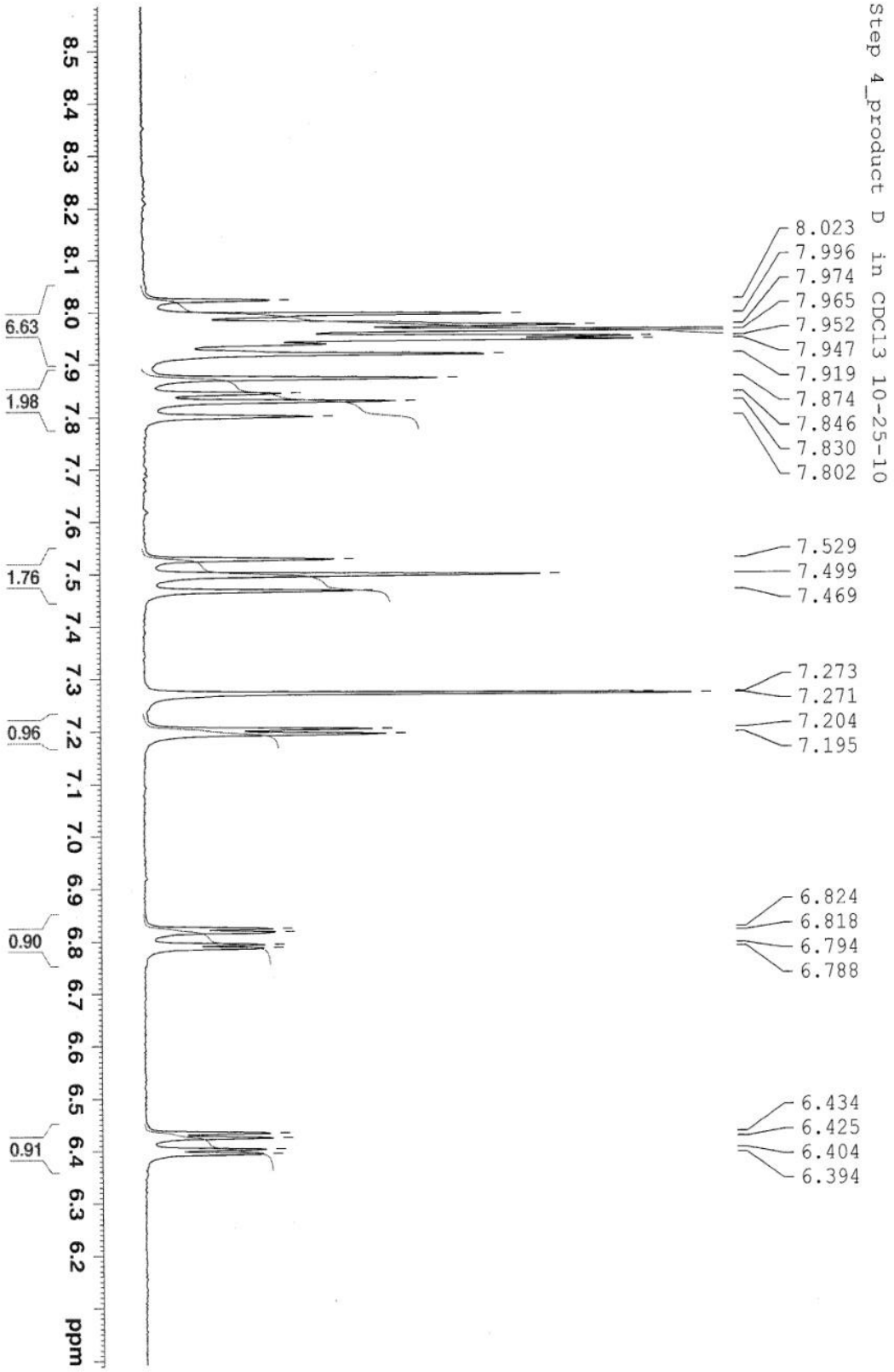

Figure A15 NMR data in $DCCl_3$ of 3-bromo-14-methoxo[6]helicene (**3b14m**).

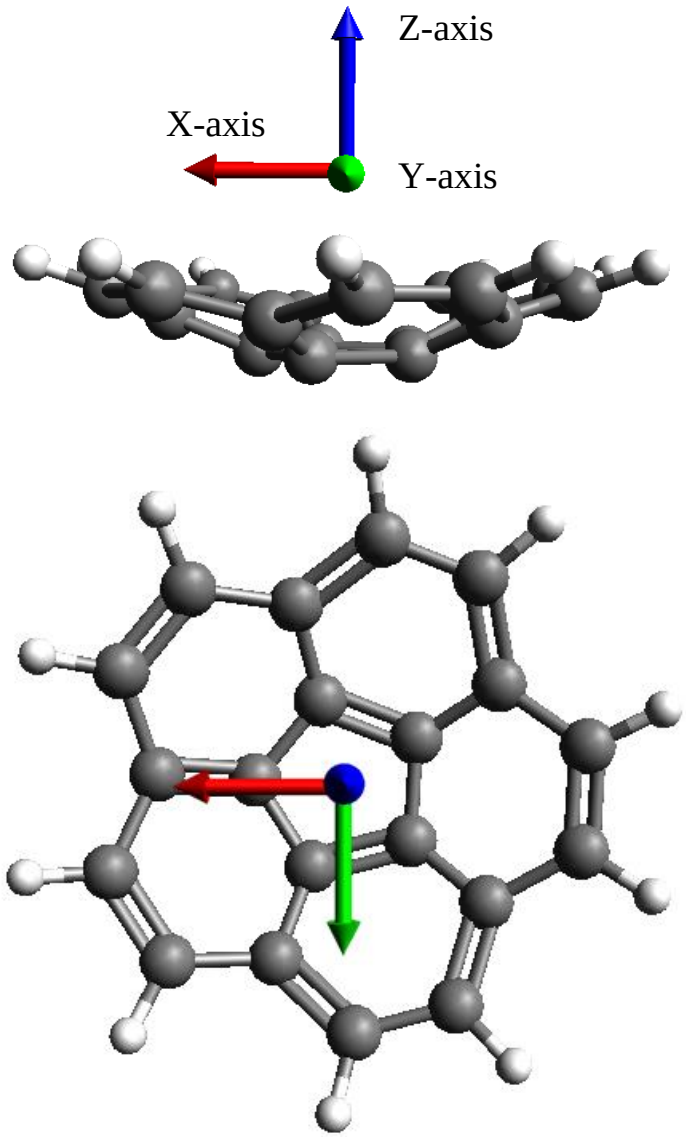

Figure A16 Internal coordinate of buckybowls using corannulene as an example. The Z-axis is chosen to point from the center of the bowl bottom to the center of the bowl rim. X-axis and Y-axis are randomly assigned perpendicular to both each other and Z-axis. from hC2 to C15 and the X-axis is along C2 to C4. Y-axis is perpendicular to both x- and z-axis. Field is only applied along the Z-axis which is the direction of the molecule breathing mode.

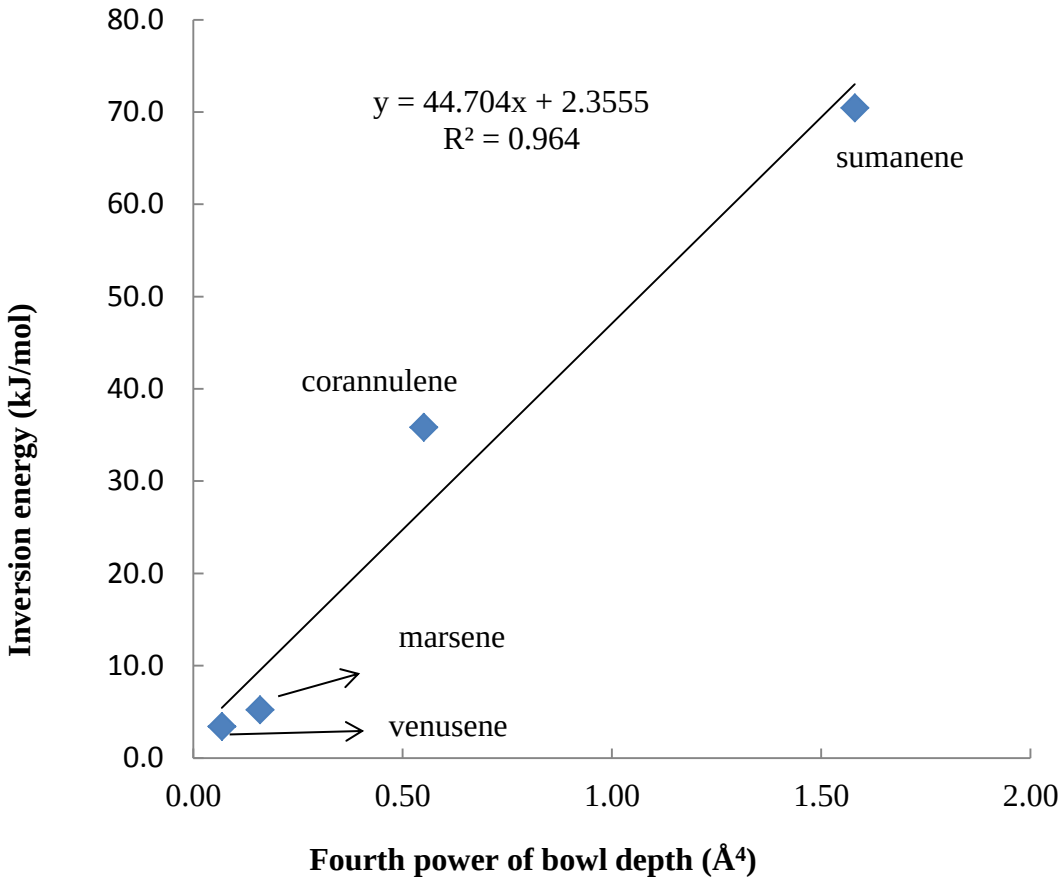

Figure A17 Structure – energy correlation of calculated inversion energy versus the fourth power of calculated bowl depth.

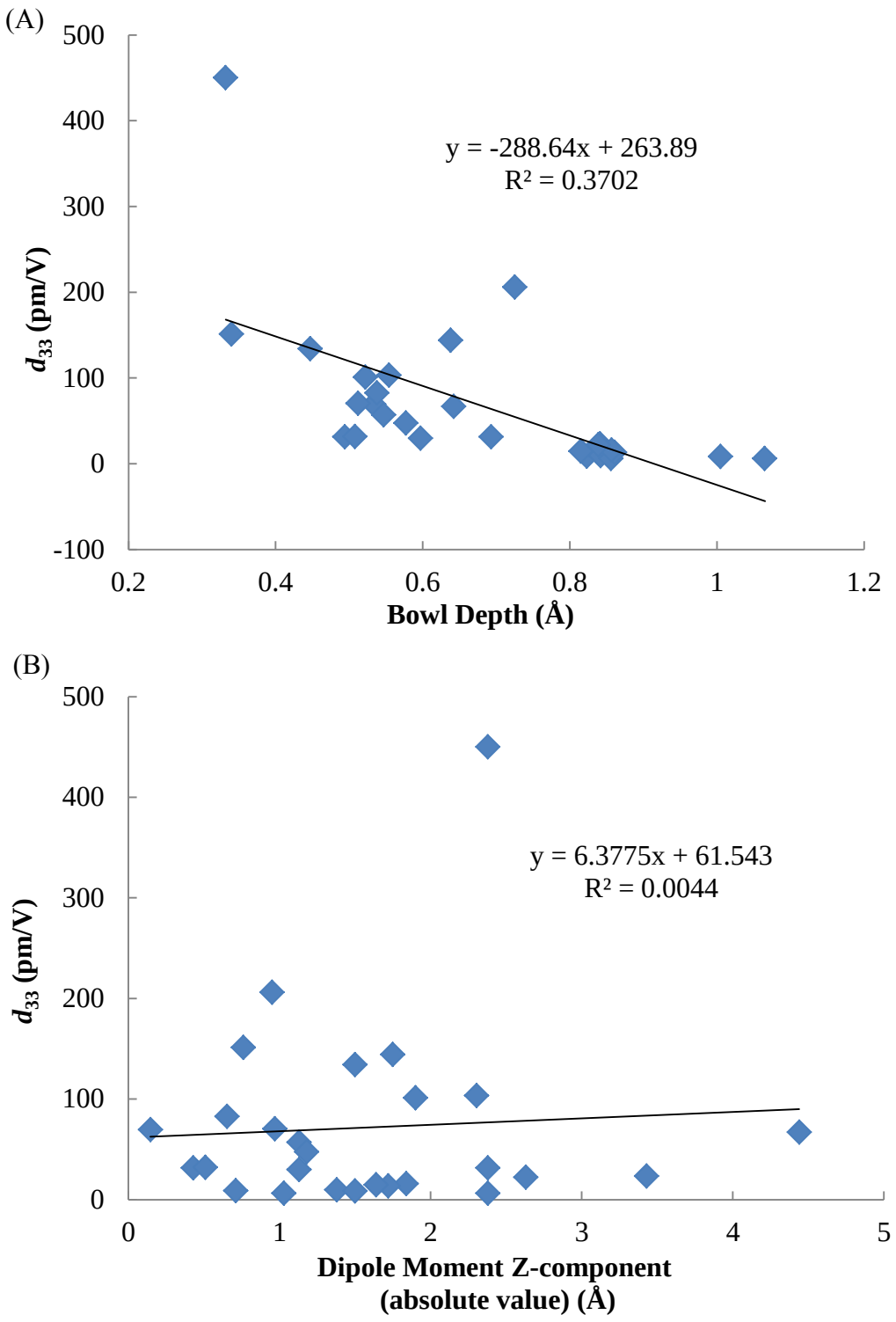

Figure A18 Correlation of calculated d_{33} to bowl depth (A) and dipole moment z-component in absolute value (B), respectively. The trend is not clear in both cases.

BIBLIOGRAPHY

1. Uchino, K., *Ferroelectric Devices*. Marcel Dekker: New York, 2000; p x, 308 p.

2. Nalwa, H. S., *Handbook of Low and High Dielectric Constant Materials and Their Applications*. Academic Press: San Diego, 1999.

3. Galassi, C., *Piezoelectric Materials : Advances in Science, Technology, and Applications*. Kluwer Academic Publishers: Dordrecht ; Boston, 2000; p xiii, 405 p.

4. Manalis, S. R.; Minne, S. C.; Quate, C. F. *Appl. Phys. Lett.* **1996,** 68, (6), 871-873.

5. Indermuhle, P. F.; Schurmann, G.; Racine, G. A.; deRooij, N. F. *J. Micromech. Microeng.* **1997,** 7, (3), 218-220.

6. Wang, Z. L.; Song, J. H. *Science* **2006,** 312, (5771), 242-246.

7. Carretero-Genevrier, A.; Gich, M.; Picas, L.; Gazquez, J.; Drisko, G. L.; Boissiere, C.; Grosso, D.; Rodriguez-Carvajal, J.; Sanchez, C. *Science* **2013,** 340, (6134), 827-831.

8. Shirane, G.; Hoshino, S.; Suzuki, K. *Phys. Rev.* **1950,** 80, (6), 1105-1106.

9. Zhao, M. H.; Wang, Z. L.; Mao, S. X. *Nano Lett.* **2004,** 4, (4), 587-590.

10. Fukada, E.; Takashit.S. *Jpn. J. Appl. Phys.* **1969,** 8, (7), 960-&.

11. Fukada, E. *Biorheology* **1995,** 32, (6), 593-609.

12. Kryszewski, M. *Acta Phys. Pol. A* **2004,** 105, (4), 389-408.

13. Horiuchi, S.; Tokura, Y. *Nat. Mater.* **2008,** 7, (5), 357-366.

14. Birkholz, M. *Z. Phys. B Con. Mat.* **1995,** 96, (3), 325-332.

15. Nye, J. F., *Physical Properties of Cristals: Their Representation by Tensors and Matrices*. Oxford University Press, Incorporated: 1985.

16. Takahashi, Y.; Ukishima, S.; Iijima, M.; Fukada, E. *J. Appl. Phys.* **1991,** 70, (11), 6983-6987.

17. Ochiai, T.; Fukada, E. *Jpn. J. Appl. Phys. Part 1* **1998,** 37, (6A), 3374-3376.

18. Hattori, T.; Takahashi, Y.; Iijima, M.; Fukada, E. *Jpn. J. Appl. Phys. Part 1* **1996,** 35, (11), 5763-5764.

19. Fukada, E., *Piezoelectricity and Pyroelectricity of Biopolymers*. Marcel Dekker INC: New York, 1995; Vol. 28, p 393.

20. Fukada, E.; Yasuda, I. *Jpn. J. Appl. Phys.* **1964,** 3, 117-121.

21. Kholkin, A.; Amdursky, N.; Bdikin, I.; Gazit, E.; Rosenman, G. *Acs Nano* **2010,** 4, (2), 610-614.

22. Lee, B. Y.; Zhang, J.; Zueger, C.; Chung, W. J.; Yoo, S. Y.; Wang, E.; Meyer, J.; Ramesh, R.; Lee, S. W. *Nat. Nanotechnol.* **2012,** 7, (6), 351-6.

23. Broadhurst, M. G.; Davis, G. T. *Ferroelectrics* **1984,** 60, (1), 3-13.

24. Nakhmanson, S. M.; Nardelli, M. B.; Bernholc, *J. Phys. Rev. B* **2005,** 72, (11).

25. Broadhurst, M. G.; Davis, G. T.; McKinney, J. E.; Collins, R. E. *J. Appl. Phys.* **1978,** 49, (10), 4992-4997.

26. Tasaka, S.; Miyata, S. *J. Appl. Phys.* **1985,** 57, (3), 906-910.

27. Fu, D.-W.; Cai, H.-L.; Liu, Y.; Ye, Q.; Zhang, W.; Zhang, Y.; Chen, X.-Y.; Giovannetti, G.; Capone, M.; Li, J.; Xiong, R.-G. *Science* **2013,** 339, (6118), 425-428.

28. Werling, K. A.; Hutchison, G. R.; Lambrecht, D. S. *J. Phys. Chem. Lett.* **2013,** 4, (9), 1365-1370.

29. Paturle, A.; Graafsma, H.; Sheu, H. S.; Coppens, P.; Becker, P. *Phys. Rev. B* **1991,** 43, (18), 14683-14691.

30. Horiuchi, S.; Tokunaga, Y.; Giovannetti, G.; Picozzi, S.; Itoh, H.; Shimano, R.; Kumai, R.; Tokura, Y. *Nature* **2010,** 463, (7282), 789-792.

31. Lipscomb, G. F.; Garito, A. F.; Narang, R. S. *J. Chem. Phys.* **1981,** 75, (3), 1509-1516.

32. Scott, J. F. *Science* **2007,** 315, (5814), 954-959.

33. Hwang, S. K.; Bae, I.; Cho, S. M.; Kim, R. H.; Jung, H. J.; Park, C. *Adv. Funct. Mater.* **2013**, 23, (44), 5484-5493.

34. Eerenstein, W.; Mathur, N. D.; Scott, J. F. *Nature* **2006,** 442, (7104), 759-765.

35. Furukawa, T. *Phase Transit.* **1989,** 18, (3-4), 143-211.

36. Bastani, Y.; Schmitz-Kempen, T.; Roelofs, A.; Bassiri-Gharb, N. *J. Appl. Phys.* **2011,** 109, (1), 014115-8.

37. Kim, D. M.; Eom, C. B.; Nagarajan, V.; Ouyang, J.; Ramesh, R.; Vaithyanathan, V.; Schlom, D. G. *Appl. Phys. Lett.* **2006,** 88, (14), 142904-3.

38. de la Cruz, J. P.; Joanni, E.; Vilarinho, P. M.; Kholkin, A. L. *J. Appl. Phys.* **2010,** 108, (11), 114106-8.

39. Nagarajan, V.; Junquera, J.; He, J. Q.; Jia, C. L.; Waser, R.; Lee, K.; Kim, Y. K.; Baik, S.; Zhao, T.; Ramesh, R.; Ghosez, P.; Rabe, K. M. *J. Appl. Phys.* **2006,** 100, (5).

40. Dunn, S. *Integr. Ferroelectr.* **2003,** 59, (1), 1505-1512.

41. Roelofs, A.; Schneller, T.; Szot, K.; Waser, R. *Nanotechnology* **2003,** 14, (2), 250.

42. Ichinose, N.; Udagawa, K. *Ferroelectrics* **1995,** 169, (1), 317-325.

43. Saito, Y.; Takao, H.; Tani, T.; Nonoyama, T.; Takatori, K.; Homma, T.; Nagaya, T.; Nakamura, M. *Nature* **2004,** 432, (7013), 84-7.

44. Shrout, T.; Zhang, S. *J. Electroceram.* **2007,** 19, (1), 113-126.

45. Takenaka, T.; Nagata, H. *J. Eur. Ceram. Soc.* **2005,** 25, (12), 2693-2700.

46. Lee, S.; Bae, S.-H.; Lin, L.; Yang, Y.; Park, C.; Kim, S.-W.; Cha, S. N.; Kim, H.; Park, Y. J.; Wang, Z. L. *Adv. Funct. Mater.* **2013,** 23, (19), 2445-2449.

47. Gu, L.; Cui, N. Y.; Cheng, L.; Xu, Q.; Bai, S.; Yuan, M. M.; Wu, W. W.; Liu, J. M.; Zhao, Y.; Ma, F.; Qin, Y.; Wang, Z. L. *Nano Lett.* **2013,** 13, (1), 91-94.

48. Lin, L.; Hu, Y. F.; Xu, C.; Zhang, Y.; Zhang, R.; Wen, X. N.; Wang, Z. L. *Nano Energy* **2013,** 2, (1), 75-81.

49. Wang, Z. L. *Adv. Mater.* **2012,** 24, (2), 280-285.

50. Pan, C. F.; Yu, R. M.; Niu, S. M.; Zhu, G.; Wang, Z. L. *Acs Nano* **2013,** 7, (2), 1803-1810.

51. Wu, W.; Wen, X.; Wang, Z. L. *Science* **2013,** 340, (6135), 952-957.

52. Yang, Y.; Guo, W.; Wang, X.; Wang, Z.; Qi, J.; Zhang, Y. *Nano Lett.* **2012,** 12, (4), 1919-1922.

53. Fan, Z.; Lu, J. G. *J. Nanosci. Nanotechnol.* **2005,** 5, (10), 1561-1573.

54. Chen, Y. Q.; Zheng, X. J.; Feng, X. *Nanotechnol.* **2010,** 21, (5), 055708.

55. Mohammadi, B.; Yousefi, A. A.; Bellah, S. M. *Polym. Test.* **2007,** 26, (1), 42-50.

56. Chen, S.; Li, X.; Yao, K.; Tay, F. E. H.; Kumar, A.; Zeng, K. *Polymer* **2012,** 53, (6), 1404-1408.

57. Blinov, L. M.; Fridkin, V. M.; Palto, S. P.; Sorokin, A. V.; Yudin, S. G. *Thin Solid Films* **1996,** 284, 474-476.

58. Biedermann, P. U.; Pogodin, S.; Agranat, I. *J. Org. Chem.* **1999,** 64, (10), 3655-3662.

59. Amaya, T.; Sakane, H.; Muneishi, T.; Hirao, T. *Chem. Commun.* **2008,** 0, (6), 765-767.

60. Seiders, T. J.; Baldridge, K. K.; Grube, G. H.; Siegel, J. S. *J. Am. Chem. Soc.* **2001,** 123, (4), 517-525.

61. Kanal, I. Y.; Owens, S. G.; Bechtel, J. S.; Hutchison, G. R. *J. Phys. Chem. Lett.* **2013,** 4, (10), 1613-1623.

62. Frisch, M. J.; Trucks, G. W.; Schlegel, H. B.; Scuseria, G. E.; Robb, M. A.; Cheeseman, J. R.; Scalmani, G.; Barone, V.; Mennucci, B.; Petersson, G. A. et al. Gaussian 09, Revision A.02, Gaussian, Inc. Wallingford, CT, USA, 2009

63. Becke, A. D. *J. Chem. Phys.* **1993,** 98, (7), 5648-5652.

64. Lee, C.; Yang, W.; Parr, R. G. *Phys. Rev. B* **1988,** 37, (2), 785.

65. Grimme, S.; Antony, J.; Ehrlich, S.; Krieg, H. *J. Chem. Phys.* **2010,** 132, (15), 154104.

66. Swart, M.; Sola, M.; Bickelhaupt, F. M. *J. Comp. Chem.* **2011,** 32, (6), 1117-1127.

67. Ehrlich, S.; Moellmann, J.; Grimme, S. *Acc. Chem. Res.* **2012**, 120615161936008.

68. Cai, Z.; Sendt, K.; Reimers, J. *J. Chem. Phys.* **2002,** 117, (12), 5543-5549.

69. Kohn, W.; Meir, Y.; Makarov, D. *Phys. Rev. Lett.* **1998,** 80, (19), 4153-4156.

70. Baer, R.; Neuhauser, D. *Phys. Rev. Lett.* **2005,** 94, (4), 043002.

71. Gritsenko, O.; Baerends, E. J. *J. Chem. Phys.* **2004,** 121, (2), 655-660.

72. Grimme, S. *J. Comput. Chem.* **2006,** 27, (15), 1787-99.

73. Yanai, T.; Tew, D. P.; Handy, N. C. *Chem. Phys. Lett.* **2004,** 393, (1-3), 51-57.

74. Adamo, C.; Barone, V. *J. Chem. Phys.* **1999,** 110, (13), 6158.

75. Chai, J. D.; Head-Gordon, M. *Phys. Chem. Chem. Phys.* **2008,** 10, (44), 6615-20.

76. Quan, X.; Marvin, C. W.; Seebald, L.; Hutchison, G. R. *J. Phys. Chem. C* **2013,** 117, (33), 16783-16790.

77. Werling, K. A.; Hutchison, G. R.; Lambrecht, D. S. *J. Phys. Chem. Lett.* **2013**, 1365-1370.

78. Hanwell, M. D.; Curtis, D. E.; Lonie, D. C.; Vandermeersch, T.; Zurek, E.; Hutchison, G. *J. Cheminf.* **2012,** 4, (1), 17.

79. Shao, Y.; Fusti-Molnar, L.; Jung, Y.; Kussmann, J.; Ochsenfeld, C.; Brown, S. T.; Gilbert, A. T. B.; Slipchenko, L. V.; Levchenko, S. V.; O'Neill, D. P.; et. al. *Phys. Chem. Chem. Phys*. 2006 8, 3172.

80. Hammett, L. P. *J. Am. Chem. Soc.* **1937,** 59, (1), 96-103.

81. Hansch, C.; Leo, A.; Taft, R. W. *Chem. Rev.* **1991,** 91, (2), 165-195.

82. Jarrold, M. F. *Annu. Rev. Phys. Chem.* **2000,** 51, (1), 179-207.

83. Furukawa, T.; Seo, N. *Jpn. J. Appl. Phys.* **1990,** 29, 675.

84. Kitagawa, K.; Morita, T.; Kimura, S. *Angew. Chem. Int. Ed.* **2005,** 44, (39), 6330-6333.

85. Fiori, W. R.; Miick, S. M.; Millhauser, G. L. *Biochemistry-Us* **1993,** 32, (45), 11957-11962.

86. Lahann, J.; Mitragotri, S.; Tran, T. N.; Kaido, H.; Sundaram, J.; Choi, I. S.; Hoffer, S.; Somorjai, G. A.; Langer, R. *Science* **2003,** 299, (5605), 371-374.

87. Birk, H.; Glatz-Reichenbach, J.; Jie, L.; Schreck, E.; Dransfeld, K. In *The local piezoelectric activity of thin polymer films observed by scanning tunneling microscopy*, 1991; AVS: 1991; pp 1162-1165.

88. Binnig, G.; Rohrer, H. *IBM J. Res. Dev.* **2000,** 44, (1-2), 279-293.

89. Guthner, P.; Dransfeld, K. *Appl. Phys. Lett.* **1992,** 61, (9), 1137-1139.

90. Eng, L.; Grafström, S.; Loppacher, C.; Schlaphof, F.; Trogisch, S.; Roelofs, A.; Waser, R., Three-Dimensional Electric Field Probing of Ferroelectrics on the Nanometer Scale Using

Scanning Force Microscopy. In *Advances in Solid State Physics*, Kramer, B., Ed. Springer Berlin / Heidelberg: 2001; Vol. 41, pp 287-298.

91. Alexe, M.; Gruverman, A., *Nanoscale Characterisation of Ferroelectric Materials : Scanning Probe Microscopy Approach*. Springer-Verlag: Berlin ; New York, 2004; p xiii, 282 p.

92. Hong, S., *Nanoscale Phenomena in Ferroelectric Thin Films*. Kluwer Academic Publishers: Boston, 2004; p xiv, 288 p.

93. Kalinin, S. V.; Rodriguez, B. J.; Jesse, S.; Karapetian, E.; Mirman, B.; Eliseev, E. A.; Morozovska, A. N. *Annu. Rev. Mater. Res.* **2007,** 37, (1), 189-238.

94. Nikiforov, M. P.; Thompson, G. L.; Reukov, V. V.; Jesse, S.; Guo, S.; Rodriguez, B. J.; Seal, K.; Vertegel, A. A.; Kalinin, S. V. *Acs Nano* **2010,** 4, (2), 689-698.

95. Hong, J. W.; Park, S. I.; Khim, Z. G. *Rev. Sci. Instrum.* **1999,** 70, (3), 1735-1739.

96. Jungk, T.; Hoffmann, A.; Soergel, E. *Appl. Phys. Lett.* **2006,** 89, (16).

97. Kalinin, S. V.; Bonnell, D. A. *Phys. Rev. B* **2002,** 65, (12), 125408.

98. Scrymgeour, D. A.; Gopalan, V. *Phys. Rev. B* **2005,** 72, (2).

99. Kalinin, S. V.; Gruverman, A., *Scanning Probe Microscopy : Electrical and Electromechanical Phenomena at the Nanoscale*. Springer: New York, 2007; p 2 v. (xx, 980 p., 8 p. of plates).

100. Jungk, T.; Hoffmann, A.; Soergel, E. *Appl. Phys. Lett.* **2007,** 91, (25), -.

101. Soergel, E. *J. Phys. D Appl. Phys.* **2011,** 44, (46).

102. Binnig, G.; Quate, C. F.; Gerber, C. *Phys. Rev. Lett.* **1986,** 56, (9), 930.

103. Muller, D. J.; Fotiadis, D.; Scheuring, S.; Muller, S. A.; Engel, A. *Biophys. J.* **1999,** 76, (2), 1101-1111.

104. Rodriguez, B. J.; et al. *Nanotechnol.* **2007,** 18, (47), 475504.

105. Gannepalli, A.; Yablon, D. G.; Tsou, A. H.; Proksch, R. *Nanotechnol.* **2011,** 22, (35), 355705.

106. Stephen, J.; Sergei, V. K.; Roger, P.; Baddorf, A. P.; Rodriguez, B. J. *Nanotechnol.* **2007,** 18, (43), 435503.

107. Susi, H.; Byler, D. M. *Method. Enzymol.* **1986,** 130, 290-311.

108. Byler, D. M.; Susi, H. *Biopolymers* **1986,** 25, (3), 469-487.

109. Goormaghtigh, E.; Cabiaux, V.; Ruysschaert, J. M. *Sub-cell. Biochem.* **1994,** 23, 405-50.

110. Jackson, M.; Mantsch, H. H. *Can. J. Chem.* **1991,** 69, (11), 1639-1642.

111. Abe, Y.; Krimm, S. *Biopolymers* **1972,** 11, (9), 1817-&.

112. Barth, A.; Zscherp, C. *Q. Rev. Biophys.* **2002,** 35, (4), 369-430.

113. Jackson, M.; Mantsch, H. H. *Crit. Rev. Biochem. Mol.* **1995,** 30, (2), 95-120.

114. Simon, A. Grazing angle microscope. US6008936 A, 1999.

115. Hegner, M.; Wagner, P.; Semenza, G. *Surf. Sci.* **1993,** 291, (1-2), 39-46.

116. Mrksich, M.; Whitesides, G. M. *Trends Biotechnol.* **1995,** 13, (6), 228-235.

117. Alexander, S.; Hellemans, L.; Marti, O.; Schneir, J.; Elings, V.; Hansma, P. K.; Longmire, M.; Gurley, J. *J. Appl. Phys.* **1989,** 65, (1), 164-167.

118. Kumar, A.; Whitesides, G. M. *Appl. Phys. Lett.* **1993,** 63, (14), 2002-2004.

119. Wilbur, J. L.; Biebuyck, H. A.; MacDonald, J. C.; Whitesides, G. M. *Langmuir* **1995,** 11, (3), 825-831.

120. Bernard, A.; Renault, J. P.; Michel, B.; Bosshard, H. R.; Delamarche, E. *Adv. Mater.* **2000,** 12, (14), 1067-1070.

121. Kathan-Galipeau, K.; Nanayakkara, S.; O'Brian, P. A.; Nikiforov, M.; Discher, B. M.; Bonnell, D. A. *Acs Nano* **2011,** 5, (6), 4835-42.

122. These three molucules with similar computed molecular lengths (CA6 1.50 nm, A6C 1.68 nm, and DT 1.91 nm) all form SAMs on gold but with different terminal (top) end group, e.g. -COOH/-COO- for CA6, -NH2 for A6C and -CH3 for DT.

123. Kozlowski L. 2007-2012 Isoelectric Point Calculator. http://isoelectric.ovh.org. The pKa of MUA (or CA6 or any surface-bound acid) depends both on the local ionic activity and measuring methods. pKa of MUA in solution is however ~4.8, e.g. [D. Wang et al., How and Why Nanoparticle's Curvature Regulates the Apparent pKa of the Coating Ligands. *J. Am. Chem. Soc.* 133, 2192 (2011/02/23, 2011).]

124. Chen, Y.; Cruz-Chu, E. R.; Woodard, J. C.; Gartia, M. R.; Schulten, K.; Liu, L. *Acs Nano* **2012,** 6, (10), 8847-56.

125. make_gold_surface.svl, Scientific Vector Language (SVL) source code provided by Chris Williams at Chemical Computing Group Inc., 1010 Sherbooke St. West, Suite #910, Montreal, QC, Canada, H3A 2R7, 2011

126. Molecular Operating Environment (MOE), 2011.10; Chemical Computing Group Inc., 1010 Sherbooke St. West, Suite #910, Montreal, QC, Canada, H3A 2R7, 2011.

127. Cieplak, P.; Caldwell, J.; Kollman, P. *J. Comp. Chem.* **2001,** 22, (10), 1048-1057.

128. Phillips, J. C.; Braun, R.; Wang, W.; Gumbart, J.; Tajkhorshid, E.; Villa, E.; Chipot, C.; Skeel, R. D.; Kalé, L.; Schulten, K. *J. Comp. Chem.* **2005,** 26, (16), 1781-1802.

129. Humphrey, W.; Dalke, A.; Schulten, K. *J. Mol. Modeling* **1996,** 14, 33-38.

130. Gibaud, T.; Barry, E.; Zakhary, M. J.; Henglin, M.; Ward, A.; Yang, Y.; Berciu, C.; Oldenbourg, R.; Hagan, M. F.; Nicastro, D.; Meyer, R. B.; Dogic, Z. *Nature* **2012,** 481, (7381), 348-351.

131. Liu, Y.; Zhang, Y.; Chow, M.-J.; Chen, Q. N.; Li, J. *Phys. Rev. Lett.* **2012,** 108, (7), 078103.

132. Amaya, T.; Sakane, H.; Nakata, T.; Hirao, T. *Pure Appl. Chem.* **2010,** 82, (4), 969-978.

133. Ginzburg, V. L. *Zh. Eksp. Teor. Fiz* **1945**, (15), 739.

134. Cillessen, J. F. M.; Prins, M. W. J.; Wolf, R. M. *J. Appl. Phys.* **1997,** 81, (6), 2777-2783.

135. For simplicity, the van der Waals volume here is estimated based on the molecular geometry and the van der Waals radius of each atom involved.

136. Kydd, R. A.; Rauk, A. *J. Mol. Struct.* **1981,** 77, (3-4), 227-238.

137. Jow, T. R.; Cygan, P. J. *J. Appl. Phys.* **1993,** 73, (10), 5147-5151.

138. Janovec, V. *Czech. J. Phys.* **1958,** 8, (1), 3-15.

139. Kay, H. F.; Dunn, J. W. *Philos. Mag.* **1962,** 7, (84), 2027-2034.

140. Pertsev, N. A.; Contreras, J. R.; Kukhar, V. G.; Hermanns, B.; Kohlstedt, H.; Waser, R. *Appl. Phys. Lett.* **2003,** 83, (16), 3356-3358.

141. Yao, Y. P.; Liu, Y. K.; Dong, S. N.; Yin, Y. W.; Yang, S. W.; Li, X. G. *Appl. Phys. Lett.* **2012,** 100, (19), 193504.

142. Kim, M.-H.; Lee, G. J.; Keum, C.-M.; Lee, S.-D. *Org. Electron.* **2013,** 14, (5), 1231-1236.

143. Scott, L. T.; Hashemi, M. M.; Bratcher, M. S. *J. Am. Chem. Soc.* **1992,** 114, (5), 1920-1921.

144. Miyajima, D.; Araoka, F.; Takezoe, H.; Kim, J.; Kato, K.; Takata, M.; Aida, T. *Science* **2012,** 336, (6078), 209-213.

145. Shen, Y.; Chen, C.-F. *Chem. Rev.* **2011,** 112, (3), 1463-1535.

146. Dreher, S. D.; Katz, T. J.; Lam, K. C.; Rheingold, A. L. *J. Org. Chem.* **2000,** 65, (3), 815-822.

147. Reetz, M. T.; Beuttenmller, E. W.; Goddard, R. *Tetrahedron Lett.* **1997,** 38, (18), 3211-3214.

148. Nishida, J.-i.; Suzuki, T.; Ohkita, M.; Tsuji, T. *Angew. Chem. Int. Edit.* **2001,** 40, (17), 3251-3254.

149. Tanaka, K.; Osuga, H.; Kitahara, Y. *J. Chem. Soc., Perkin Trans. 2* **2000**, (12), 2492-2497.

150. Kelly, T. R.; Tellitu, I.; Sestelo, J. P. *Angew. Chem. Int. Ed.* **1997,** 36, (17), 1866-1868.

151. Yamamoto, K.; Ikeda, T.; Kitsuki, T.; Okamoto, Y.; Chikamatsu, H.; Nakazaki, M. *J. Chem. Soc., Perkin Trans. 1* **1990**, (2), 271-276.

152. Nakazaki, M.; Yamamoto, K.; Ikeda, T.; Kitsuki, T.; Okamoto, Y. *J. Chem. Soc., Chem. Commun.* **1983**, (14), 787-788.

153. Lovinger, A. J.; Nuckolls, C.; Katz, T. J. *J. Am. Chem. Soc.* **1998,** 120, (2), 264-268.

154. Newman, M. S.; Lednicer, D. J. *J. Am. Chem. Soc.* **1956,** 78, 4765.

155. Aloui, F.; El Abed, R.; Marinetti, A.; Ben Hassine, B. *Tetrahedron Lett.* **2007,** 48, (11), 2017-2020.

156. Martin, R. H. *Angew. Chem. Int. Ed.* **1974,** 13, (10), 649-660.

157. Liu, L.; Yang, B.; Katz, T. J.; Poindexter, M. K. *J. Org. Chem.* **1991,** 56, (12), 3769-3775.

158. Dubois, F.; Gingras, M. *Tetrahedron Lett.* **1998,** 39, (28), 5039-5040.

159. Teplý, F.; Stará, I. G.; Starý, I.; Kollárovič, A.; Šaman, D.; Rulíšek, L.; Fiedler, P. *J. Am. Chem. Soc.* **2002,** 124, (31), 9175-9180.

160. Harrowven, D. C.; Nunn, M. I. T.; Fenwick, D. R. *Tetrahedron Lett.* **2002,** 43, (41), 7345-7347.

161. Urbano, A. *Angew. Chem. Int. Ed.* **2003,** 42, (34), 3986-3989.

162. Carreño, M. C.; García-Cerrada, S.; Urbano, A. *Chem. Eur. J.* **2003,** 9, (17), 4118-4131.

163. Caeiro, J.; Peña, D.; Cobas, A.; Pérez, D.; Guitián, E. *Adv. Synth. Catal.* **2006,** 348, (16-17), 2466-2474.

164. The XRD experiment and analysis were performed as a courtesy by Tao Li, a graduate student in Dr. Nathaniel Rosi's group in University of Pittsburgh and a best friend of mine.

165. Cambridge Crystallographic Data Centre (CCDC): http://www.ccdc.cam.ac.uk/pages/Home.aspx

166. March, J., *Advanced Organic Chemistry : Reactions, Mechanisms, and Structure*. 4th ed.; Wiley: New York, 1992; p xv, 1495 p.

167. Emmons, W. D. *J. Am. Chem. Soc.* **1954,** 76, (13), 3470-3472.

168. Lowell, J.; Roseinnes, A. C. *Adv. Phys.* **1980,** 29, (6), 947-1023.

169. Wang, S. H.; Lin, L.; Wang, Z. L. *Nano Lett.* **2012,** 12, (12), 6339-6346.

170. Zhu, G.; Lin, Z.-H.; Jing, Q.; Bai, P.; Pan, C.; Yang, Y.; Zhou, Y.; Wang, Z. L. *Nano Lett.* **2013,** 13, (2), 847-853.